Technische Universität München
Fakultät für Mathematik

Amplitude and sign decompositions by complex wavelets – Theory and applications to image analysis

Martin Storath

Vollständiger Abdruck der von der Fakultät für Mathematik der Technischen Universität München zur Erlangung des akademischen Grades eines

Doktors der Naturwissenschaften (Dr. rer. nat.)

genehmigten Dissertation.

Vorsitzender:		Univ.-Prof. Dr. Michael Ulbrich
Prüfer der Dissertation:	1.	Univ.-Prof. Dr. Brigitte Forster-Heinlein Universität Passau
	2.	Univ.-Prof. Dr. Rupert Lasser
	3.	Univ.-Prof. Dr. Gabriele Steidl Technische Universität Kaiserslautern (schriftliche Beurteilung)

Die Dissertation wurde am 22.11.2012 bei der Technischen Universität München eingereicht und durch die Fakultät für Mathematik am 25.03.2013 angenommen.

Abstract

The present thesis deals with multiscale amplitude and sign decompositions of functions by complex wavelets and their applications to signal and image processing.

We introduce conditions for reasonable complexifications of real-valued wavelet transforms and reconsider various classical complex wavelet constructions with respect to this aspect. We derive a new class of directional wavelets, called monogenic curvelets, by replacing the complexification of the classical curvelet transform by the monogenic signal, which is better compatible with the rotation operations of the curvelet transform. In contrast to the classical curvelets, monogenic curvelets allow for a reasonable decomposition into amplitude and sign over the entire range of scales. Furthermore, we show that monogenic curvelets maintain important properties, such as Calderón reproducing formula and Parseval formula, and that they converge to the classical curvelets at the fine scales.

We develop two image analysis applications of the wavelet amplitudes and the wavelet signs. In the first application, we exploit the duality of curvelet amplitudes and the wavefront set for a new algorithm to separate crossing edges in x-ray images. We develop a suitable edge model based on manifolds with corners which allows for a detailed analysis of the method. In the latter application, a directional statistics approach to the wavelet signs is used for a novel signal and image analysis tool, called the discrete signature. We show in various experiments the edge detection capabilities of the discrete signature.

Eventually, we transfer the findings on amplitude and sign decompositions to a complex wavelet model of mammalian vision, which we extend by a quantization of the wavelet amplitudes. We show in a series of experiments that this extended model accounts for brightness illusions such as the Hermann grid.

Acknowledgement

At this place my gratitude goes to all who contributed to the completion of this work.

Foremost, I would like to express my sincere gratitude to my advisor Prof. Brigitte Forster-Heinlein for the excellent support, the constructive advice, and the constant encouragement. I honestly thank Prof. Rupert Lasser for the opportunity to complete the thesis while working in his research group. I further would like to thank him and Prof. Gabriele Steidl for the interest in this work and for kindly having agreed to write a report. I thank Peter Heinlein for the mentorship and for the constructive discussions about medical imaging.

I especially thank Jürgen Frikel for the invaluable discussions, for the careful proofreading, and for the steady companionship over the last years. My thank goes also to Laurent Demaret, Peter Massopust, and Andreas Weinmann for fruitful discussions and for carefully proofreading. I further would like to thank Leo Arnold for proofreading parts of the thesis.

I gratefully acknowledge the financial support which I received from the project "Multimodal Proteome Imaging" (SysTec, grant 0315508) funded by the German Federal Ministry for Education and Research, from the TUM Graduate School, and from the research cooperation "Conformal monogenic frames for image analysis" funded by the program Acções Integradas Luso-Alemãs/DAAD.

Last but not least, I thank my family and Pia for the constant support and for the patience.

Contents

Chapter 1

Introduction

The wavelet transform has become an essential tool for signal and image processing. Its multiscale structure allows for macroscopic and microscopic views on signals, which enables us to independently process coarse structures and fine details of a signal. Over the last decades, a large variety of wavelets have been developed, and the performance of the different wavelets mainly depends on the desired application. For example, real-valued orthonormal wavelets such as the Daubechies wavelets turned out to be suitable for signal compression. For signal analysis, the analyzing functions are classically complex wavelets. A complex wavelet κ is the combination of a real-valued wavelet ψ and its Hilbert transform $\mathcal{H}\psi$ as imaginary part, that is,

$$\kappa = \psi + i\,\mathcal{H}\psi.$$

Complex-valued analyzing functions of this type have been introduced in the context of time-frequency analysis already by Gabor who applied them to the analysis of hearing [Gab46]. The importance of complex wavelets for signal analysis has been observed by Grossmann and Morlet in their pioneering paper in wavelet theory [GM84]. The great advantage of complex wavelets over real-valued wavelets is that they yield a natural decomposition of the wavelet coefficient functions into a slowly varying envelope, the amplitude, and an oscillatory part, the sign (or phase[1]). The strengths of complex wavelets have been exploited in various applications such as denoising, deconvolution [Kin01], and the detection of singularities [THH05].

In recent years, there has been an increasing interest in generalizations of complex wavelets to higher dimensions, mainly for image processing. Whereas in one dimension the construction of complex wavelets by the Hilbert transform is in some sense unique, there are several reasonable ways to construct multivariate complex wavelets. In fact, there is a variety of different approaches for example the dual tree complex wavelet transform [Kin99], complex curvelets [CD05a], complex shearlets [LLKW05], and monogenic wavelets [OM09, USvdV09, HSMF10, Hel12], which all have proven their usability in image processing.

Although many of those multivariate complex wavelet transforms have found applications in image processing, the roles of the amplitude and the sign of the wavelet coefficients have not been studied systematically. Especially the signs of the wavelet coefficients are poorly understood despite their importance for images. Furthermore, it has not been investigated under which conditions a complex wavelet transform yields a reasonable decomposition into amplitude and sign. The main goals of this work are to study the construction of multivariate complex wavelets for amplitude and sign decompositions and to investigate the use of wavelet amplitude and sign decompositions for image analysis.

[1] In this work, we denote the argument of a complex number z as phase and its representation as complex unit vector as sign, i.e., $\operatorname{sgn} z = \frac{z}{|z|}$.

Construction of complex wavelets for amplitude and sign decompositions

In contrast to the one-dimensional setting, there is no unique way of constructing multivariate complex wavelets. On the one hand, there are several different generalizations of the Hilbert transform, and on the other hand, there is a high degree of freedom in the construction of real-valued wavelets. Our first goal is to investigate which combinations of real-valued wavelet transforms and (generalized) Hilbert transforms yield reasonable complex wavelets with respect to multiscale amplitude and sign decompositions.

Higher dimensional generalizations of the Hilbert transform Whereas in one dimension the Hilbert transform is the only bounded, translation and dilation invariant, and selfinvertible operator on L^2, this is not the case in higher dimensions [Ste70]. Indeed, there are various multi-dimensional generalizations of the Hilbert transform for instance the partial Hilbert transform, the total Hilbert transform and the Riesz transform [Ste70, BS01, Kin09a]. Recently, the Riesz transform has gained a lot of interest in image analysis whose induced complex signal is called monogenic signal [FS01, LBO01, USvdV09, HSMF10, Hel12].

In this work (Chapter 2), we consider a generalized Hilbert transform as an operator generalizing the most important operator properties of the Hilbert transform, namely boundedness, translation and dilation invariance, and self-invertibility. Since the self-invertibility induces a quadrature relationship we call this class quadrature operators. This point of view allows us to treat the frequently occurring generalizations, the partial Hilbert transform and the Riesz transform, in a common framework.

Multiscale amplitude and sign decompositions by complex wavelets In one dimension, a complex wavelet is constructed canonically from a real-valued wavelet by adding its Hilbert transform as imaginary part. In higher dimensions, there is a much higher degree of freedom for the construction of complex wavelets, and in fact there is a large variety of different approaches. For instance, the dual-tree complex wavelet transform is a separable construction of one dimensional complex wavelets [Kin99, SBK05]. Monogenic wavelets, which are based on the Riesz transform, have been proposed in [OM09, USvdV09, HSMF10, Hel12]. Complex curvelets [CD05a, CD05b] and complex shearlets [LLKW05] are by construction implicitly complex wavelets based on the partial Hilbert transform.

In this work (Chapter 3), we construct multivariate complex wavelets from a real-valued wavelet and a quadrature operator. We introduce two requirements for reasonable combinations. First the quadrature operator should preserve the integrability of the real-valued wavelet, and second the quadrature operator should yield an amplitude which is invariant to the group operations of the generating wavelet family. We show that many classical complex wavelet constructions, such as isotropic and anisotropic monogenic wavelets or complex shearlets, are compatible in this sense. However, we observe that the classical complex curvelets, which can be written as combination of real-valued curvelets and the partial Hilbert transform, do not fulfill our second condition. To overcome this, we introduce monogenic curvelets where the complexification is obtained by the Riesz transform instead of the partial Hilbert transform. Since the Riesz transform covaries with rotations the monogenic curvelet amplitude is invariant to the rotation group operation of the curvelet transform. The monogenic curvelet transform preserves important properties of the classical curvelet transform such as Calderón resolution of identity, cf. Theorem 3.7. We show

that the monogenic curvelets converge at the fine scales to the classical curvelets, cf. Theorem 3.10. Thus they behave at the fine scales essentially like the classical curvelets. A further advantage of the monogenic curvelet transform is that we may continue it to the coarse scales by isotropic monogenic wavelets, which leads to a consistent amplitude and sign decomposition over all scales.

The results about the monogenic curvelet transform have been published in

- M. Storath. The monogenic curvelet transform. In *Proceedings of the IEEE International Conference on Image Processing (ICIP), Hong Kong*, pages 353–356, 2010,
- M. Storath. Directional multiscale amplitude and phase decomposition by the monogenic curvelet transform. *SIAM Journal on Imaging Sciences*, 4:57–78, 2011.

The use of wavelet amplitude and sign decompositions for image analysis

Having constructed complex wavelets, we in the further course investigate the roles of the amplitudes and the signs of the wavelet coefficients. Complex wavelet coefficients already have proven their usability in a large variety of signal and image processing applications; for example, edge detection [Kov99], image fusion [FvdVB+04], denoising, image rotation [SBK05], demodulation [USvdV09], equalization of brightness, and descreening [HSMF10]. In this work, we focus on the usability of the amplitudes and the signs of complex wavelet coefficients for image analysis, and we eventually draw a connection between amplitude and sign decompositions in mammalian vision and the perception of optical illusion.

The role of the wavelet amplitudes The amplitudes of the wavelet coefficients are closely connected to the local regularity of a signal in terms of order of differentiability, see e.g. [Mal09] and the references therein. It has been recently shown that the amplitudes of "microlocalizing" wavelet transforms, such as the complex curvelet [CD05a] and the complex shearlet transform [KL09], characterize the wavefront set, which is the classical approach to directional smoothness [Hö03, Hö85]. Due to this connection to the well-established theory of the wavefront set, we can consider the theory behind the amplitudes of the wavelet coefficients as quite well understood. First applications which exploit this connection are edge detection [YLEK09] and geometric separation curvilinear from point-like singularities [KL12].

In this work (Chapter 4), we use the correspondence of the curvelet amplitudes and the wavefront set for developing and analyzing a new method for the separation of overlaying edges in x-ray images. The main idea is to lift the problem of separation of crossing edges to the phase space of locations and orientations $\mathbb{R}^2 \times \mathbb{P}$, where the wavefront set lives in.[2] The key observation is that the wavefront sets of two crossing edges are disconnected whereas each single edge is connected. Therefore, the separation of edges can be achieved by connected component analysis of the wavefront set of the image. For the theoretical analysis of our method, we develop a model for edges in x-ray images based on manifolds with corners. To set up a corresponding analytic edge model, we show that the (geometric) normal space of a manifold with corners equals the wavefront set of a distribution acting on test functions as integration over that manifold, cf. Theorem 4.39. Based on this equality we consider a distribution to define an edge if its wavefront

[2] The symbol $\mathbb{P}$ denotes the real projective space.

set coincides with the (geometric) normal space of some manifold with corners. Using this edge model, we can show the functionality of our separation of edges algorithm, cf. Theorem 4.39. We obtain the numerical estimate of the wavefront set via regression on the amplitudes of the curvelet coefficients and show in numerical experiments that the proposed algorithm applies to practice.

Some preliminary results on the separation of edges in x-ray images have been announced in

- M. Storath. Separation of edges in x-ray images by microlocal analysis. *Proceedings in Applied Mathematics and Mechanics (PAMM)*, 11(1):867–868, 2011.

The role of the wavelet signs Classical results of Fourier and wavelet analysis suggest that the signs of the wavelet coefficients carry a great portion of the information about a signals structure [LJ77]. In fact, images can often be reconstructed from the sign of their Fourier or wavelet coefficients, but not from their amplitude [OL81]. Despite their high information content, the signs of the wavelet coefficients have received much less attention for signal and image analysis, because their rigorous mathematical analysis is often difficult. In contrast to the wavelet amplitudes, no theoretical framework has been established for the wavelet signs. First indications for the usability of wavelet signs in signal analysis have been given by Kronland-Martinet, Morlet, and Grossmann [KMMG87]. They observed that the lines of constant sign in the wavelet domain converge towards the singularities. In [MO87], phase congruency was proposed as a heuristic approach to signal analysis by Fourier signs. Kovesi [Kov99] extended phase congruency by complex wavelets. He applied this modification successfully to edge detection, but the algorithms involve many heuristics and empirical parameters.

In this work (Chapter 5), we propose a novel approach for signal and image analysis based on complex wavelet signs, called discrete signature. The discrete signature uses directional statistics to measure how much the wavelet signs are aligned over the scales. We illustrate in various experiments that the discrete signature is capable of detecting salient points of a signal, such as steps and cusps and that the results are sharply localized. We further generalize the concept to higher dimensions using monogenic wavelets, and derive a new sign-based method for edge detection for two- and three-dimensional images. In contrast to phase congruency, our method does not require any further heuristics or extra parameters while it shows a comparable edge detection performance.

Amplitude and sign decompositions in mammalian vision There is an interesting connection between mammalian vision and complex wavelet transforms. It is a classical result of vision science that the mammalian visual cortex expands an observed scene into a family of oriented wavelets [HW59, DVAT82, Pal99]. It has been shown by Daugman and Lee that this process can be modeled by a family of complex Gabor wavelets [Dau85, Lee96]. It is remarkable that the amplitudes and the signs of the complex wavelet coefficients are represented in separate ways in the visual cortex [Lee96, Pal99], thus we are given a natural amplitude and sign decomposition.

In this work (Chapter 6), we set this amplitude and sign representation in connection with the perception of optical illusions. To this end, we model a quantization of the amplitudes of the wavelet coefficients which is naturally induced by the unary representation in terms of neuronal discharges. We shall see that this quantization of the wavelet amplitudes leads to small errors for natural images, but introduces visible distortions if applied to brightness illusions. We show in a

series of experiments that our model accurately simulates the illusory effects of many brightness illusions, such as the Hermann grid, the Mach bands, and White's illusion.

1.1 Organization of the thesis

The thesis consists of two major parts. In the first part (Chapters 2 and 3), we deal with the construction of multivariate complex wavelets and the resulting amplitude and sign decompositions. In the second part (Chapters 4, 5, and 6), new applications of both the wavelet amplitude and the wavelet sign for image analysis are presented and analyzed.

In Chapter 2 we recall important facts about one and multidimensional complex signals and introduce the generalizing class of quadrature operators. Chapter 3 is devoted to the investigation of complex wavelet transforms and, in particular, to the introduction and analysis of the monogenic curvelet transform. In Chapter 4, we recall the role of the wavelet amplitudes for the microlocal analysis of images, and, based on that, derive and analyze a new algorithm for the separation of edges in x-ray images. In Chapter 5, we illustrate the importance of wavelet signs in images, and we develop a new method for signal and image analysis, which exploits the sign information. In Chapter 6, we draw a connection of the amplitude and sign decompositions to mammalian vision and the perception of brightness illusions. Each of these chapters is closed by further references to related works. At the end of the thesis (Chapter 7), we draw a short conclusion and give an outlook to further directions of research.

1.2 Basic notation

We introduce some basic notations and definitions. The *modulus* or *amplitude* of a complex number $z \in \mathbb{C}$ is defined by

$$|z| = \sqrt{(\operatorname{Re} z)^2 + (\operatorname{Im} z)^2}$$

and its *sign* by

$$\operatorname{sgn} z = \begin{cases} \frac{z}{|z|}, & \text{for } z \neq 0, \\ 0, & \text{for } z = 0. \end{cases} \tag{1.1}$$

For $z \neq 0$, the complex sign can be represented by the *phase angle* $\arg z \in (-\pi, \pi]$, defined by

$$\arg z = \begin{cases} +\arccos \frac{\operatorname{Re} z}{|z|}, & \text{for } \operatorname{Im} z \geq 0, \\ -\arccos \frac{\operatorname{Re} z}{|z|}, & \text{for } \operatorname{Im} z < 0. \end{cases}$$

We will use the phase representation of the sign only for the purpose of visualization.

Further, Ω denotes an open subset in $\mathbb{R}^n$. We write $x \cdot y$ or $\langle x, y \rangle$ for the *inner product* of vectors $x, y \in \mathbb{R}^n$. We write $\langle f, \phi \rangle$ or $\langle \phi, f \rangle$ for the evaluation of a distribution $f \in \mathcal{D}'(\Omega)$ versus a testfunction $\phi \in \mathcal{D}(\Omega)$. We define a bilinear form on $L^2(\mathbb{R}^n, \mathbb{C})$ by

$$\langle f, g \rangle = \int_{\mathbb{R}^n} f(x) g(x) \, \mathrm{d}x.$$

We denote the *modulation* by $e_\xi(x) = e^{2\pi i \xi \cdot x}$ and define the *Fourier transform* for $f \in L^1(\mathbb{R}^n)$ by

$$\hat{f}(\xi) = \mathcal{F}f(\xi) = \int_{\mathbb{R}^n} f(x) e^{-2\pi i \xi \cdot x} \, \mathrm{d}x.$$

We write $\mathcal{F}^{-1}f$ or $f^\vee$ for the inverse Fourier transform of f. For a distribution with compact support $f \in \mathcal{E}'(\mathbb{R}^n)$ the Fourier transform $\hat{f}$ is a function and we may write

$$\hat{f}(\xi) = \langle f, e_{-\xi} \rangle.$$

The Fourier transform for general tempered distributions $f \in \mathcal{S}'(\mathbb{R}^n)$ is defined by duality

$$\langle \hat{f}, \phi \rangle = \langle f, \hat{\phi} \rangle, \text{ for } \phi \in \mathcal{S}(\mathbb{R}^n).$$

The convolution of two integrable function f and g is given by

$$f * g(x) = \int f(x-y) g(y) \, \mathrm{d}y.$$

For $y \in \mathbb{R}$ we define the *unit step function* u_y by

$$u_y(x) = \begin{cases} 1, & \text{for } x > y, \\ 0 & \text{else.} \end{cases}$$

If $y = 0$ we shortly write $u = u_0$.

If $f \in \mathcal{D}'(\Omega)$, then the *singular support* of f, denoted by $\operatorname{sing\,supp} f$, is the set of points in Ω having no open neighborhood to which the restriction of f is a C^∞ function.

We denote the *translation* by $b \in \mathbb{R}^n$ by $\tau_b x = x + b$ and the *(positive) homogeneous dilation* by $a \in \mathbb{R}^+$ by $\delta_a x = ax$. The corresponding translation operator is defined by

$$\tau_b f(x) \coloneqq f(x - b).$$

and the positive homogeneous dilation operator by

$$\delta_a f(x) \coloneqq a^{-n/2} f\left(\frac{x}{a}\right).$$

We say that a function f on $\mathbb{R}^n$ is *homogeneous of degree* $t \in \mathbb{R}$ if

$$f(\lambda x) = \lambda^t f(x)$$

for every $x \in \mathbb{R}^n \setminus \{0\}$ and every $\lambda > 0$.

Chapter 2

Amplitude and sign decompositions of multivariate signals

Our goal is to decompose a multivariate function or a signal into a positive part, the *amplitude*, and a normed (hyper-)complex-valued part, the *sign.* The amplitude shall represent the signal's local intensity whereas the sign shall encodes the oscillatory part of f. In one dimension, the classical way to achieve such a decomposition into amplitude and sign is the *complex signal*[1]*,* introduced by Gabor in his seminal article *Theory of Communication* [Gab46]. The complex signal is the complex-valued function which arises when doubling the positive frequencies of the frequency spectrum and setting the other frequencies to 0. The complex signal induces the natural decomposition of a signal f into amplitude and sign by

$$f(x) = \underbrace{|g(x)|}_{\text{amplitude}} \operatorname{Re}\big(\underbrace{\operatorname{sgn} g(x)}_{\text{sign}}\big),$$

where g denotes the complex signal of f. Classical applications of the complex signal are for example the analysis of hearing [Gab46] or the demodulation of signals [Bed62].

The key observation for a higher dimensional generalization is that the real and the imaginary part of the complex signal form a so called *quadrature pair,* i.e., they are Hilbert transform of each other. Thus, the way to go for higher dimensional complex signals is to generalize the Hilbert transform. In recent years, several reasonable multidimensional generalizations of the complex signal have been proposed, most prominently the complex signal in the sense of the partial Hilbert transform (cf. [BS01] and the references therein) and the monogenic signal, based on the Riesz transform [FS01, LBO01].

This chapter is devoted to the introduction of the Hilbert transform, the one-dimensional complex signal and the induced amplitude and sign decompositions (Section 2.1), as well as to the classical generalizations partial Hilbert transform and Riesz transform (Section 2.3). Apart from the classical results, we provide the following point of view on these generalizations, cf. Section 2.2. At first glance, the classical generalizations extend the Fourier multiplier of the Hilbert transform to higher dimensions. But we can regard the partial Hilbert transform and the Riesz transform also as operators generalizing the characterizing operator properties of the Hilbert transform, namely invariance to translations and dilations, boundedness, and self-invertibility. This observation gives rise to consider the partial Hilbert transform and the Riesz transform as instances of a class of operators having those properties. Here, we call that class *quadrature operators* because the self-invertibility leads to a symmetric quadrature relation. This point of view enables us to treat the different generalizations of the Hilbert transform in a common framework.

[1] The complex signal is also called *analytic signal.*

2.1 Amplitude and sign decomposition by the complex signal

We give a short introduction to the Hilbert transform, the complex signal, and the induced amplitude and sign decomposition. We refer to [Ste70, Hah96, Kin09a, Kin09b] for exhaustive discussions of the topic and the applications to signal processing.

2.1.1 The Hilbert transform

We start with an important fact about continuous linear translation and dilation invariant operators. It is well known that every continuous linear translation invariant operator T on L^2 is the convolution with a proper tempered distribution, cf. [Gra04, Chap. 2.5]. If T additionally commutes with homogeneous dilations, then the corresponding convolution kernel is a homogeneous function. More precisely, the following is true, cf. [Ste70, pp. 28, 39ff].

Proposition 2.1. *Let T be a bounded linear transformation mapping $L^2(\mathbb{R}^n, \mathbb{C})$ to itself, which commutes with translations and homogeneous dilations. Then there exists a bounded measurable function M, homogeneous of degree 0, such that*

$$\widehat{Tf}(\xi) = M(\xi)\hat{f}(\xi), \quad \textit{almost everywhere},$$

for all $f \in L^2(\mathbb{R}^n, \mathbb{C})$. One has then $\|T\| = \|M\|_\infty$. ⌟

Notation 2.2. Let T be as in Proposition 2.1. The Fourier multiplier M associated to T is called the *multiplier* or the *symbol* of T. We denote the multiplier of a linear translation invariant operator T by $\mathrm{M}(T)$. Conversely, we denote the operator associated to the multiplier M by $\mathrm{Op}(M)$. ⌟

One of the most important linear translation and dilation invariant operators is the Hilbert transform, which is defined as follows.

Definition 2.3. The operator $\mathcal{H} : L^2(\mathbb{R}, \mathbb{C}) \to L^2(\mathbb{R}, \mathbb{C})$, defined by

$$\widehat{\mathcal{H}f} := -i \operatorname{sgn} \cdot \hat{f}, \qquad \text{for } f \in L^2(\mathbb{R}, \mathbb{C}), \tag{2.1}$$

is called *Hilbert transform.* ⌟

Remark 2.4. The Hilbert transform can be written as the convolution with the tempered distribution $\frac{1}{\pi}\,\mathrm{P.\,V.}\left(\frac{1}{\bullet}\right)$, where P. V. denotes the Cauchy principal value, thus

$$\mathcal{H}f = \frac{1}{\pi}\,\mathrm{P.\,V.}\left(\frac{1}{\bullet}\right) * f.$$ ⌟

We say that an operator on $L^2(\mathbb{R}^n, \mathbb{C})$ is *real-valued* if it maps real-valued functions into real-valued functions. It follows directly from the fact that the Fourier transform of a real-valued function is Hermitian that the symbol of a real-valued operator is Hermitian. That is, a linear translation invariant operator T is real-valued if and only if

$$\mathrm{M}(T)(\xi) = \overline{\mathrm{M}(T)(-\xi)}, \qquad \text{almost everywhere, } \xi \in \mathbb{R}^n. \tag{2.2}$$

Let us recall the following elementary properties of the Hilbert transform, cf. [Ste70, p. 55].

Lemma 2.5. *The Hilbert transform has the following properties:*

(1) $\mathcal{H}$ is a bounded linear operator on $L^2(\mathbb{R},\mathbb{R})$.

(2) $\mathcal{H}$ commutes with translations.

(3) $\mathcal{H}$ commutes with homogeneous dilations.

(4) $i\mathcal{H}$ is selfinverting, that is, $(i\mathcal{H})^2 = \mathrm{id}$.

(5) $\mathcal{H}$ is anti-selfadjoint, that is, $\mathcal{H}^* = -\mathcal{H}$.

(6) $\mathcal{H}$ anti-commutes with reflections, that is, $\mathcal{H}[f(-\bullet)] = -\mathcal{H}f(\bullet)$, for $f \in L^2(\mathbb{R},\mathbb{R})$. ⌟

Proof. For the proof of (1 – 3), we refer to [Ste70, p. 55].

(4) From $\mathrm{M}(\mathcal{H})^2 = (-i\ \mathrm{sgn}\,)^2 \equiv -1$ we get $\mathcal{H}^2 \equiv -\mathrm{id}$. Hence $(i\mathcal{H})^2 = \mathrm{id}$.

(5) The claim follows from

$$\overline{i\ \mathrm{M}(\mathcal{H})} = \overline{-i^{\,2}\,\mathrm{sgn}} = \mathrm{sgn} = i\ \mathrm{M}(\mathcal{H}).$$

(6) See [Ste70, p. 55]. ∎

It is worth mentioning that the Hilbert transform $\mathcal{H}$ is up to a constant the only operator on $L^2(\mathbb{R},\mathbb{R})$ with the properties (1 – 3) and (6) of Lemma 2.5. For a proof of this fact we refer to [Ste70, p. 55]. Remarkably, the Hilbert transform is – up to sign – also characterized by the properties (1 – 5):

Lemma 2.6. *Let T be an operator on $L^2(\mathbb{R},\mathbb{R})$ with the properties (1 – 5) of Lemma 2.5. Then $T = \pm\mathcal{H}$.* ⌟

Proof. Let T be an operator with the properties (1 – 5) of Lemma 2.5. By virtue of Proposition 2.1, it follows from (1 – 3) that its multiplier $\mathrm{M}(T)$ is homogeneous of degree 0. From the selfinvertibility condition (4) we derive that the multiplier satisfies $(i\ \mathrm{M}(T))^2 \equiv 1$, hence

$$\mathrm{M}(T)(\xi) \in \{-i\,, i\,\}, \qquad \text{almost everywhere.} \tag{2.3}$$

Since T is real-valued, the multiplier is Hermitian, cf. (2.2). Together with (2.3) and the homogeneity of $\mathrm{M}(T)$ we arrive at

$$\mathrm{M}(T)(\xi) = \pm i\ \mathrm{sgn}\ \xi = \mathrm{M}(\pm\mathcal{H})(\xi), \qquad \text{almost everywhere,}$$

which proves the claim. ∎

2.1.2 The complex signal

We say that two square-integrable functions f and g are in *in quadrature* if they are the Hilbert transform of each other, i.e., if

$$g = i\mathcal{H}f. \tag{2.4}$$

The quadrature relation is symmetric, since the selfinvertibility Lemma 2.5(4) yields that

$$g = i\mathcal{H}f \quad \Longrightarrow \quad i\mathcal{H}g = i\mathcal{H}i\mathcal{H}f = f.$$

The complex signal of a square integrable function is the combination the function itself and its quadrature counterpart.

Definition 2.7. Let $f \in L^2(\mathbb{R}, \mathbb{C})$. The function

$$h = f + i\mathcal{H}f \tag{2.5}$$

is called the *complex signal* of f. We call the operator $\mathcal{H}' : L^2(\mathbb{R}, \mathbb{C}) \to L^2(\mathbb{R}, \mathbb{C})$, defined by

$$\mathcal{H}' \coloneqq \mathrm{id} + i\mathcal{H},$$

the *complex signal operator.* ⌟

Remark 2.8. The complex signal is often called *analytic signal* because $\overline{h} = \overline{\mathcal{H}'f}$ is the boundary value of a complex function $H(x + iy)$, i.e.,

$$h(x) = \lim_{y \to 0+} H(x + iy),$$

where H is holomorphic in the upper halfplane $\{z = x + iy : x \in \mathbb{R}, y > 0\}$ and satisfies

$$\int_{-\infty}^{\infty} |H(x + iy)|^2 \, \mathrm{d}x < C, \qquad \text{for } y > 0 \text{ and some constant } C > 0,$$

cf. [Tit48, Theorem 95]. ⌟

The complex signal operator has the following important properties, which derive directly from the properties of the Hilbert transform (Lemma 2.5):

Corollary 2.9. *For the complex signal operator it holds that*

(1) $\mathcal{H}'$ *is a bounded linear operator from* $L^2(\mathbb{R}, \mathbb{C})$ *to* $L^2(\mathbb{R}, \mathbb{C})$.

(2) $\mathcal{H}'$ *commutes with translations.*

(3) $\mathcal{H}'$ *commutes with positive dilations.*

(4) $\mathcal{H}'$ *is quasi-idempotent, i.e.,* $(\mathcal{H}')^2 = 2\mathcal{H}'$.

(5) $\mathcal{H}'$ *is self-adjoint.* ⌟

It further follows directly from the selfinvertibility of the Hilbert transform that the complex signal is invariant under the action of the Hilbert transform $i\mathcal{H}$, that is,

$$i\mathcal{H}\mathcal{H}'f = i\mathcal{H}(f + i\mathcal{H}f) = (i\mathcal{H}f + i\mathcal{H}i\mathcal{H}f) = (i\mathcal{H}f + f) = \mathcal{H}'f.$$

A further important property of the complex signal is that it has a purely one-sided frequency spectrum [Kin09b, Chap. 18.4]; that is, for a square-integrable function f it holds that

$$\widehat{\mathcal{H}'f}(\xi) = \begin{cases} 2\widehat{f}(\xi), & \text{for } \xi > 0, \\ 0, & \text{else,} \end{cases} \qquad \text{almost everywhere.} \tag{2.6}$$

The complex signal induces a natural decomposition of a function $f \in L^2(\mathbb{R}, \mathbb{R})$ into a product of a non-negative amplitude function

$$|\mathcal{H}' f(x)| = \sqrt{f(x)^2 + \mathcal{H} f(x)^2}$$

and a complex-valued sign function

$$\operatorname{sgn}(\mathcal{H}' f(x)) = \frac{\mathcal{H}' f(x)}{|\mathcal{H}' f(x)|}.$$

That is, f can be decomposed into amplitude and sign by

$$f(x) = |\mathcal{H}' f(x)| \operatorname{Re}[\operatorname{sgn}(\mathcal{H}' f(x))]. \tag{2.7}$$

The amplitude function is a slowly varying positive envelope of f, whereas the sign function encodes the oscillatory part of f. This effect is illustrated in the following example.

Example 2.10. Let $a > 0$ and $b \in \mathbb{R}$. The Hilbert transform of the modulated Gaussian

$$f(x) = e^{-ax^2} \cos bx$$

is given by

$$\mathcal{H} f(x) = e^{-ax^2} \operatorname{Im}\left\{ e^{i\,bx} \operatorname{erf}\left[\sqrt{a}\left(\frac{b}{2a} + i\,x \right) \right] \right\},$$

where erf denotes the complex error function, cf. [Kin09b, p. 487]. Figure 2.1(a) depicts the functions for $a = 1$ and $b = 4\pi$. In Figure 2.1(b), we see that the plain real modulus $|f|$ oscillates and that the plain real sign, here depicted as phase angle $\arg f$, is a piecewise constant function. The modulus of the complex signal, on the other hand, is a smoothly varying function without oscillations which corresponds to the Gaussian factor of f. The phase of the complex signal, corresponding to the sign, is a piecewise linear function, encoding the oscillatory cosine factor of f, see Figure 2.1(c). ⌟

2.2 Higher dimensional amplitude and sign decompositions

Having introduced the Hilbert transform and the complex signal in one dimension, we describe in this section generalizations to higher dimensions. In the literature, we find three reasonable approaches for generalizations of the complex signal to n-D. A first possible way is the generalization of the one-sided frequency spectrum property of the complex signal (2.6), that is, to cut off the frequencies in a halfspace or a quadrant; examples for this are the partial and the total Hilbert transform, respectively [BS01]. The most common approach is the generalization based on the Fourier multiplier of the Hilbert transform. This leads to the partial Hilbert transform and, if a tuple of operators is admissible, the Riesz transform [Ste70, FS01]. A third possibility is to generalize the Hilbert transform as operator on L^2. In [Kin08], a generalization is proposed based on the boundedness, and the translation and dilation invariance of the Hilbert transform.

In this work, we follow the latter approach to a generalization of the Hilbert transform. We generalize the characterizing properties (1 – 5) of Lemma 2.5, where the selfinvertibility (4) may

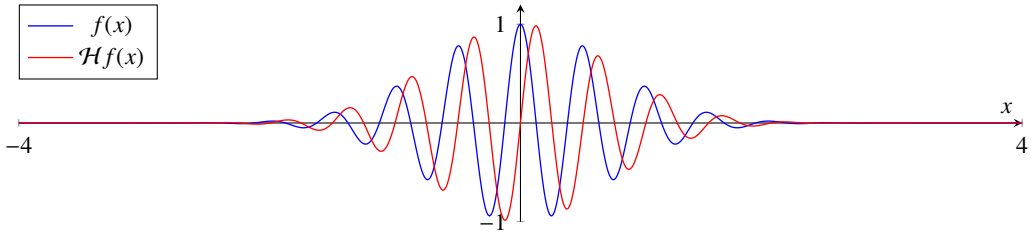

(a) Modulated Gaussian and its Hilbert transform.

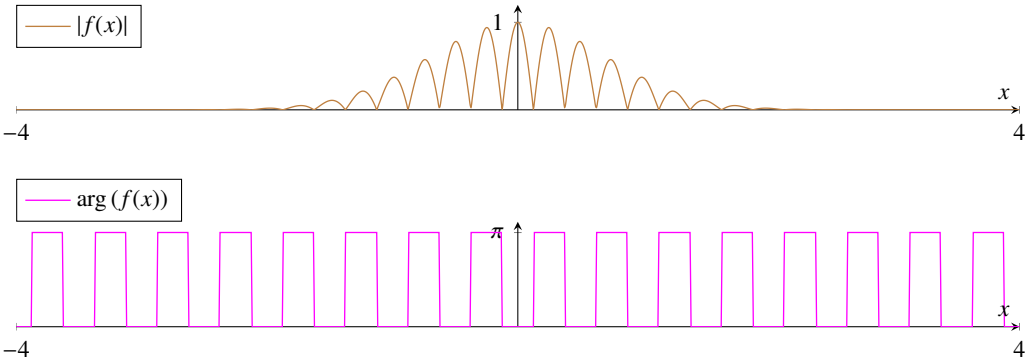

(b) Plain real amplitude and sign (phase) decomposition.

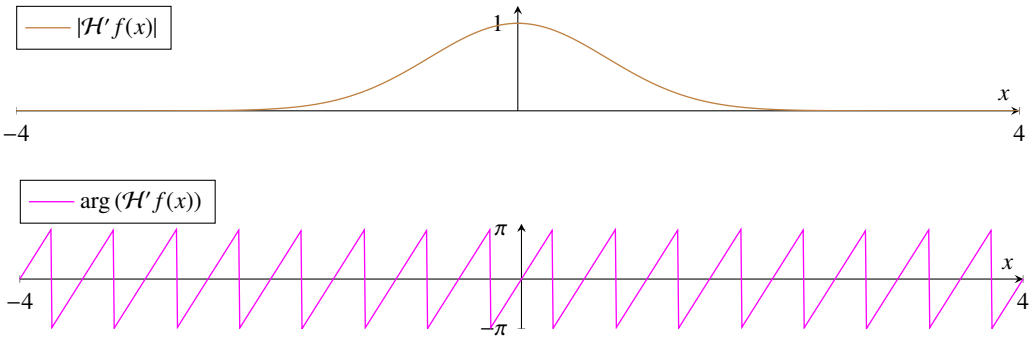

(c) Amplitude and sign (phase) decomposition by the complex signal.

Figure 2.1: Amplitude and sign (or phase) decomposition of the function $f(x) = e^{-x^2}\cos 4\pi x$. (b) The plain real amplitude contains oscillations and the plain real sign (or phase) reduces to a jump function. (c) We nicely see the envelope effect of the analytic signal's instantaneous amplitude $|\mathcal{H}'f|$. Note also that the instantaneous amplitude varies slowly, whereas the sign $\operatorname{sgn}\mathcal{H}'f(x) \in \mathbb{C}$, displayed here as the phase angle $\arg(\operatorname{sgn}\mathcal{H}'f(x)) \in (-\pi, \pi]$, contains the oscillatory part of f.

be fulfilled by a tuple of operators. We denote this type of generalization as *quadrature operator* since the selfinvertibility yields a symmetric quadrature relation as in (2.4). To write up this approach conveniently, we need hypercomplex numbers, so we start with a short introduction into this topic.

2.2.1 Hypercomplex numbers

This introduction to hypercomplex numbers mainly follows [GM91, Chapter 1] and [HSMF10]. In this section, we write $\mathbb{K}$ for $\mathbb{R}$ or $\mathbb{C}$. Let $\{\mathbf{e}_0, \dots, \mathbf{e}_m\}$ be the standard orthonormal basis of $\mathbb{K}^{1+m}$, where $m \in \mathbb{N}$. We equip $\mathbb{K}^{1+m}$ with a vector multiplication such that it holds

$$\begin{aligned} \mathbf{e}_\nu \mathbf{e}_\nu &= -\mathbf{e}_0, && \text{for all } \nu = 1, \dots, m, \\ \mathbf{e}_\nu \mathbf{e}_\mu &= -\mathbf{e}_\mu \mathbf{e}_\nu, && \text{for all } \nu, \mu = 1, \dots, m, \quad \nu \neq \mu. \end{aligned}$$

We also write 1 for the multiplicative identity $\mathbf{e}_0$, so any $v \in \mathbb{K}^{1+m}$ has the representation

$$v = v_0 + \sum_{\mu=1}^{m} \mathbf{e}_\mu v_\mu,$$

where $v_0, ..., v_m \in \mathbb{K}$. In this notation, the complex numbers read

$$\mathbb{C} \cong \{a + \mathbf{e}_1 b : a, b \in \mathbb{R}\}.$$

Note that $\mathbb{K}^{1+m}$ is not closed with respect to multiplication for $m > 1$. In general, for $v, w \in \mathbb{K}^{1+m}$, the product vw is an element of the *Clifford algebra* $\mathbb{K}_m$, which is the closure of $\mathbb{K}^{1+m}$ under the given multiplication. $\mathbb{K}_m$ consist of the 2^m elements $e_0, \dots, e_{2^m-1}$. For example, the multiplicative closure of $\mathbb{R}^{1+1}$ is the complex numbers $\mathbb{C}$, and for $\mathbb{R}^{1+2}$ the quaternions $\mathbb{H}$. However, in this work we only consider powers of 2 of $v \in \mathbb{K}^{1+m}$ which does not lead outside $\mathbb{K}^{1+m}$ because

$$\left(v_0 + \sum_{\mu=1}^{m} \mathbf{e}_\mu v_\mu \right)^2 = v_0^2 - \sum_{\mu=1}^{m} v_\mu^2 + 2v_0 \sum_{\mu=1}^{m} \mathbf{e}_\mu v_\mu \quad \in \mathbb{K}^{1+m}.$$

In analogy to the complex numbers, we call the $\mathbf{e}_0$ component the *real part* of v and the components $\mathbf{e}_1, \dots, \mathbf{e}_m$ the *imaginary parts* of v, so for $v \in \mathbb{K}^{1+m}$ we write

$$\operatorname{Re} v \coloneqq v_0, \qquad \text{and} \qquad \operatorname{Im} v \coloneqq \sum_{\nu=1}^{m} \mathbf{e}_\nu v_\nu.$$

Notice here the slight difference of the hypercomplex imaginary part to the classical complex imaginary part. The classical imaginary part of a complex number is a real number, whereas the imaginary part of a hypercomplex number is a hypercomplex number as well. Further, the hypercomplex conjugation is defined by

$$\overline{v} = v_0 - \sum_{\mu=1}^{m} \mathbf{e}_\mu \overline{v_\mu}. \qquad \text{for } v \in \mathbb{K}^{1+m}.$$

The integral of a hypercomplex-valued function $f : \mathbb{R}^n \to \mathbb{K}^{1+m}$ is defined component-wise, that is, if $f = \sum_{\mu=0}^{m} \mathbf{e}_\mu f_\mu$ with $f_\mu \in L^1(\Omega, \mathbb{K})$, then

$$\int_\Omega f(x)\,\mathrm{d}x = \sum_{\mu=0}^{m} \mathbf{e}_\mu \int_\Omega f_\mu(x)\,\mathrm{d}x$$

If ϕ is a $\mathbb{K}^{1+m}$-valued testfunction, that is, $\phi = \sum_{\mu=0}^{m} \mathbf{e}_\mu \phi_\mu$ where $\phi_\mu \in \mathcal{D}(\Omega, \mathbb{K})$, then we write

$$\langle f, \phi \rangle = \sum_{\mu=0}^{m} \mathbf{e}_\mu \langle f, \phi_\mu \rangle \quad \in \mathbb{K}^{1+m}$$

for the evaluation of a distribution f versus ϕ. Likewise, we define the vector-valued $\mathbb{K}$-bilinear form for $f \in L^2(\mathbb{R}^n, \mathbb{K})$ and $g \in L^2(\mathbb{R}^n, \mathbb{K}^{1+m})$ by

$$\langle f, g \rangle = \sum_{\mu=0}^{m} \mathbf{e}_\mu \langle f, g \rangle \quad \in \mathbb{K}^{1+m}.$$

We write $\hat{f}$ for the component-wise Fourier transform

$$\hat{f} = \sum_{\mu=0}^{m} \mathbf{e}_\mu \hat{f}_\mu.$$

For any vector in $v \in \mathbb{K}^{1+m}$ we define the real non-negative *amplitude* by

$$|v| = \sqrt{|v_0|^2 + \ldots + |v_m|^2}$$

an the *sign* by

$$\operatorname{sgn}(v) \coloneqq \begin{cases} \frac{v}{|v|}, & \text{for } v \neq 0, \\ 0, & \text{else.} \end{cases} \tag{2.8}$$

Further, for $v \in \mathbb{R}^{1+m} \setminus \{0\}$ we call the angle $\Phi(v) \in [0, \pi]$ between the imaginary part and the real part the *phase*

$$\Phi(v) \coloneqq \arccos \frac{\operatorname{Re} v}{|v|}.$$

With these notations, we can decompose a vector $v \in \mathbb{R}^{1+m}$ into amplitude and sign by

$$v = |v| \operatorname{sgn}(v),$$

In particular for $v \neq 0$, we get an amplitude and phase representation of the real part by

$$v_0 = |v| \operatorname{Re}(\operatorname{sgn} v) = |v| \cos \Phi(v).$$

2.2.2 Quadrature operators

Now we are able to introduce quadrature operators as generalization of the Hilbert transform based on the properties (1 – 5) of Lemma 2.5, namely invariance to translations and positively homogeneous dilations, boundedness on $L^2(\mathbb{R}^n)$, real-valence, selfinvertibility and anti-selfadjointness.

Definition 2.11. Let $m \in \mathbb{N}$ and $Q_1, \dots, Q_m$ an m-tuple of linearly independent operators from $L^2(\mathbb{R}^n, \mathbb{R})$ to itself. We call the operator

$$Q = \sum_{\mu=1}^{m} \mathbf{e}_\mu Q_\mu$$

quadrature operator if the following conditions are fulfilled:

(1) Q_μ is a bounded linear operator from $L^2(\mathbb{R}^n, \mathbb{R})$ to $L^2(\mathbb{R}^n, \mathbb{R})$ for every $\mu = 1, \dots, m$.

(2) Q_μ is invariant under translations for every $\mu = 1, \dots, m$.

(3) Q_μ is invariant under positively homogeneous dilations for every $\mu = 1, \dots, m$.

(4) Q is selfinverting, i.e., $Q^2 = \mathrm{id}$.

(5) Q_μ is anti-selfadjoint for every $\mu = 1, \dots, m$, that is, $Q_\mu^* = -Q_\mu$.

We call m the *order* of the quadrature operator. We define the only quadrature operator of order $m = 0$ to be the identity. ⌟

The properties (1 – 3) of Definition 2.11 will allow for reasonable combinations of quadrature operators with wavelet transform. Property (4) yields the quadrature relation

$$g = Qf \quad \Rightarrow \quad Qg = QQf = f.$$

The name quadrature operator comes from this relation. Property (5) assures that the multipliers are all purely imaginary.

We still need to specify a reasonable domain of a quadrature operator Q. The domain of Q ought to contain all real-valued, square-integrable functions, and should be invariant under the action of Q. Therefore, the natural choice is the space

$$X_Q = \left\{ f + Qg : f, g \in L^2(\mathbb{R}^n, \mathbb{R}) \right\} \subset L^2(\mathbb{R}^n, \mathbb{R}^{1+m}). \tag{2.9}$$

From the calculation

$$Qh = Q(f + Qg) = Qf + Q^2 g = g + Qf$$

we see that $QX_Q = X_Q$, so indeed X_Q is invariant under the action of Q.

Example 2.12. Let $n = 1$. From Lemma 2.6 follows that $\pm\mathbf{e}_1\mathcal{H}$ is the only quadrature operator on $X_{\mathcal{H}}(\mathbb{R}) \cong L^2(\mathbb{R}, \mathbb{C})$ of order 1. ⌟

The following two propositions characterize the partial multipliers of a quadrature operator.

Proposition 2.13. *Let $Q : X_Q \to X_Q$ be a quadrature operator of order $m > 0$. Then the mulitpliers $\mathrm{M}(Q_\mu)$ are homogeneous of degree 0, purely imaginary, Hermitian and it holds*

$$-\sum_{\mu=1}^{m} \mathrm{M}(Q_\mu)(\xi)^2 = 1, \qquad \textit{almost everywhere}. \tag{2.10}$$

Proof. It follows from the anti-selfadjointness (Definition 2.11(5)) that $Q_\mu^* = -Q_\mu$, hence

$$\mathrm{M}(Q_\mu) = -\overline{\mathrm{M}(Q_\mu)}, \qquad \text{for all } \mu = 1, \dots, m.$$

Thus the symbols $\mathrm{M}(Q_\mu)$ are purely imaginary. Since all Q_μ are real-valued operators it follows with (2.2) that $\mathrm{M}(Q_\mu)$ is Hermitian for every $\mu = 1, \dots, m$. The last claim (2.10) can be seen as follows. First we notice that the operators Q_ν commute which each other, since they are of convolution type. From $\mathbf{e}_\nu \mathbf{e}_\mu = -\mathbf{e}_\mu \mathbf{e}_\nu$ we get that the mixed terms in Q^2 cancel out. Hence we have

$$\mathrm{id} = Q^2 = \sum_{\nu=1}^{m} \mathbf{e}_\nu Q_\nu \sum_{\mu=1}^{m} \mathbf{e}_\mu Q_\mu = \sum_{\nu=1}^{m} \sum_{\mu=1}^{m} \mathbf{e}_\nu \mathbf{e}_\mu Q_\nu Q_\mu = -\sum_{\mu=1}^{m} Q_\nu^2,$$

thus on the Fourier side

$$-\sum_{\mu=1}^{m} \mathrm{M}(Q_\mu)^2 \equiv 1.$$

■

Proposition 2.14. *Let $m \in \mathbb{N}$ and let $M_\mu \in L^\infty(\mathbb{R}^n, \mathbb{C})$, $\mu = 1, ..., m$, be a tuple of linearly independent multipliers which are homogeneous of degree 0. If M_μ is purely imaginary and Hermitian for every $\mu = 1, ..., m$, and if*

$$-\sum_{\mu=1}^{m} \mathrm{M}(Q_\mu)(\xi)^2 = 1, \qquad \textit{almost everywhere} \tag{2.11}$$

then

$$Q = \sum_{\mu=1}^{m} \mathbf{e}_\mu \operatorname{Op}(M_\mu) \tag{2.12}$$

is a quadrature operator of order m. ⌟

Proof. Let $\mu \in \{1, ..., m\}$. $\operatorname{Op} M_\mu$ is indeed a bounded linear translation invariant operator on $L^2(\mathbb{R}^n, \mathbb{C})$ to itself since $M_\mu \in L^\infty(\mathbb{R}^n, \mathbb{C})$, see [Gra04, Theorem 2.5.10]. Then, $\operatorname{Op}(M_\mu)$ is real-valued since M_μ is Hermitian. As M_μ is purely imaginary $\operatorname{Op}(M_\mu)$ is anti-selfadjoint. The invariance to homogeneous dilations follows from the homogeneity of the multiplier M_μ. From (2.11) we get the selfinvertibility of Q. ■

From Proposition 2.13 and Proposition 2.14 we see that the partial multipliers of a quadrature operator are sign-functions on every line passing through the origin, which sum up quadratically to -1, and in particular,

$$M_\mu(t\xi) = \operatorname{sgn}(t) M_\mu(\xi),$$

for almost every $\xi \in \mathbb{R}^n \setminus \{0\}$ and $t \in \mathbb{R} \setminus \{0\}$.

2.2.3 Complex signals

Having defined generalizations of the Hilbert transform, we now introduce in analogy to the one-dimensional complex signal operator (Definition 2.7) a complex signal operator for multivariate signals.

Definition 2.15. Let $Q : X_Q(\mathbb{R}^n) \to X_Q(\mathbb{R}^n)$ be a quadrature operator of order $m \in \mathbb{N}$. We define the *Q-complex signal operator,* denoted by Q', as

$$Q' = \mathrm{id} + Q. \qquad \lrcorner$$

We also say shortly *complex signal operator.* The complex signal operator Q' commutes with homogeneous dilations and translation because Q does so. Further, like the one-dimensional complex signal, the complex signal operator is quasi-idempotent and invariant under the action of the associated quadrature operator.

Lemma 2.16. *Let $Q : X_Q(\mathbb{R}^n) \to X_Q(\mathbb{R}^n)$ be a quadrature operator. Then*

$$QQ' = Q'Q = Q'$$

and Q' is quasi-idempotent, that is,

$$Q'^2 = 2Q'. \qquad \lrcorner$$

Proof. The claim follows directly using $Q^2 = \mathrm{id}$ by

$$QQ' = Q(\mathrm{id} + Q) = Q + Q^2 = Q + \mathrm{id} = Q'$$

and

$$Q'^2 = \mathrm{id} + 2Q + Q^2 = 2\mathrm{id} + 2Q = 2Q'. \qquad \blacksquare$$

The assertions of Lemma 2.16 can be illustrated by the following commutative diagrams, where $f \in L^2(\mathbb{R}^n, \mathbb{R})$ and Q a quadrature operator of order $m \in \mathbb{N}$.

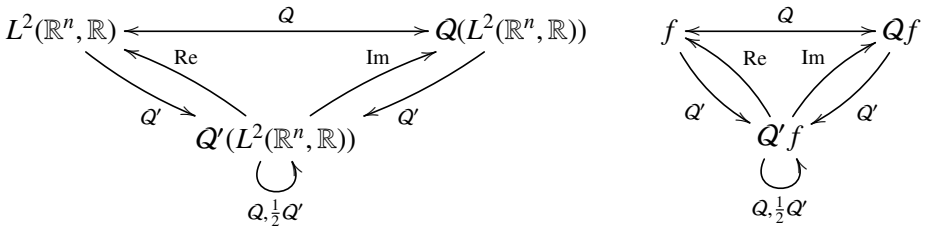

We recall that the goal of this chapter was the generalization of the one-dimensional amplitude and sign decomposition (2.7). We now define such a decomposition in higher dimension as follows.

Definition 2.17. Let Q be a quadrature operator of order $m \in \mathbb{N}$ and let $f \in L^2(\mathbb{R}^n, \mathbb{R})$. We define the *Q-amplitude* of f by

$$|Q'f(x)| = \sqrt{f(x)^2 + Q_1 f(x)^2 + \ldots + Q_m f(x)^2} \tag{2.13}$$

and the *Q-sign* of f by

$$\operatorname{sgn}(Q'f(x)) = \begin{cases} \frac{Q'f(x)}{|Q'f(x)|}, & \text{if } |Q'f(x)| \neq 0, \\ 0, & \text{else.} \end{cases} \tag{2.14}$$

We occasionally omit the quadrature operator Q and shortly say *amplitude* and *sign*. With these definitions, we can decompose a signal f into Q-amplitude and Q-sign by

$$f = |Q'f| \operatorname{Re} \operatorname{sgn}(Q'f)$$

of a real-valued signal $f \in L^2(\mathbb{R}, \mathbb{R})$. In the Chapters 4, 5, and 6, we shall see that both the amplitude and the sign are useful in signal and image analysis.

2.3 Two important quadrature operators

In this section we study the two most frequently used generalizations of the Hilbert transform, namely the partial Hilbert transform and the Riesz transform. We in particular point out that the first commutes with shearings whereas the latter intertwines with rotations. These properties are important for the subsequent chapter, where we investigate the compatibility of quadrature operators with the group operations of wavelets.

2.3.1 The partial Hilbert transform

The partial Hilbert transform acts as a one-dimensional Hilbert transform with respect to some fixed direction ξ_0.

Definition 2.18. Let $\xi_0 \in \mathbb{R}^n \setminus \{0\}$. The *partial Hilbert transform with respect to* ξ_0 is defined for $f \in L^2(\mathbb{R}^n, \mathbb{R})$ by

$$\widehat{\mathcal{H}_{\xi_0} f}(\xi) := -i \operatorname{sgn}(\langle \xi, \xi_0 \rangle) \hat{f}(\xi), \tag{2.15}$$

almost everywhere. ⌟

It follows directly from the characterization in Proposition 2.14 that $\mathbf{e}_1 \mathcal{H}_{\xi_0}$ is a quadrature operator of order $m = 1$. The partial Hilbert transform occurs naturally in the context of functions whose Fourier transform is supported in one halfspace, compare also [Mal09, Ch. 4].

Lemma 2.19. *Let $\xi_0 \in \mathbb{R}^n \setminus \{0\}$ and denote $\Xi := \{\xi \in \mathbb{R}^n : \langle \xi_0, \xi \rangle \geq 0\}$ the halfspace defined by ξ_0. Let $f \in L^2(\mathbb{R}^n, \mathbb{C})$ such that $\operatorname{supp} \hat{f} \subset \Xi$. Then there is a real-valued function $g \in L^2(\mathbb{R}^n, \mathbb{R})$ such that*

$$f = g + i \mathcal{H}_{\xi_0} g. \tag{2.16}$$

Proof. We define g in the Fourier domain by $\hat{g}(\xi) = \frac{1}{2}(\hat{f}(\xi) + \overline{\hat{f}(-\xi)})$, almost everywhere. As $\hat{g}$ is Hermitian, it follows that g is real-valued. To see (2.16) we observe that

$$\hat{f}(\xi) = \begin{cases} 2\hat{g}(\xi), & \text{for } \langle \xi_0, \xi \rangle \geq 0, \\ 0, & \text{else,} \end{cases}$$

and calculate

$$\mathcal{F}(g + i \mathcal{H}_{\xi_0} g)(\xi) = \hat{g}(\xi) + i \operatorname{M}(\mathcal{H}_{\xi_0}) \hat{g}(\xi) = [1 - i^2 \operatorname{sgn}(\langle \xi, \xi_0 \rangle)] \hat{g}(\xi) = \hat{f}(\xi).$$

The claim follows by taking inverse Fourier transforms. ∎

For the partial Hilbert transform, we have an intertwining relationship with linear invertible mappings. For its formulation, we require some notation. Let $A : \mathbb{R}^n \to \mathbb{R}^n$ be a linear invertible mapping. We write $(A_{\nu,\mu})$ for the matrix realization of A. We denote the induced operation on functions f on $\mathbb{R}^n$ with the same symbol A, that is,

$$Af(x) \coloneqq f(A^{-1}x).$$

Lemma 2.20. *Let $\xi_0 \in \mathbb{R}^n \setminus \{0\}$ and let $A : \mathbb{R}^n \to \mathbb{R}^n$ be a linear invertible mapping. Then for any $f \in L^2(\mathbb{R}^n, \mathbb{R})$ it holds that*

$$A(\mathcal{H}_{\xi_0} f) = \mathcal{H}_{A\cdot\xi_0}(Af). \tag{2.17}$$

Proof. By the intertwining relations of A with the Fourier transform, cf. Appendix A.1, we get that

$$\begin{aligned}
\mathcal{F}(A(\mathcal{H}_{\xi_0} f))(\xi) &= \frac{1}{|\det A^{-1}|}\widehat{\mathcal{H}_{\xi_0} f}(A^T\xi) \\
&= -i\ \operatorname{sgn}(\langle \xi_0, A^T\xi\rangle)\,|\det A|\,\hat{f}(A^T\xi) \\
&= -i\ \operatorname{sgn}(\langle A\xi_0, \xi\rangle)\,|\det A|\,\hat{f}(A^T\xi) \\
&= -\,i\ \operatorname{sgn}(\langle A\xi_0, \xi\rangle)\,\widehat{Af}(\xi) \\
&= \mathcal{F}(\mathcal{H}_{A\xi_0} Af)(\xi),
\end{aligned}$$

almost everywhere. The assertion follows by taking the inverse Fourier transform on both sides. ∎

Since for any $\lambda > 0$ the operators $\mathcal{H}_{\xi_0}$ and $\mathcal{H}_{\lambda\xi_0}$ are equal, the following assertion follows from Lemma 2.20.

Corollary 2.21. *Let $\xi_0 \in \mathbb{R}^n \setminus \{0\}$ and $A : \mathbb{R}^n \to \mathbb{R}^n$ a linear invertible mapping such that ξ_0 is an eigenvector to a positive eigenvalue $\lambda > 0$. Then*

$$A(\mathcal{H}_{\xi_0} f) = \mathcal{H}_{\xi_0}(Af). \qquad \lrcorner$$

A particular interesting case of Corollary 2.21 are shearings in the plane. A shear matrix S with respect to the x_1-axis, leaving the x_2- coordinate invariant, is of the form

$$S = \begin{pmatrix} r & s \\ 0 & t \end{pmatrix} \qquad \text{where } s, t \in \mathbb{R} \text{ and } r > 0.$$

The vector $\xi_0 = (0, 1)^T$ is an eigenvector to the eigenvalue r of S, so from Corollary 2.21 follows that the shear operator S commutes with the partial Hilbert transform with respect to ξ_0, that is, $\mathcal{H}_{\xi_0} S = S\mathcal{H}_{\xi_0}$. We will come back to this case in Section 3.1, when we deal with the compatibility of wavelet group operations and quadrature operators.

2.3.2 The Riesz transform

The Riesz transform is a tuple of n partial transforms, thus it is a quadrature operator of order $m = n$.

Definition 2.22. The *partial Riesz transform with respect to the ν-th coordinate axis,* denoted by $\mathcal{R}_\nu$, where $\nu = 1, \ldots, n$, is defined for $f \in L^2(\mathbb{R}^n, \mathbb{R})$ by

$$\widehat{\mathcal{R}_\nu f}(\xi) := -i \frac{\xi_\nu}{|\xi|} \hat{f}, \tag{2.18}$$

almost everywhere. The *Riesz transform* is the vector of all n partial Riesz transforms, that is,

$$\mathcal{R} f := \mathbf{e}_1 \mathcal{R}_1 f + \ldots + \mathbf{e}_n \mathcal{R}_n f. \tag{2.19}$$

The $\mathcal{R}$-complex signal $\mathcal{R}' f$ of a square-integrable real-valued function f is called *monogenic signal,* see [FS01].

It was proven by Stein [Ste70] that the Riesz transform covaries with orthogonal transformations and that this is the only n-tuple of linear, bounded, translation and dilation invariant operators on L^2 with this property. We formulate the analogous statement in terms of quadrature operators.

Lemma 2.23. *Let $f \in L^2(\mathbb{R}^n, \mathbb{R})$ Let Q be a quadrature operator of order n satisfying*

$$U Q_\nu U^{-1} f = \sum_{\mu=1}^{n} U_{\nu,\mu} Q_\mu f, \qquad \text{for all } \nu = 1, \ldots, n, \tag{2.20}$$

and for any linear orthogonal mapping $U : \mathbb{R}^n \to \mathbb{R}^n$. Then

$$Q = \pm \mathcal{R}. \qquad \lrcorner$$

Proof. We first check that $\mathcal{R}$ indeed satisfies (2.20). To this end we calculate in the Fourier domain using (A.2)

$$\begin{aligned} \mathcal{F}(U Q_\nu U^{-1} f)(\xi) &= U(-i \frac{\xi_\nu}{|\xi|}(U^{-1}\hat{f}))(\xi) \\ &= -i \frac{\sum_{\mu=1}^n U_{\nu,\mu}\xi_\mu}{|\xi|} U U^{-1} \hat{f}(\xi) = \sum_{\mu=1}^{n} -i \frac{\xi_\mu}{|\xi|} U_{\nu,\mu} \hat{f}(\xi) = \sum_{\mu=1}^{n} U_{\nu,\mu} \mathcal{F}(Q_\mu f(\xi)) \end{aligned}$$

almost everywhere. The transformation law (2.20) follows by taking inverse Fourier transforms.

To see the opposite direction, we use the following result of [Ste70, p. 58]: If a n-tuple $Q_1, ..., Q_n$ of translation and dilation invariant, bounded operators on $L^2(\mathbb{R}^n, \mathbb{R})$ which satisfies (2.20) for every linear orthogonal mapping U, then $Q_\mu = c\mathcal{R}_\mu$ for every $\mu = 1, ..., n$, and some non-zero constant c. With this results, it only remains to show that $c = \pm 1$. Since $Q = c\mathcal{R}$ is a quadrature operator the squared multipliers sum up to -1 by virtue of Proposition 2.13, so

$$-1 = \sum_{\mu=1}^{n} \mathrm{M}((\mathcal{R}_\nu)(\xi))^2 = \sum_{\mu=1}^{n} c^2 i^2 \frac{\xi_\mu^2}{|\xi|^2} = -c^2 \sum_{\mu=1}^{n} \frac{\xi_\mu^2}{|\xi|^2} = -c^2,$$

for almost every $\xi \in \mathbb{R}^n$. Since $\mathcal{R}_\mu$ is a real-valued transform for every $\mu = 1, ..., n$, we get that $c \in \mathbb{R}$, hence $c_{1/2} = \pm 1$. So we have proved that $Q = \pm \mathcal{R}$. ∎

The covariant transformation law of the Riesz transform (2.20) has the consequence that the $\mathcal{R}$-amplitude is invariant under orthogonal transformations.

Lemma 2.24. *Let $f \in L^2(\mathbb{R}^n, \mathbb{R})$ and let $U : \mathbb{R}^n \to \mathbb{R}^n$ a be a linear orthogonal mapping. Then we have that*

$$|U\mathcal{R}U^{-1} f| = |\mathcal{R}f|.$$

In particular,

$$|U\mathcal{R}' U^{-1} f| = |\mathcal{R}' f|. \qquad \lrcorner$$

Proof. Since U is orthogonal, we may apply Lemma 2.23 to get

$$U\mathcal{R}U^{-1} f = \sum_{\nu=1}^{n} \mathbf{e}_\nu U\mathcal{R}_\nu U^{-1} f = \sum_{\nu=1}^{n} \mathbf{e}_\nu \sum_{\mu=1}^{n} U_{\nu,\mu}\mathcal{R}_\mu f.$$

This can be considered as matrix vector multiplication if $\mathcal{R}f$ is considered as row vector, i.e.,

$$U\mathcal{R}U^{-1} f = \mathcal{R}f \cdot U^T.$$

Since the linear orthogonal mapping U preserves the modulus it follows that

$$|U\mathcal{R}U^{-1} f| = |\mathcal{R}f \cdot U^T| = |\mathcal{R}f|, \tag{2.21}$$

which is the first claim. The second claim is a direct consequence. ∎

Remark 2.25. The Riesz transform formally can be seen as the weak gradient of the Riesz potential of order 1. Let I_s denote the Riesz potential of order s, where $s < n$, defined by

$$\widehat{I_s f}(\xi) := (2\pi|\xi|)^{-s} \hat{f}(\xi),$$

for a sufficiently smooth function f on $\mathbb{R}^n$, see [Ste70, Chapter V.1]. Further, let D be the *Dirac operator*

$$D := \sum_{\nu=1}^{n} \mathbf{e}_\nu D_\nu,$$

where D_ν denotes the derivative with respect to the ν-th component (cf. [GM91, Chapter 2]). Then, since $\widehat{D_\nu f}(\xi) = 2\pi i \xi_\nu \hat{f}(\xi)$, we get by a simple manipulation in the Fourier domain the formal identity

$$D_\nu f = -\mathcal{R}_\nu I_{-1} f,$$

for any $\nu = 1, ..., n$. So we formally may rewrite the Riesz transform as the Dirac operator applied to the smoothed function $I_1 f$, that is,

$$\mathcal{R}f = -D\, I_1 f. \tag{2.22}$$

Furthermore, the transformation law (2.20) coincides with the covariant transformation law of the Dirac operator D, which reads as

$$UD_\nu U^{-1} f = \sum_{\mu=1}^{n} U_{\nu,\mu} D_\mu f,$$

for every $\nu = 1, ..., n$. $\lrcorner$

We conclude from the findings of this section, that the partial Hilbert transform is especially well compatible with shearing due to the commutator relationship. In particular, the $\mathcal{H}_{\xi_0}$-amplitude is invariant under shearings with respect to ξ_0. On the other hand, Lemma 2.24 shows that the Riesz transform is adequate for linear orthogonal transformations, such as rotations, since the $\mathcal{R}$-amplitude is invariant to orthogonal transformations. This observation will become of importance in the next chapter, where the compatibility of these quadrature operators with wavelet transforms is studied.

2.4 Further references

The results about the Riesz transform that we have used here are mainly due to Stein [Ste70]. Note that Stein uses a vectorial notation of the Riesz transform instead of the hypercomplex formulation. We here followed the hypercomplex formulation of [GM91, FS01, HSMF10, Hel12] because it allows for convenient and compact notations.

The Riesz transform has simultaneously been introduced to image processing by Felsberg and Sommer [FS01] in the context of digital signal processing and by Larkin et. al. [LBO01] in the context of optics. The term *monogenic signal* for the complex signal based on the Riesz transform was coined by Felsberg and Sommer [FS01].

The partial Hilbert transform was investigated in [Hah96] and, in the context of image processing, in [BS01]. However, there has been probably earlier works on the topic in other contexts, since the partial Hilbert transform naturally appears at functions whose frequency spectrum lies in one half-plane.

The generalization of the Hilbert transform based on its operator properties is inspired by the work [Kin08]. There, King proposes to generalize the Hilbert transform based on its important operator properties, namely the linearity, the boundedness, and the invariance to translations and dilations. The main difference to our notion of quadrature operator is that we allow an m-tuple of operators instead of a single operator, which enables us to treat the Riesz transform in that framework.

Chapter 3

Directional multiscale amplitude and sign decomposition by the monogenic curvelet transform

In one dimension, complex wavelets[1] are constructed from a real-valued wavelet by adding its Hilbert transform as imaginary part, cf. [SBK05, Mal09]. In two and higher dimensions, the construction of complex wavelets is not that canonical. On the one hand, as we have seen in the last chapter, there are several reasonable generalizations of the Hilbert transform to n-D. On the other hand, we have much more freedom in the choice of the wavelet, since dimensions higher than one allow for anisotropic wavelets as well. As a consequence, there is large variety of different complex wavelet constructions, based on different combinations of generalized Hilbert transforms and wavelets; for example dual-tree complex wavelets [Kin99], complex curvelets [CD05a], complex shearlets [LLKW05] or monogenic wavelets [OM09, USvdV09, HSMF10].

In this work, we consider complex wavelet constructions κ of the type

$$\kappa = \psi + Q\psi = Q'\psi,$$

where ψ is a real-valued primal wavelet and Q a quadrature operator (Section 3.1). However, not every arbitrary combination of quadrature operator and wavelet leads to a reasonable complex wavelet. For example if the quadrature operator introduces step singularities to the spectrum of the wavelet, then the complex wavelet fails to be integrable. Thus our first requirement is that the quadrature operator should preserve the integrability of the wavelet. The second condition, concerns the group operations of the wavelet system. Here, we postulate that the wavelet amplitude shall be invariant under the group actions of the wavelet transform. Since quadrature operators by construction commute with translations and homogeneous dilations, this constraint only affects anisotropic operations like rotations and shearings. Most classical complex wavelets fulfill these constraints, for example complex wavelets based on isotropic wavelets and the Riesz transform [HSMF10, OM09, USvdV09] or the complex shearlet transform [LLKW05, KL07]. However, we shall see that the classical complex curvelet transform [CD05a] does not satisfy the conditions. The atoms of the curvelet transform are complex wavelets in the sense of the partial Hilbert transform, but the amplitude of the curvelets is not invariant respect to their anisotropic group operations, the rotations. The observation that the Riesz transform yields a rotation-invariant amplitude, cf. Lemma 2.23, motivates a modification of the classical curvelet transform based on the Riesz transform, called *monogenic curvelet transform*. We introduce this new quaternion-valued transform in Section 3.2 and we show some remarkable properties. First, the monogenic curvelet

[1] Complex wavelets are sometimes called *analytic wavelets.*

transform can be continued to the coarse scales by an isotropic monogenic wavelet transform. In this way, the monogenic curvelet transform is a complex wavelet over the entire range of scales. Second, the monogenic curvelet transform yields a Calderón resolution of identity and a Parseval formula (Theorem 3.3). In Section 3.3, we establish that the monogenic curvelet transform converges at fine scales to the classical curvelet transform, cf. Theorem 3.10. We provide a proper discretization (Section 3.4) and illustrate in numerical experiments the advantages of the amplitude and sign decomposition by monogenic curvelets for the estimation of directional regularity (Section 3.5).

The major part of this chapter has been published in the *SIAM Journal on Imaging Sciences* [Sto11a].

3.1 Construction of complex wavelets

In this chapter, we describe the construction of complex wavelet from a real-valued wavelet, called primal wavelet, and a quadrature operator. We first introduce compatibility conditions and then look at classical wavelet transform with respect to these conditions.

3.1.1 Compatibility conditions for complex signal operators and wavelets

We now introduce two conditions which allow for a reasonable combination of a wavelet and a quadrature operator. We first recall that a real-valued *wavelet* ψ is a function in $L^1 \cap L^2(\mathbb{R}^n, \mathbb{R})$ which satisfies the admissibility condition

$$\int_{\mathbb{R}^n \setminus \{0\}} \frac{|\hat{\psi}(\xi)|^2}{|\xi|^n} \, \mathrm{d}\xi < \infty. \tag{3.1}$$

The integrability, the square-integrability, and the admissibility of the wavelet are important in order to obtain Calderón resolutions of identity. Our first condition for a complex wavelet consists in the preservation of these wavelet properties.

Definition 3.1. Let $\psi \in L^1 \cap L^2(\mathbb{R}^n, \mathbb{R})$ be a real-valued wavelet and let Q be a quadrature operator of order m. We call the $\mathbb{R}^{1+m}$-valued function $Q'\psi$ a *Q-complex wavelet* if $Q_\mu\psi$ is a wavelet for every $\mu = 1, \dots, m$, that is, if $Q_\mu\psi \in L^1 \cap L^2(\mathbb{R}^n, \mathbb{R})$ and if $Q_\mu\psi$ satisfies the admissibility condition (3.1). ⌟

Since the Fourier multiplier of a quadrature operator is homogeneous of degree 0, the admissibility of the primal wavelet ψ implies the admissibility of the complex wavelet. Furthermore, as quadrature operators are bounded in L^2, the components $Q_\mu\psi$ of the complex wavelet are in L^2 as well.

The only condition which is not trivially satisfies the integrability of $Q_\mu\psi$. A simple necessary condition for the integrability is as follows. Since the Fourier transform of an integrable function is continuous, we get that the Fourier multiplier $\mathrm{M}(Q_\mu) \cdot \hat{\psi}$ is necessarily continuous for $\mu = 1, \dots, m$. Further, we can also give the following simple sufficient condition for the integrability.

Lemma 3.2. *Let $\psi \in \mathcal{S}(\mathbb{R}^n, \mathbb{R})$ be a real-valued wavelet and let Q be a quadrature operator of order $m \in \mathbb{N}$. If*

$$\operatorname{sing\,supp} \mathrm{M}(Q_\mu) \cap \operatorname{supp} \hat{\psi} = \emptyset \quad \textit{for every } \mu = 1, \dots, m,$$

then $Q'\psi$ is a complex wavelet. ⌟

Proof. Let $\mu \in \{1, \dots, m\}$. The condition $\operatorname{sing\,supp} \mathrm{M}(Q_\mu) \cap \operatorname{supp} \hat{\psi} = \emptyset$ implies that $\mathrm{M}(Q_\mu)$ is in C^∞ on a neighborhood of the support of $\hat{\psi}$, so $\mathrm{M}(Q_\mu) \cdot \hat{\psi}$ is smooth. Then, since $\mathrm{M}(Q_\mu)$ is positively homogeneous of degree 0 it follows that $\mathrm{M}(Q_\mu) \cdot \hat{\psi}$ is of rapid decay, thus $\mathrm{M}(Q_\mu) \cdot \hat{\psi}$ is a Schwartz function. In consequence $Q_\mu\psi \in \mathcal{S}(\mathbb{R}^n, \mathbb{R})$, and in particular $Q_\mu\psi \in L^1$. From the homogeneity of $\mathrm{M}(Q_\mu)$ we obtain that $Q_\mu\psi$ satisfies the admissibility condition. Hence $Q'\psi$ is a complex wavelet. ∎

Let us illustrate this compatibility condition by some examples. First, let $\xi_0 \in \mathbb{R}^n \setminus \{0\}$. The multiplier of the partial Hilbert transform $\mathcal{H}_{\xi_0}$ has a step singularity at the subspace $\{\xi_0\}^\perp$. Hence, $\mathcal{H}_{\xi_0}$ is applicable for wavelets whose Fourier spectrum does not intersect $\{\xi_0\}^\perp$; that is, $\operatorname{supp} \hat{\psi} \cap \{\xi_0\}^\perp = \emptyset$. In contrast, if ψ is an isotropic wavelet, then the complex signal $\mathcal{H}'_{\xi_0}\psi$ is not a $\mathcal{H}_{\xi_0}$-complex wavelet, because $\mathcal{H}'_{\xi_0}\psi$ fails to be integrable. In that case the Riesz transform is more suitable. As the multipliers of the partial Riesz transforms $\mathrm{M}(\mathcal{R}_\nu)$, $\nu = 1, \dots, n$, are smooth on $\mathbb{R}^n \setminus \{0\}$, we get by Lemma 3.2 that the Riesz transform $\mathcal{R}$ is applicable for any wavelet whose Fourier spectrum vanishes in a neighborhood of the origin. In particular, the Riesz transform maintains the integrability for both isotropic and anisotropic wavelets.

The first condition for combination of complex signal operators and wavelets assures that filter properties of the mother wavelet are preserved by the quadrature operator. Our second constraint concerns the group operations of the wavelet system. Here, we postulate that the amplitude is invariant to the group operations in the sense that

$$|AQ'A^{-1}\psi| = |Q'\psi|, \tag{3.2}$$

where A denotes a group operation of the wavelet system such as dilation, translation, rotation, and shearing. By construction, a quadrature operator is invariant to translation and homogeneous dilations, thus condition (3.2) only affects anisotropic operations such as rotations and shearings. Constraint (3.2) assures that it does not matter for the wavelet amplitude whether we first complexify the primal wavelet wavelet and then apply the group operations or the other way round.

In the next subsections, we present several important classical complex and hypercomplex wavelet transforms, arising from different combinations of real-valued wavelets and quadrature operators. We first look at isotropic and then at anisotropic constructions.

3.1.2 Complex wavelets based on isotropic primal wavelets

Probably the most simple way of constructing an isotropic wavelet ψ is to take the inverse Fourier transform of a non-negative, radial window function $W : \mathbb{R}_0^+ \to \mathbb{R}_0^+$, satisfying

$$\int_0^\infty W(ar)^2 \frac{\mathrm{d}a}{a} = 1, \qquad \text{for all } r > 0, \tag{3.3}$$

cf. [FJW91]. Then, the formula

$$\hat{\psi}(\xi) = W(|\xi|) \tag{3.4}$$

defines an isotropic wavelet ψ. For these types of wavelets, we have a Calderón decomposition of unity, cf. [FJW91].

Theorem 3.3. *Let $\psi \in L^1(\mathbb{R}^n, \mathbb{R})$ be real-valued and radial, satisfying*

$$\int_0^\infty \hat{\psi}(a\xi)^2 \frac{\mathrm{d}a}{a} = 1, \qquad \text{for all } \xi \in \mathbb{R}^n \setminus \{0\}.$$

Then, for $f \in L^2(\mathbb{R}^n)$,

$$f(x) = \int_0^\infty (\psi_a * \psi_a * f)(x) \frac{\mathrm{d}a}{a}, \tag{3.5}$$

where $\psi_a(x) \coloneqq a^{-n}\psi(\frac{x}{a})$. ⌟

Remark 3.4. Equation 3.5 has to be understood in the following L^2 sense: if $0 < \epsilon < \delta < \infty$ and

$$f_{\epsilon,\delta}(x) = \int_\epsilon^\delta (\psi_a * \psi_a * f)(x) \frac{\mathrm{d}a}{a},$$

then $\left\| f - f_{\epsilon,\delta} \right\|_{L^2(\mathbb{R}^n)} \to 0$ if $\epsilon \to 0$ and $\delta \to 0$, cf. [FJW91]. ⌟

The selfinvertibility of quadrature operators, cf. Definition 2.11(4), allows us to derive a Calderón resolution of identity for isotropic complex wavelets. To this end, we need the following relation for the convolution with complex wavelets.

Lemma 3.5. *Let ψ be a real-valued wavelet on $\mathbb{R}^n$, let Q be a quadrature operator of order $m \in \mathbb{N}$ such that $Q'\psi$ is a Q-complex wavelet. Then*

$$Q'\psi * Q'\psi * f = 2\psi * \psi * Q'f \tag{3.6}$$

for every $f \in L^2(\mathbb{R}^n, \mathbb{R})$ in the L^2-sense. ⌟

Proof. Since ψ and $Q_\mu\psi \in L^1(\mathbb{R}^n, \mathbb{R})$ for any $\mu \in 1, \dots, m$ the convolutions are well defined and the left and right hand side of (3.6) are in $L^2(\mathbb{R}^n, \mathbb{R}^{1+m})$. Since Q_μ is of convolution type for every $\mu = 1, \dots, m$, it follows that

$$Q'\psi * f = \psi * Q'f. \tag{3.7}$$

It remains to show that $Q'\psi * Q'\psi = 2\psi * Q'\psi$. To this end, we first calculate in the Fourier domain

$$\mathcal{F}(-\sum_{\mu=1}^m Q_\mu\psi * Q_\mu\psi) = -\sum_{\mu=1}^m \mathrm{M}(Q_\mu)\cdot\hat{\psi}\cdot\mathrm{M}(Q_\mu)\cdot\hat{\psi} = \hat{\psi}^2 \sum_{\mu=1}^m -\mathrm{M}(Q_\mu)^2 = \hat{\psi}^2,$$

so

$$-\sum_{\mu=1}^m Q_\mu\psi * Q_\mu\psi = \psi * \psi.$$

Then, since the mixed coefficients of $\mathbf{e}_\mu\mathbf{e}_\nu$ cancel out for $\mu, \nu \geq 1$ and $\mu \neq \nu$, we get that

$$\begin{aligned} Q'\psi * Q'\psi &= \sum_{\mu=0}^m \sum_{\nu=0}^m \mathbf{e}_\mu\mathbf{e}_\nu (Q_\mu\psi * Q_\nu\psi) \\ &= \psi * \psi + 2\psi * \sum_{\mu=1}^m \mathbf{e}_\mu Q_\mu\psi - \sum_{\mu=1}^m Q_\mu\psi * Q_\mu\psi \\ &= 2\psi * \psi + 2\psi * \sum_{\mu=1}^m \mathbf{e}_\mu Q_\mu\psi = 2\psi * Q'\psi. \end{aligned}$$

The claim now follows by (3.7). ∎

It follows from Theorem 3.3 and Lemma 3.5 that a complex wavelet arising from the isotropic wavelet in (3.4) has a Calderón decomposition of unity.

Corollary 3.6. *Let $\psi \in L^1 \cap L^2(\mathbb{R}^n)$ be a wavelet satisfying the conditions of Theorem 3.3 and let Q be quadrature operator. If $Q'\psi$ is a hypercomplex wavelet, then it holds for $f \in L^2(\mathbb{R}^n)$*

$$Q' f(x) = \frac{1}{2} \int_0^\infty (Q'\psi_a * Q'\psi_a * f)(x) \frac{\mathrm{d}a}{a}. \tag{3.8}$$

Formula (3.8) has to be understood in the sense of Remark 3.4.

3.1.3 Complex wavelets based on anisotropic primal wavelets

We now look at anisotropic complex wavelet constructions, in particular the classical complex shearlets and the classical complex curvelets, and investigate if their group operations, shearings and rotations, are compatible with the complexification.

Let us first introduce some notation. We denote a counter-clockwise rotation by the angle θ by ρ_θ and its the matrix realization by

$$\rho_\theta = \begin{pmatrix} \cos\theta & -\sin\theta \\ \sin\theta & \cos\theta \end{pmatrix}.$$

Throughout this chapter, we write $(r, \omega) \in \mathbb{R}_0^+ \times [-\pi, \pi]$ for the polar coordinates in $\mathbb{R}^2$. We write also shortly $\mathcal{H}_\theta$ for the partial Hilbert transform with respect to the direction indicated by the angle θ, thus $\mathcal{H}_\theta := \mathcal{H}_{(\cos\theta, \sin\theta)}$.

A simple method of constructing anisotropic wavelets is to multiply the frequency spectrum of an isotropic wavelet by a suitable angular window V. This angular window typically is a smooth function supported in $[-1, 1]$ which satisfies

$$\int_{-1}^{1} V(u)^2 \, \mathrm{d}u = 1. \tag{3.9}$$

When using the rotation group we can construct directional wavelets by using the radial and angular windowing

$$\widehat{\psi_{1,0,0}}(r, \omega) := W(r) \cdot V\left(\frac{N\omega}{2\pi}\right). \tag{3.10}$$

The associated wavelet family consists of the translation, dilations, and rotations the mother wavelet $\psi_{1,0,0}$

$$\psi_{a,b,\theta}(\xi) := \tau_b \delta_a \rho_\theta \psi_{1,0,0}(\xi), \qquad a \in \mathbb{R}^+, b \in \mathbb{R}^2, \theta \in [0, 2\pi).$$

Anisotropic wavelets based on the shearlet group can be constructed in an analogous way.

Although this construction gives us a certain level of anisotropy, the angular resolution remains limited since the level of anisotropy does not increase as the scale parameter decreases. To gain a higher angular resolution, "microlocalizing" wavelet transforms have been proposed in recent years, most prominently curvelets [CD04] and shearlets [LLKW05]. These types of wavelet increase their anisotropy as the scales becomes finer. This way, they are able to resolve orientations more exactly than the wavelet transforms with a fixed degree of anisotropy. Because of these advantage over the simple anisotropic wavelets of (3.10) we focus in the following on curvelets and shearlets.

Complex shearlets Let us start with an observation about shearlets [LLKW05]. The mother shearlet is given by

$$\widehat{\psi^{\mathcal{S}}_{1,0,0}}(\xi_1,\xi_2) = W(\xi_1)V\left(\frac{\xi_1}{\xi_2}\right)$$

The frequency spectrum of the mother shearlet is supported in the halfplane $\{\xi_0\}^{\perp}$, where $\xi_0 = (1,0)$. Hence, by Lemma 2.19, the mother shearlet is a complex signal with respect to the partial Hilbert transform $\mathcal{H}_{\xi_0}$, i.e.,

$$\psi^{\mathcal{S}}_{1,0,0} = \operatorname{Re}\psi^{\mathcal{S}}_{1,0,0} + i\,\mathcal{H}_{\xi_0}\operatorname{Re}\psi^{\mathcal{S}}_{1,0,0}.$$

The shearlet family consists of the atoms

$$\psi^{\mathcal{S}}_{a,b,s}(x) = \tau_b V_{as}\psi^{\mathcal{S}}_{1,0,0}(x), \qquad a\in\mathbb{R}^+, b\in\mathbb{R}^2, s\in\mathbb{R},$$

where V_{as} is the operator induced by the shearing matrix

$$V_{as} = \begin{pmatrix} a & -\sqrt{a}s \\ 0 & \sqrt{a}\end{pmatrix}.$$

Since the partial Hilbert transform commutes with the shearings, cf. Corollary 2.21, the shearlet amplitude is invariant with respect to the group operations of the shearlet transform. Furthermore, shearlets are Schwartz-functions, so in particular integrable. Hence, the complex shearlets are by construction compatible combinations of the partial Hilbert transform and real-valued shearlets.

Complex curvelets Now let us turn to the construction of curvelets [CD05a]. The curvelet family is constructed by the set of basic atoms

$$\widehat{\gamma_{a,0,0}}(r,\omega) \coloneqq a^{\frac{3}{4}}W(ar)V\left(\frac{\omega}{\sqrt{a}}\right), \tag{3.11}$$

where the scale parameter a is smaller than a fixed coarsest scale $\alpha_0 > 0$, for example $\alpha_0 = 1$. Again from Lemma 2.19 it follows that the directional mother curvelets (3.11) are by construction $\mathcal{H}_{\xi_0}$-complex wavelets with $\xi_0 = (1,0)$. Thus the complex-valued mother curvelets can be written as

$$\gamma_{a,0,0} = \beta_{a,0,0} + i\,\mathcal{H}_{\xi_0}\beta_{a,0,0}, \tag{3.12}$$

for every admissible parameter a where $\beta_{a,0,0}$ denotes the real-valued curvelet defined by

$$\beta_{a,0,0} = \operatorname{Re}\gamma_{a,0,0}. \tag{3.13}$$

Up to now, everything is analogous to the shearlets. The difference now comes from the different stearing operation. The curvelet family is set up from rotations instead of shearings, that is,

$$\gamma_{a,b,\theta} = \tau_b\rho_\theta\gamma_{a,0,0}, \qquad a<\alpha_0, b\in\mathbb{R}^2, \theta\in[0,2\pi),$$

and the *curvelet transform*, denoted by Γ_f, is defined by

$$\Gamma_f(a,b,\theta) = \langle f, \gamma_{a,b,\theta}\rangle. \tag{3.14}$$

But the partial Hilbert transform does not commute with the rotations. Indeed, $\mathcal{H}_{(1,0)}\beta_{a,0,\frac{\pi}{2}}$ is in general not even integrable, since the multiplier $\mathrm{M}(\mathcal{H}_{(1,0)})$ has a step singularity at $\mathbb{R}\times\{0\}$. Thus, if we apply the rotation to the mother curvelet $\gamma_{a,0,0}$, we have to adjust also the orientation ξ_0 of the partial Hilbert transform according to Lemma 2.20; so we have only

$$\gamma_{a,b,\theta} = \beta_{a,b,\theta} + i\,\mathcal{H}_{\rho_\theta\xi_0}\beta_{a,b,\theta}, \tag{3.15}$$

where $\beta_{a,b,\theta}(\xi) = \tau_b\rho_\theta\beta_{a,0,0}(\xi)$. So we need in principle a different quadrature operator for every angle. We will remedy this by replacing the partial Hilbert transform in the curvelet construction by the Riesz transform, which is better compatible with rotations, see 2.23.

3.2 The monogenic curvelet transform

We have pointed out in the last section that the partial Hilbert transform is not compatible with the rotations of the continuous curvelet transform (CCT). Moreover, there is the following issue with the partial Hilbert transform construction. To get a full decomposition of a function into curvelet coefficients over all scales, one has to continue the curvelet transform to the coarse scales as well. This can be achieved by purely isotropic wavelets as those in (3.4), so we set

$$\widehat{\gamma_{a,0,0}}(r,\omega) = \begin{cases} a^{\frac{3}{4}}W(ar)V(\frac{\omega}{\sqrt{a}}), & \text{if } a<\alpha_0,\\ a\frac{W(ar)}{\sqrt{\pi}}, & \text{if } a\geq\alpha_0. \end{cases} \tag{3.16}$$

However we have seen that the partial Hilbert transform is not applicable to isotropic wavelets, cf. Section 3.1, thus there is no reasonable complex continuation to the coarse scales. In contrast, we have seen in Section 2.3 and in Section 3.1 that the Riesz transform is compatible with both the rotations and the isotropic wavelets. This motivates to replace the partial Hilbert transform by the Riesz transform in the construction of the curvelets. Thus we construct *monogenic curvelets* $\mathcal{R}'\beta_{ab\theta}$ as $\mathcal{R}'$-complex wavelets from the real-valued curvelets of (3.13), that is,

$$\mathcal{R}'\beta_{ab\theta} := \mathcal{R}'(\beta_{ab\theta}) := \beta_{ab\theta} + \mathbf{e}_1\mathcal{R}_1(\beta_{ab\theta}) + \mathbf{e}_2\mathcal{R}_2(\beta_{ab\theta}). \tag{3.17}$$

Here, $\beta_{a,0,0}$ is the real part of the curvelet $\gamma_{a,0,0}$ for the fine scales $a<\alpha_0$ and a purely radial wavelet at the coarse scales $a\geq\alpha_0$; in the Fourier domain

$$\widehat{\beta}_{a,0,0}(r,\omega) = \begin{cases} a^{\frac{3}{4}}W(ar)V(\frac{\omega}{\sqrt{a}}), & \text{if } a<\alpha_0,\\ a\frac{W(ar)}{\sqrt{\pi}}, & \text{if } a\geq\alpha_0. \end{cases} \tag{3.18}$$

Illustrations of some monogenic curvelets can be found in Figure 3.1 for a fine scale monogenic curvelet and in Figure 3.2 for a coarse scale monogenic curvelet. The monogenic curvelets yield a new quaternion-valued transform, called *monogenic curvelet transform (MCT)*. We define the monogenic curvelet transform M_f by

$$M_f : \begin{cases} \mathbb{R}^+\times\mathbb{R}^2\times[0,2\pi) & \to \mathbb{H},\\ (a,b,\theta) & \mapsto \langle f, \mathcal{R}'\beta_{ab\theta}\rangle, \end{cases} \tag{3.19}$$

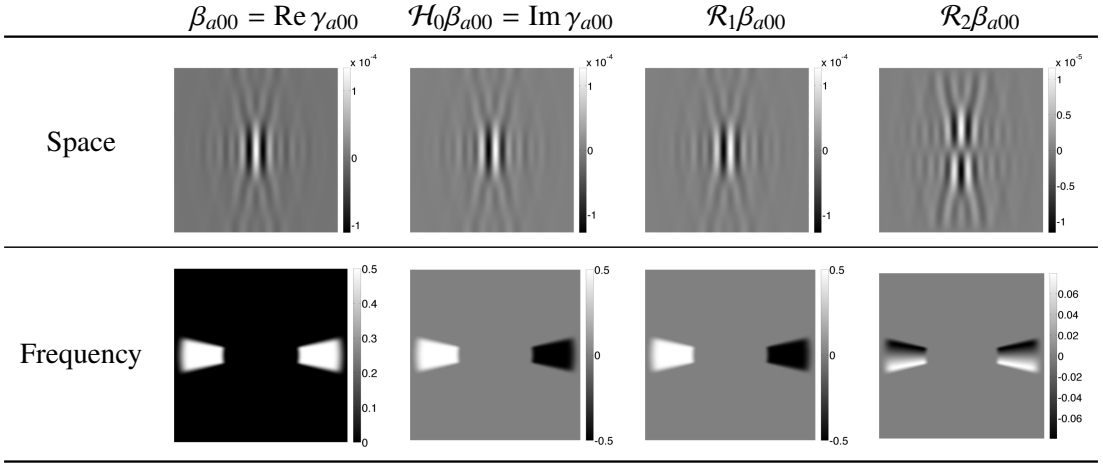

Figure 3.1: Comparison of the atoms of the continuous curvelet transform (CCT) and the monogenic curvelet transform (MCT) at a fine scale. The difference between $\mathcal{H}_0\beta_{a00}$ and $\mathcal{R}_1\beta_{a00}$ can be hardly recognized and the values of $\mathcal{R}_2\beta_{a00}$ are small in comparison to $\mathcal{R}_1\beta_{a00}$. This indicates that the monogenic curvelets and the classical curvelets behave very similar at the fine scales.

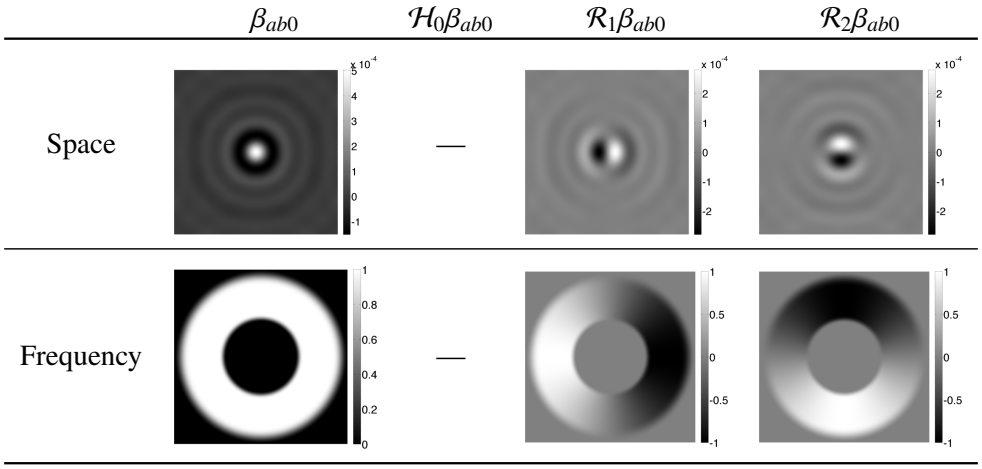

Figure 3.2: Comparison of the atoms of the CCT and the MCT at a coarse scale. The partial Hilbert transform is not reasonable for the isotropic functions thus the classical curvelets are not complex wavelets at the coarse scales. The Riesz transform in contrast is applicable to isotropic functions, hence the monogenic curvelet transform has a reasonable continuation to the coarse scales by complex wavelets. In this figure, we used for reasons of displayability a different scaling than in Figure 3.1.

where

$$\langle f, \mathcal{R}'\beta_{ab\theta}\rangle = \langle f, \beta_{ab\theta}\rangle + \mathbf{e}_1\langle f, \mathcal{R}_1(\beta_{ab\theta})\rangle + \mathbf{e}_2\langle f, \mathcal{R}_2(\beta_{ab\theta})\rangle.$$

Here, the analyzed object f can be a tempered distributions, because $\beta_{ab\theta}$ and $\mathcal{R}_\nu\beta_{ab\theta}$, where $\nu = 1, 2$, are Schwartz-functions.

Like the classical curvelet transform, the monogenic curvelet transform has a reproducing formula and a Parseval formula for square-integrable functions, which have to be understood in the L^2-sense of Remark 3.4.

Theorem 3.7. *Let $f \in L^2(\mathbb{R}^2, \mathbb{R})$. The monogenic curvelets have a Calderón-like reproducing formula*

$$\mathcal{R}' f(x) = \int_0^\infty \int_0^{2\pi} \int_{\mathbb{R}^2} \overline{\langle f, \mathcal{R}'\beta_{ab\theta}\rangle}\mathcal{R}'\beta_{ab\theta}(x)\,\mathrm{d}b\,\mathrm{d}\theta\frac{\mathrm{d}a}{a^3} \tag{3.20}$$

in the L^2-sense and a Parseval formula

$$\|f\|_2^2 = \int_0^\infty \int_0^{2\pi} \int_{\mathbb{R}^2} \left|M_f(a, b, \theta)\right|^2\,\mathrm{d}b\,\mathrm{d}\theta\frac{\mathrm{d}a}{a^3}. \tag{3.21}$$

Proof. We mainly follow the argumentation of [CD05b] with the necessary modifications. Let

$$g_{a\theta}(x) := \int_{\mathbb{R}^2} \overline{\langle f, \mathcal{R}'\beta_{ab\theta}\rangle}\mathcal{R}'\beta_{ab\theta}(x)\,\mathrm{d}b$$

in $L^2(\mathbb{R}^2, \mathbb{R})$. We have to show

$$\mathcal{R}' f(x) = \int_0^\infty \int_0^{2\pi} g_{a\theta}(x)\frac{1}{a^3}\,\mathrm{d}\theta\,\mathrm{d}a \tag{3.22}$$

in $L^2(\mathbb{R}^2, \mathbb{R})$. Let $\widetilde{\ }$ denote the reflection. As $\mathcal{R}'\beta_{ab\theta}(x) = \mathcal{R}'\beta_{a0\theta}(x - b)$ we have

$$\begin{aligned}
g_{a\theta}(x) &= \int_{\mathbb{R}^2} \mathcal{R}'\beta_{a0\theta}(x - b)\overline{\int_{\mathbb{R}^2} \mathcal{R}'\beta_{a0\theta}(y - b)f(y)\,\mathrm{d}y}\,\mathrm{d}b \\
&= \int_{\mathbb{R}^2} \mathcal{R}'\beta_{a0\theta}(x - b)\int_{\mathbb{R}^2} \overline{\mathcal{R}'\beta_{a0\theta}(y - b)}f(y)\,\mathrm{d}y\,\mathrm{d}b \\
&= \int_{\mathbb{R}^2} \mathcal{R}'\beta_{a0\theta}(x - b)\overline{(\widetilde{\mathcal{R}'\beta}_{a0\theta} * f)}(b)\,\mathrm{d}b \\
&= \mathcal{R}'\beta_{a0\theta} * \overline{\widetilde{\mathcal{R}'\beta}_{a0\theta}} * f(x) \\
&= \mathcal{R}'\beta_{a0\theta} * \mathcal{R}'\beta_{a0\theta} * f(x),
\end{aligned}$$

because $\widehat{\beta}_{a0\theta}$ is symmetric with respect to the origin and real valued and hence $\widetilde{\mathcal{R}'\beta}_{a0\theta}(x) = \mathcal{R}'\beta_{a0\theta}(-x) = \overline{\mathcal{R}'\beta_{a0\theta}(x)}$. From Lemma 3.5 follows that

$$\widehat{g_{a\theta}}(\xi) = \mathcal{F}(\mathcal{R}'\beta_{a0\theta} * \mathcal{R}'\beta_{a0\theta} * f)(\xi) = 2\widehat{\beta}_{a0\theta}(\xi)^2\widehat{\mathcal{R}' f}(\xi).$$

Plugging this into (3.22) we get

$$\widehat{\mathcal{R}'f}(\xi) = \int_0^\infty \int_0^{2\pi} \widehat{g}_{a\theta}(\xi)\frac{1}{a^3}\,\mathrm{d}\theta\,\mathrm{d}a = 2\widehat{\mathcal{R}'f}(\xi)\int_0^\infty \int_0^{2\pi} \widehat{\beta}_{a0\theta}(\xi)^2\frac{1}{a^3}\,\mathrm{d}\theta\,\mathrm{d}a.$$

So it remains to show that

$$\int_0^\infty \int_0^{2\pi} \widehat{\beta}_{a0\theta}(\xi)^2\frac{1}{a^3}\,\mathrm{d}\theta\,\mathrm{d}a = \frac{1}{2}. \tag{3.23}$$

We split the integral into the coarse and the fine scales

$$\int_0^\infty \int_0^{2\pi} \widehat{\beta}_{a0\theta}(\xi)^2\frac{1}{a^3}\,\mathrm{d}\theta\,\mathrm{d}a = \int_0^{\alpha_0} \int_0^{2\pi} \widehat{\beta}_{a0\theta}(\xi)^2\frac{1}{a^3}\,\mathrm{d}\theta\,\mathrm{d}a + \int_{\alpha_0}^\infty \int_0^{2\pi} \widehat{\beta}_{a0\theta}(\xi)^2\frac{1}{a^3}\,\mathrm{d}\theta\,\mathrm{d}a.$$

As $\widehat{\beta}_{a0\theta}$ is defined in polar coordinates, we rewrite the equation via $\xi = r(\cos\omega, \sin\omega)$ to get

$$\widehat{\beta}_{a0\theta}(\xi) = \frac{1}{2}W(ar)V\left(\frac{\omega-\theta}{\sqrt{a}}\right)a^{3/4},$$

thus

$$\int_0^{\alpha_0} \int_0^{2\pi} \widehat{\beta}_{a0\theta}(\xi)^2\frac{1}{a^3}\,\mathrm{d}\theta\,\mathrm{d}a = \int_0^{\alpha_0} \int_0^{2\pi} \frac{1}{2}W(ar)^2a^{3/2}V\left(\frac{\omega-\theta}{\sqrt{a}}\right)^2\frac{1}{a^3}\,\mathrm{d}\theta\,\mathrm{d}a. \tag{3.24}$$

The admissibility condition for V yields

$$\int_0^{2\pi} V\left(\frac{\omega-\theta}{\sqrt{a}}\right)^2\,\mathrm{d}\theta = a^{1/2},$$

so (3.24) reduces to

$$\frac{1}{2}\int_0^{\alpha_0} W(ar)^2\frac{1}{a}\,\mathrm{d}a.$$

For the second part we have

$$\int_{\alpha_0}^\infty \int_0^{2\pi} \widehat{\beta}_{a0\theta}(\xi)^2\frac{1}{a^3}\,\mathrm{d}\theta\,\mathrm{d}a = \int_{\alpha_0}^\infty \int_0^{2\pi} \frac{1}{4}W(ar)^2\frac{a^2}{\pi}\frac{1}{a^3}\,\mathrm{d}\theta\,\mathrm{d}a = \int_{\alpha_0}^\infty \frac{1}{2}W(ar)^2\frac{1}{a}\,\mathrm{d}a.$$

After summing up the coarse and the fine scale integrals we get from the admissibility condition (3.3) that

$$\frac{1}{2}\int_0^\infty W(ar)^2\frac{1}{a}\,\mathrm{d}a = \frac{1}{2}\int_0^\infty W(t)^2\frac{r}{t}\frac{1}{r}\,\mathrm{d}t = \frac{1}{2}\int_0^\infty W(t)^2\frac{1}{t}\,\mathrm{d}t = \frac{1}{2},$$

which completes the proof of (3.20).

Now we prove the Parseval formula. To this end, we first calculate

$$\begin{aligned}
\int_{\mathbb{R}^2} |\overline{\mathcal{R}'\beta_{a0\theta}} * f(b)|^2 \,\mathrm{d}b &= \int_{\mathbb{R}^2} |\beta_{a0\theta} * f(b)|^2 + |(\mathcal{R}_1\beta_{a0\theta}) * f(b)|^2| + |(\mathcal{R}_2\beta_{a0\theta}) * f(b)|^2 \,\mathrm{d}b \\
&= \|\beta_{a0\theta} * f\|_2^2 + \|(\mathcal{R}_1\beta_{a0\theta}) * f\|_2^2 + \|(\mathcal{R}_2\beta_{a0\theta}) * f\|_2^2 \\
&= \|\widehat{\beta_{a0\theta}}\hat{f}\|_2^2 + \|\widehat{\mathcal{R}_1\beta_{a0\theta}}\hat{f}\|_2^2 + \|\widehat{\mathcal{R}_2\beta_{a0\theta}}\hat{f}\|_2^2 \\
&= \int_{\mathbb{R}^2} \left|\widehat{\beta_{a0\theta}}(\xi)\hat{f}(\xi)\right|^2 \mathrm{d}\xi + \int_{\mathbb{R}^2} \left|\frac{\xi_1}{|\xi|}\widehat{\beta_{a0\theta}}(\xi)\hat{f}(\xi)\right|^2 \mathrm{d}\xi \\
&\quad + \int_{\mathbb{R}^2} \left|\frac{\xi_2}{|\xi|}\widehat{\beta_{a0\theta}}(\xi)\hat{f}(\xi)\right|^2 \mathrm{d}\xi \\
&= \int_{\mathbb{R}^2} \left(1 + \frac{\xi_1^2}{|\xi|^2} + \frac{\xi_2^2}{|\xi|^2}\right) \left|\widehat{\beta_{a0\theta}}(\xi)\hat{f}(\xi)\right|^2 \mathrm{d}\xi \\
&= 2\int_{\mathbb{R}^2} \left|\widehat{\beta_{a0\theta}}(\xi)\hat{f}(\xi)\right|^2 \mathrm{d}\xi.
\end{aligned}$$

With this identity we get

$$\begin{aligned}
\int \left|\langle f, \mathcal{R}'\beta_{ab\theta}\rangle\right|^2 \,\mathrm{d}b\,\mathrm{d}\theta\frac{\mathrm{d}a}{a^3} &= \int 2\left|\widehat{\beta_{a0\theta}}(\xi)\right|^2 \left|\widehat{f}(\xi)\right|^2 \,\mathrm{d}\xi\,\mathrm{d}\theta\frac{\mathrm{d}a}{a^3} \\
&= 2\int \left|\widehat{f}(\xi)\right|^2 \left(\int \left|\widehat{\beta_{a0\theta}}(\xi)\right|^2 \,\mathrm{d}\theta\frac{\mathrm{d}a}{a^3}\right) \mathrm{d}\xi \\
&= 2\int \left|\widehat{f}(\xi)\right|^2 \frac{1}{2}\,\mathrm{d}\xi = \|f\|_2^2,
\end{aligned}$$

where the last line follows from (3.23). ∎

3.3 Relations between the classical and the monogenic curvelet transform

The goal of this section is to point out the differences and similarities between the classical continuous curvelet transform (CCT) and the new monogenic curvelet transform (MCT). To this end, we first compare the function plots of the classical curvelets and the monogenic curvelets. At the fine scales, one immediately recognizes the similarities between the imaginary part of γ_{a00} and $\mathcal{R}_1\beta_{a00}$ (Figure 3.1). At the coarse scales on the other hand, there is a big difference, because γ_{a00} lacks an imaginary part for $a \geq \alpha_0$ (Figure 3.2). In Figure 3.3, the amplitude and sign (or phase) of the CCT and the MCT are compared.

3.3.1 Uniform convergence of the monogenic to the classical curvelets at fine scales

The MCT is quaternion-valued whereas the CCT is complex-valued, hence they cannot be compared per se. To make them comparable, we isometrically embed the complex values of the curvelets into the quaternions. We define the embedded curvelets $\widetilde{\gamma}_{ab\theta}$ by

$$\begin{aligned}
\widetilde{\gamma}_{ab\theta} &:= \operatorname{Re}\gamma_{ab\theta} + \mathbf{e}_1 \cos(\theta) \operatorname{Im}\gamma_{ab\theta} + \mathbf{e}_2 \sin(\theta) \operatorname{Im}\gamma_{ab\theta} \\
&= \beta_{ab\theta} + \mathbf{e}_1 \cos(\theta)\mathcal{H}_\theta\beta_{ab\theta} + \mathbf{e}_2 \sin(\theta)\mathcal{H}_\theta\beta_{ab\theta}. \qquad (3.25)
\end{aligned}$$

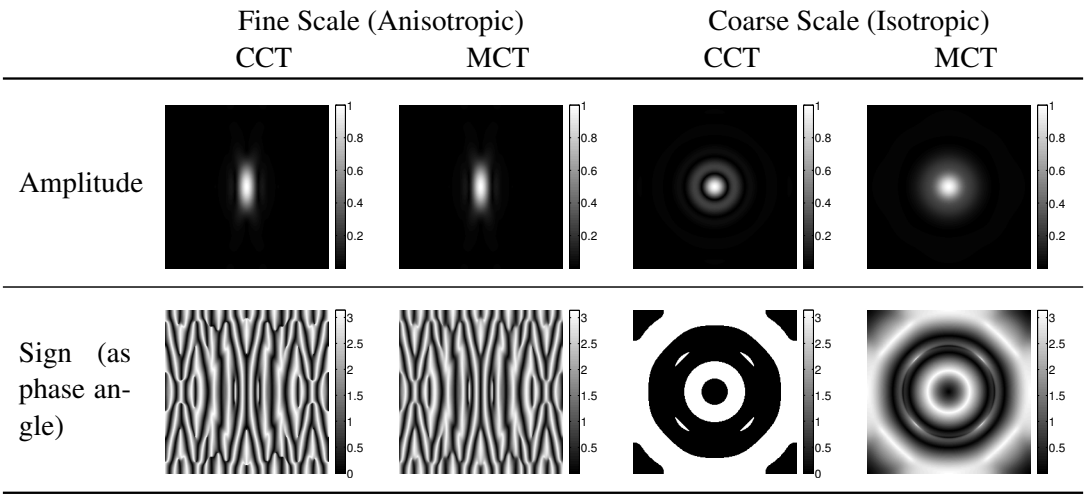

Figure 3.3: Comparison of amplitude and phase responses of the filters in Figure 3.1 and Figure 3.2. There is no visible difference at the fine scale between CCT and MCT. At the coarse scale the CCT-amplitude oscillates and the CCT-sign (phase) is discontinuous whereas the MCT-amplitude decays monotonously and the MCT-sign (phase) is smoother. For reasons of displayability, the sign is depicted as phase angle.

The corresponding embedding of the curvelet coefficients is denoted by

$$\widetilde{\Gamma}_f(a,b,\theta) = \langle f, \widetilde{\gamma}_{ab\theta} \rangle.$$

The canonical embedding $\mathbb{C} \to \mathbb{H}, a + ib \mapsto a + \mathbf{e}_1 b$ is not suitable here, because it is not compatible with the covariant transformation law of the Riesz transform in this setting. With the embedding (3.25) we are able to prove the uniform convergence of the CCT and the MCT (Corollary 3.11). To this end, we need some preliminary lemmas.

Lemma 3.8. *Let* $\Omega_a = \left(\left[-\frac{2}{a}, -\frac{1}{2a}\right] \cup \left[\frac{1}{2a}, \frac{2}{a}\right]\right) \times \left[-\sqrt{a}, \sqrt{a}\right]$ *and* β_{a00} *a real curvelet at scale* a*, where* $0 < a < \alpha_0$*. Then the following statements hold:*

(1) The support of $\widehat{\beta}_{a00}$ *lies in the rectangle* Ω_a*, that is,* $\operatorname{supp} \widehat{\beta}_{a00} \subset \Omega_a$*.*

(2) The measure of $\operatorname{supp} \widehat{\beta}_{a00}$ *has the upper bound* $\mu(\operatorname{supp}(\widehat{\beta}_{a00})) \leq \mu(\Omega_a) = 6a^{-1/2}$*, where* μ *denotes the Lebesgue measure.*

(3) $\left\| \widehat{\beta_{a00}} \right\|_\infty = a^{3/4} \cdot C_{W,V}$ *with a constant* $C_{W,V}$ *depending only on the choice of the window functions* W *and* V*.*

(4) For all $\xi \in \Omega_a$ *we have the inequalities*

$$\frac{|\xi_2|}{|\xi|} \leq 2a^{3/2}$$

and

$$\left| \operatorname{sgn}(\xi_1) - \frac{\xi_1}{|\xi|} \right| \leq 2a^{3/2},$$

which are related to the Fourier multiplier of the Riesz transform. ⌟

Proof. (1) Holds by construction of $\widehat{\beta}_{a00}$.

(2) $\mu(\Omega_a) = 2(\frac{2}{a} - \frac{1}{2a})(2\sqrt{a}) = 4(\frac{4}{2a} - \frac{1}{2a})\sqrt{a} = 4\frac{3}{2a}\sqrt{a} = 6a^{-1}a^{1/2} = 6a^{-1/2}$.

(3) $\left\|\widehat{\beta_{a00}}\right\|_\infty = \sup_{(r,\omega)\in\mathbb{R}^+\times[-1,1]} a^{3/4} W(r)V(\omega) = a^{3/4} \underbrace{\sup_{r\in\mathbb{R}^+} W(r) \sup_{\omega\in[-1,1]} V(\omega)}_{=:C_{W,V}}$.

(4) The first inequality follows from $|\xi_2| \leq \sqrt{a}$ and $|\xi| \geq \frac{1}{2a}$. For the second we have $|\xi| - |\xi_1| \leq |\xi_1| + |\xi_2| - |\xi_1| = |\xi_2| = \sqrt{a}$, thus it follows

$$\left|\operatorname{sgn}\,\xi_1 - \frac{\xi_1}{|\xi|}\right| = \left|\frac{\operatorname{sgn}\,\xi_1\,|\xi| - \xi_1}{|\xi|}\right| = \left|\frac{|\xi| - |\xi_1|}{|\xi|}\right| \leq \frac{\sqrt{a}}{\frac{1}{2a}} = 2a^{3/2}. \qquad \blacksquare$$

In the next lemma, we compute the norm difference between a curvelet and a monogenic curvelet.

Lemma 3.9. *Let $0 < a < \alpha_0$, $b \in \mathbb{R}^2$, and $\theta \in [0, 2\pi)$. For the L^2-distance of the embedded curvelets $\widetilde{\gamma}_{ab\theta}$ and the monogenic curvelets $\mathcal{R}'\beta_{ab\theta}$ we have that*

$$\left\|\widetilde{\gamma}_{ab\theta} - \mathcal{R}'\beta_{ab\theta}\right\|_2^2 = \|\mathcal{H}_0\beta_{a00} - \mathcal{R}_1\beta_{a00}\|_2^2 + \|\mathcal{R}_2\beta_{a00}\|_2^2\,. \qquad \lrcorner$$

Proof. First we calculate

$$\begin{aligned}
\left\|\widetilde{\gamma}_{ab\theta} - \mathcal{R}'\beta_{ab\theta}\right\|_2^2 &= \|\beta_{ab\theta} + \mathbf{e}_1\cos(\theta)\mathcal{H}_\theta\beta_{ab\theta} + \mathbf{e}_2\sin(\theta)\mathcal{H}_\theta\beta_{ab\theta} - \beta_{ab\theta} - \mathbf{e}_1\mathcal{R}_1\beta_{ab\theta} - \mathbf{e}_2\mathcal{R}_2\beta_{ab\theta}\|_2^2 \\
&= \|\mathbf{e}_1(\cos(\theta)\mathcal{H}_\theta\beta_{ab\theta} - \mathcal{R}_1\beta_{ab\theta}) + \mathbf{e}_2(\sin(\theta)\mathcal{H}_\theta\beta_{ab\theta} - \mathcal{R}_2\beta_{ab\theta})\|_2^2 \\
&= \|\cos(\theta)\mathcal{H}_\theta\beta_{ab\theta} - \mathcal{R}_1\beta_{ab\theta}\|_2^2 + \|\sin(\theta)\mathcal{H}_\theta\beta_{ab\theta} - \mathcal{R}_2\beta_{ab\theta}\|_2^2\,.
\end{aligned}$$

Using the intertwining relations of the partial Hilbert transform (2.17) and the Riesz transform (2.20), we compute for the first term

$$\begin{aligned}
\|\cos(\theta)\mathcal{H}_\theta\beta_{ab\theta} - \mathcal{R}_1\beta_{ab\theta}\|_2^2 &= \|\cos(\theta)\mathcal{H}_\theta\rho_\theta\beta_{ab0} - \mathcal{R}_1\rho_\theta\beta_{ab0}\|_2^2 \\
&= \|\cos(\theta)\rho_\theta\mathcal{H}_0\beta_{ab0} - \cos(\theta)\rho_\theta\mathcal{R}_1\beta_{ab0} - \sin(\theta)\rho_\theta\mathcal{R}_2\beta_{ab0}\|_2^2 \\
&= \|\rho_\theta[\cos(\theta)(\mathcal{H}_0\beta_{ab0} - \mathcal{R}_1\beta_{ab0}) - \sin(\theta)\mathcal{R}_2\beta_{ab0}]\|_2^2 \\
&= \|\cos(\theta)(\mathcal{H}_0\beta_{ab0} - \mathcal{R}_1\beta_{ab0}) - \sin(\theta)\mathcal{R}_2\beta_{ab0}\|_2^2\,,
\end{aligned}$$

and analogously for the second term

$$\begin{aligned}
\|\sin(\theta)\mathcal{H}_\theta\beta_{ab\theta} - \mathcal{R}_2\beta_{ab\theta}\|_2^2 &= \|\sin(\theta)\mathcal{H}_\theta\rho_\theta\beta_{ab0} - \mathcal{R}_2\rho_\theta\beta_{ab0}\|_2^2 \\
&= \|\sin(\theta)\rho_\theta\mathcal{H}_0\beta_{ab0} + \sin(\theta)\rho_\theta\mathcal{R}_1\beta_{ab0} - \cos(\theta)\rho_\theta\mathcal{R}_2\beta_{ab0}\|_2^2 \\
&= \|\rho_{-\theta}[\sin(\theta)(\mathcal{H}_0\beta_{ab0} - \mathcal{R}_1\beta_{ab0}) + \cos(\theta)\mathcal{R}_2\beta_{ab0}]\|_2^2 \\
&= \|\sin(\theta)(\mathcal{H}_0\beta_{ab0} - \mathcal{R}_1\beta_{ab0}) + \cos(\theta)\mathcal{R}_2\beta_{ab0}\|_2^2\,.
\end{aligned}$$

Summing up both terms, we get

$$\begin{aligned}
&\|\cos(\theta)(\mathcal{H}_0\beta_{ab0} - \mathcal{R}_1\beta_{ab0}) - \sin(\theta)\mathcal{R}_2\beta_{ab0})\|_2^2 + \|\sin(\theta)(\mathcal{H}_0\beta_{ab0} - \mathcal{R}_1\beta_{ab0}) + \cos(\theta)\mathcal{R}_2\beta_{ab0})\|_2^2 \\
&= \int_{\mathbb{R}^2} (\cos(\theta)(\mathcal{H}_0\beta_{ab0}(x) - \mathcal{R}_1\beta_{ab0}(x)) - \sin(\theta)\mathcal{R}_2\beta_{ab0}(x)))^2 \\
&\quad + (\sin(\theta)(\mathcal{H}_0\beta_{ab0}(x) - \mathcal{R}_1\beta_{ab0}(x)) + \cos(\theta)\mathcal{R}_2\beta_{ab0}(x)))^2 \, \mathrm{d}x \\
&= \int_{\mathbb{R}^2} (\mathcal{H}_0\beta_{ab0}(x) - \mathcal{R}_1\beta_{ab0}(x))^2 + \mathcal{R}_2\beta_{ab0}(x)^2 \, \mathrm{d}x \\
&= \|\mathcal{H}_0\beta_{ab0} - \mathcal{R}_1\beta_{ab0}\|_2^2 + \|\mathcal{R}_2\beta_{ab0}\|_2^2 ,
\end{aligned}$$

where the penultimate equation follows from the trigonometric identity

$$(\cos(\theta)u - \sin(\theta)v)^2 + (\sin(\theta)u + \cos(\theta)v)^2 = u^2 + v^2.$$

The claim follows because both the partial Hilbert transform and the Riesz transform commute with the translations, that is,

$$\|\mathcal{H}_0\beta_{ab0} - \mathcal{R}_1\beta_{ab0}\|_2^2 + \|\mathcal{R}_2\beta_{ab0}\|_2^2 = \|\mathcal{H}_0\beta_{a00} - \mathcal{R}_1\beta_{a00}\|_2^2 + \|\mathcal{R}_2\beta_{a00}\|_2^2 . \qquad \blacksquare$$

Now we can show that the atoms of the classical curvelet transform and the monogenic curvelet transform converge to each other.

Theorem 3.10. *For every $b \in \mathbb{R}^2$, every $\theta \in [0, 2\pi)$ and every $0 < a < \alpha_0$ it holds*

$$\left\|\widetilde{\gamma}_{ab\theta} - \mathcal{R}'\beta_{ab\theta}\right\|_2 \leq a^2 4\sqrt{3} C_{W,V},$$

with a constant $C_{W,V}$ depending only on the choice of the window functions W and V. ⌟

Proof. From Lemma 3.9 we get

$$\left\|\widetilde{\gamma}_{ab\theta} - \mathcal{R}'\beta_{ab\theta}\right\|_2^2 = \|\mathcal{H}_0\beta_{a00} - \mathcal{R}_1\beta_{a00}\|_2^2 + \|\mathcal{R}_2\beta_{a00}\|_2^2 . \tag{3.26}$$

Now we estimate upper bounds for the terms in (3.26), so applying the Plancherel equation and using Lemma 3.8 we get

$$\begin{aligned}
\|\mathcal{H}_0\beta_{a00} - \mathcal{R}_1\beta_{a00}\|_2^2 &= \|\mathcal{F}(\mathcal{R}_1\beta_{a00} - \mathcal{H}_0\beta_{a00})\|_2^2 \\
&= \left\|\widehat{\mathcal{R}_1\beta_{a00}} - \widehat{\mathcal{H}_0\beta_{a00}}\right\|_2^2 \\
&= \int_{\mathbb{R}^2} \left| i \, \frac{\xi_1}{|\xi|}\widehat{\beta}_{a00}(\xi) - i \, \operatorname{sgn} \xi_1 \widehat{\beta}_{a00}(\xi) \right|^2 \mathrm{d}\xi \\
&= \int_{\mathbb{R}^2} \left(\frac{\xi_1}{|\xi|} - \operatorname{sgn} \xi_1 \right)^2 \widehat{\beta}_{a00}(\xi)^2 \, \mathrm{d}\xi \\
&\leq (2a^{3/2})^2 \mu(\operatorname{supp}(\widehat{\beta}_{a00})) \left\|\widehat{\beta}_{a00}\right\|_\infty^2 \\
&= 4a^3 \mu(\operatorname{supp}(\widehat{\beta}_{a00})) \left\|\widehat{\beta}_{a00}\right\|_\infty^2
\end{aligned}$$

and

$$\begin{aligned}\|\mathcal{R}_2\beta_{a00}\|_2^2 = \left\|\widehat{\mathcal{R}_1\beta}_{a00}\right\|_2^2 &= \int_{\mathbb{R}^2}\left(\frac{\xi_2}{|\xi|}\right)^2 \widehat{\beta}_{a00}(\xi)^2\,\mathrm{d}\xi \\ &\leq (2a^{3/2})^2\mu(\mathrm{supp}(\widehat{\beta}_{a00}))\left\|\widehat{\beta}_{a00}\right\|_\infty^2 \\ &= 4a^3\mu(\mathrm{supp}(\widehat{\beta}_{a00}))\left\|\widehat{\beta}_{a00}\right\|_\infty^2 .\end{aligned}$$

Summing up both terms and applying again Lemma 3.8 we get

$$\begin{aligned}\left\|\widetilde{\gamma}_{ab\theta} - \mathcal{R}'\beta_{ab\theta}\right\|_2 &= \sqrt{\|\mathcal{H}_0\beta_{a00} - \mathcal{R}_1\beta_{a00}\|_2^2 + \|\mathcal{R}_2\beta_{a00}\|_2^2} \\ &\leq \sqrt{8a^3\mu(\mathrm{supp}(\widehat{\beta}_{a00}))}\left\|\widehat{\beta}_{a00}\right\|_\infty \\ &\leq \sqrt{8a^3 6a^{-1/2}}\; a^{3/4}C_{W,V} \\ &= \sqrt{48}a^{8/4}\; C_{W,V} \\ &= a^2 4\sqrt{3}\; C_{W,V}\end{aligned}$$

and the proof is complete. ∎

As a consequence, we get that the monogenic curvelet coefficients converge uniformly over scales to the classical curvelets.

Corollary 3.11. *Let $f \in L^2(\mathbb{R}^2, \mathbb{R})$. The classical curvelet coefficients and the monogenic curvelet coefficients converge to each other uniformly in b and θ for $a \to 0$ with the estimate*

$$\left|\widetilde{\Gamma}_f(a,b,\theta) - M_f(a,b,\theta)\right| \leq a^2 4\sqrt{3}C_{W,V}\,\|f\|_2 . \qquad ⌟$$

Proof. By the Cauchy-Schwartz inequality we get

$$\begin{aligned}\left|\widetilde{\Gamma}_f(a,b,\theta) - M_f(a,b,\theta)\right| &= \left|\langle f, \widetilde{\gamma}_{ab\theta}\rangle - \langle f, \mathcal{R}'\beta_{ab\theta}\rangle\right| \\ &= \left|\langle f, \widetilde{\gamma}_{ab\theta} - \mathcal{R}'\beta_{ab\theta}\rangle\right| \\ &\leq \left\|\widetilde{\gamma}_{ab\theta} - \mathcal{R}'\beta_{ab\theta}\right\|_2 \|f\|_2 \\ &\leq a^2 4\sqrt{3}C_{W,V}\,\|f\|_2 .\end{aligned}$$ ∎

Corollary 3.11 shows, that the CCT and the MCT are essentially the same as the scale a is near 0.

3.3.2 Amplitude and sign decomposition by the monogenic curvelet transform

We have seen that the classical curvelet transform and the monogenic curvelet transform are essentially the same at the fine scales. At the coarse scales, in contrast, the transforms differ strongly. The concept of the Hilbert-complex signal is not applicable to the isotropic scales, cf. Section 3.1. Thus, $\gamma_{ab\theta}$ remains a purely real-valued function for $a \geq \alpha_0$. Hence the amplitude $|\gamma_{ab\theta}|$ boils down to the absolute value of the real numbers. In analogy to the one-dimensional

	Anisotropy		Quadrature operator	
	Coarse scales	Fine scales	Coarse scales	Fine scales
Isotropic Monogenic wavelets [OM09, USvdV09, HSMF10]	Low	Low	Riesz transform	Riesz transform
Shearlets [LLKW05]	Low	High (scale-adaptive)	Partial Hilbert transform	Partial Hilbert transform
Classical curvelets [CD05a]	Low	High (scale-adaptive)	—	Partial Hilbert transform
Monogenic Curvelets	Low	High (scale-adaptive)	Riesz transform	Riesz transform

Table 3.1: Comparison between the monogenic wavelets, the classical curvelets, and the monogenic curvelets. Only the monogenic curvelets posses both the high scale-adaptive directionality and a consistent concept of analytic signal over all scales.

example in Figure 2.1, the real absolute value $|\gamma_{ab\theta}|$ oscillates and is non-smooth, even though $\gamma_{ab\theta}$ is smooth; see Figure 3.3, upper row.

The concept of the monogenic signal on the other hand can be applied to all scales, thus $\mathcal{R}'\beta_{ab\theta}$ is a $\mathcal{R}$-complex wavelet also at the coarse scales $a \geq \alpha_0$. Following the arguments of Section 2.1, the amplitude $|\mathcal{R}'\beta_{ab\theta}|$ can be interpreted as envelope of $\beta_{ab\theta}$. We observe that $|\mathcal{R}'\beta_{ab\theta}|$ is slowly varying and does not oscillate (Figure 3.3, upper row), whereas the oscillating part is coded in the sign (or phase), cf. bottom row of Figure 3.3 .

Let us give a remark about the connection of the MCT with other existing transforms. Consider the case $\alpha_0 = \infty$. In that case, the angular windowing never applies, so the real parts of the monogenic curvelets are purely isotropic functions. Thus the monogenic curvelet transform boils down to the isotropic monogenic wavelet transform of [OM09] or, after discretization, to the monogenic wavelet frame of [HSMF10]. Table 3.1 depicts the connections we described in this section.

3.4 Discretization and frames

The discretization of the monogenic curvelet transform directly derives from the discretization of the classical curvelet transform, which we shortly recall here. For further details we refer the reader to [CD05b]. First recall the definition of a frame, cf. [Chr03].

Definition 3.12. A sequence $\{f_k\}_{k=1}^{\infty}$ of elements in a Hilbert space H is a *frame* for H if there exist constants $A, B > 0$ such that

$$A\|f\|^2 \leq \sum_{k=1}^{\infty} |\langle f, f_k\rangle|^2 \leq B\|f\|^2, \quad \text{for all } f \in H. \tag{3.27}$$

The numbers A, B are called *frame bounds*. If we can choose $A = B$ then the frame is called *tight*. A tight frame with $A = B = 1$ is called *Parseval frame.* ⌟

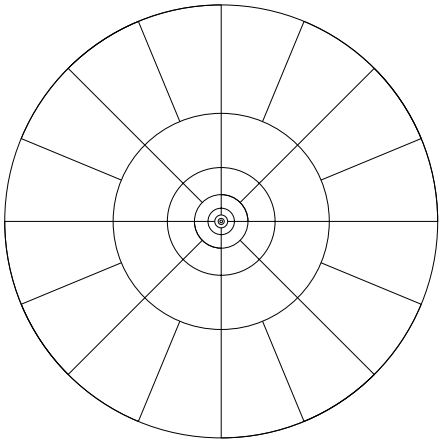

Figure 3.4: Schematic tiling of the frequency plane by the curvelet frame.

The classical curvelet family $\gamma_{ab\theta}$ is discretized as follows. The continuous parameters a, b and θ are replaced by the discrete samples

$$\begin{aligned}
a_j &:= 2^{-j}, \quad j \in \mathbb{Z}, \\
\widetilde{a}_j^{1/2} &:= \frac{1}{2} \cdot 2^{-\lfloor j/2 \rfloor}, \\
\theta_{j,l} &:= \frac{\pi}{2} l \cdot 2^{-\lfloor j/2 \rfloor}, \quad \text{where } l = 0, \ldots, L_j - 1 \text{ with } L_j := 4 \cdot 2^{\lfloor j/2 \rfloor}, \\
b_{k_1,k_2}^{j,l} &:= \begin{cases} \rho_{\theta_{j,l}}(k_1/2^j, k_2/2^{j/2}), & \text{if } j \geq 0, \\ (k_1/2^j, k_2/2^j), & \text{else,} \end{cases}
\end{aligned}$$

where $(k_1, k_2) \in \mathbb{Z}^2$. Notice that the discrete parameters sample the continuous parameters exactly only at every other scale due to the construction of $\widetilde{a}_j$, [CD05b]. The discrete curvelet frame is the family

$$\left\{ \phi_{j,k,l} := \phi_{j,0,0}(\rho_{\theta_{j,l}}(\bullet - b_{k_1,k_2}^{j,l})) : l = 0, \ldots, L_j - 1 \right\}_{j,k_1,k_2 \in \mathbb{Z}},$$

where

$$\widehat{\phi}_{j,0,0}(r, \omega) = \begin{cases} W(a_j r) V\left(\frac{\omega}{\pi \widetilde{a}_j^{1/2}} \right), & \text{if } j \geq 0, \\ W(a_j r), & \text{else.} \end{cases}$$

The curvelet frame yields a tiling of the frequency plane according to the scheme in Figure 3.4.

Note that now W and V have to fulfill slightly different admissibility conditions than in the continuous case, namely

$$\begin{aligned}
\sum_{j=-\infty}^{\infty} W(2^j r)^2 &= 1, \quad \forall\, r \in (3/4, 3/2), \\
\sum_{l=-\infty}^{\infty} V(t - l)^2 &= 1, \quad \forall\, t \in (-1/2, 1/2).
\end{aligned}$$

In order to obtain a tight frame of monogenic curvelets we proceed in the same way as we derived the monogenic curvelets from the classical curvelets in Section 3.2. We symmetrize the basic element $\widehat{\phi}_{j,0,0}$ with respect to the origin by

$$\widehat{\psi}_{j,0,0}(\xi_1,\xi_2) := \frac{1}{2}(\widehat{\phi}_{j,0,0}(\xi_1,\xi_2) + \widehat{\phi}_{j,0,0}(-\xi_1,-\xi_2)).$$

to get a tight frame of real valued functions $\psi_{j,k,l}$, cf. [CD05b]. Because of the symmetry it is sufficient to discretize the angles in the range from $[0,\pi)$, thus we modify L_j to $\widetilde{L}_j := 2\cdot 2^{\lfloor j/2\rfloor}$.

In [HSMF10, Theorem 5.1] and [Hel12], it has been proven that the Riesz transforms maps a frame of real-valued elements into a frame of quaternion-valued elements with the same frame bounds. Thus it follows that the family of monogenic curvelets

$$\left\{\mathcal{R}'\psi_{j,k,l} = \psi_{j,k,l} + \mathbf{e}_1\mathcal{R}_2\psi_{j,k,l} + \mathbf{e}_2\mathcal{R}_2\psi_{j,k,l} : l = 0,\dots,\widetilde{L}_j - 1\right\}_{j,k_1,k_2\in\mathbb{Z}}$$

is a tight frame for $L^2(\mathbb{R}^2,\mathbb{R})$.

3.5 Numerical experiments

It is an important task in image analysis to estimate the local Sobolev regularity at a point $b\in\mathbb{R}^2$ and in a direction $\theta\in[0,\pi]$, denoted by $s_{b,\theta}$. We will see in the next chapter (Subsection 4.1.2) that this can be achieved by estimating the decay rates of the moduli of the curvelet coefficients. To get a stable estimate for the decay rate, the amplitude of the wavelet coefficients must behave well for all available scales a_j; that means, the amplitude should not oscillate. We pointed out in Section 3.3, that the amplitude of the CCT oscillates at the isotropic scales. (Figure 3.3). The experiments in Figure 3.5 illustrate that this behavior leads to artifacts in the estimate of the decay rates. On the other hand, we have seen in Figure 3.3 that the amplitude of the monogenic curvelet transform does not contain oscillations. Thus the estimation by the MCT does not suffer from these artifacts, cf. Figure 3.5.

From a theoretical point of view, only the limit $a_j\to 0$ matters for the estimation of regularity. Thus we usually shall compute the decay rates from the finest scales a_j, which are anisotropic for a sufficient small a_j. However, there are cases where it makes sense to employ also the isotropic scales for the estimation. For example, if for some reason, e.g., runtime, the number of directions at the finest scale is small, say we have only four directions. Then we only have three anisotropic scales available (one time four directions and two times two directions). Hence the anisotropic scales provide only three data points for the computation of $s_{b,\theta}$, which is not sufficient for a robust estimate of $s_{b,\theta}$. In that case, the addition of further data points by using the subsequent isotropic scales leads to a more robust estimation, cf. Figure 3.6.

Let us eventually comment on the window functions W and V. The construction of the curvelet transform requires compactly supported windows, for example the Meyer windows, cf. Section A.2. Despite their good theoretical smoothness properties, these compactly supported windows may not be the first choice in practice. As they are very close to an ideal band-pass filter, the spatial localization is far from optimal, which often causes Gibbs effects. Therefore in applications, we prefer to use windows with better space-frequency localizations. In particular, we here use the radial window defined by

$$W(\xi) = e^{\beta(-\xi^2-\xi^{-2}+1)} \tag{3.28}$$

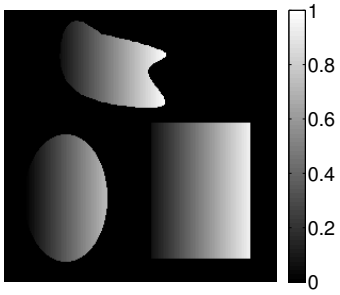

Orientation	Decay rate $s_{\theta,b}$ computed by CCT	Decay rate $s_{\theta,b}$ computed by MCT
$\theta = \frac{\pi}{8}$	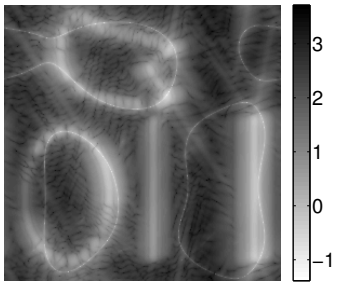	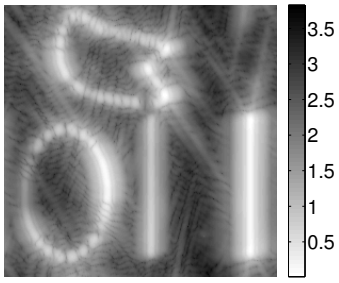
$\theta = \frac{5\pi}{8}$	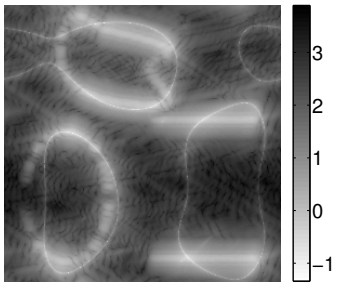	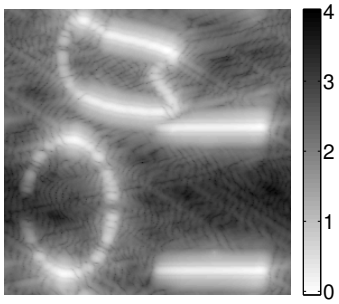
$\inf_{\theta\in[0,2\pi)} s_{b,\theta}$	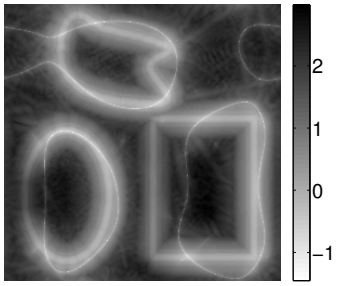	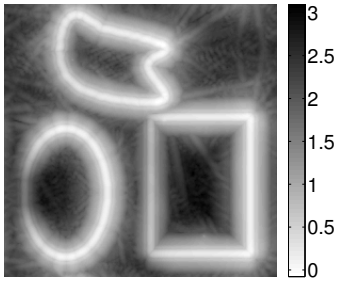

Figure 3.5: Estimation of the regularity by decay rates of curvelet coefficients. The upper image shows the test image. The first two rows display the decay rates over two different orientations, that is the functions $I(b_1, b_2) = s_{\theta,(b_1,b_2)}$ for $\theta = \pi/8$ and $\theta = 5\pi/8$. The lower row shows the minimum of the decay rates, that is, the function $I(b_1, b_2) = \inf_{\theta\in[0,2\pi)} s_{\theta,(b_1,b_2)}$. As also isotropic scales $a_j \geq \alpha_0$ are considered for the estimation, the unstable amplitude of the CCT at the isotropic scales results in artifacts (thin curved lines), whereas the MCT does not suffer from this problem. Note that these artifacts do not occur if we take only the anisotropic scales $a_j < \alpha_0$ for the estimation of $s_{\theta,(b_1,b_2)}$.

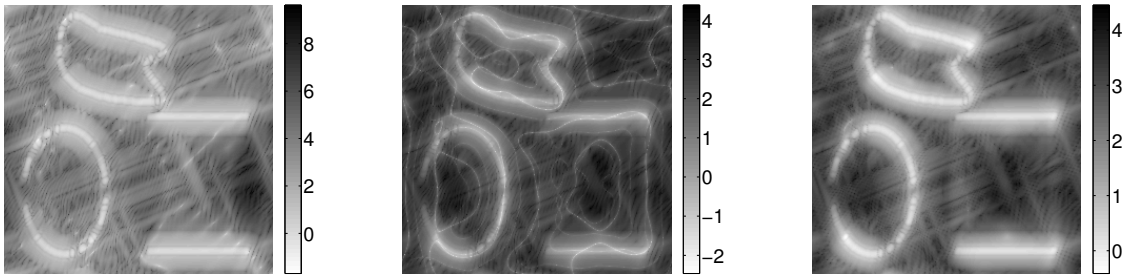

(a) Estimate of $s_{\pi/8,b}$ by the classical curvelet transform using all three anisotropic scales.

(b) Estimate of $s_{\pi/8,b}$ by the classical curvelet transform using all three anisotropic scales and the two subsequent isotropic scales.

(c) Estimate of $s_{\pi/8,b}$ by the monogenic curvelet transform using all three anisotropic scales and the two subsequent isotropic scales.

Figure 3.6: Estimate of $s_{\pi/8,b}$ by the curvelet transform with four directions at the finest scales. The estimation by the classical curvelet transform (a) using only the anisotropic scales oscillates strongly. Using also the subsequent two isotropic scales (b) results in artifacts as explained in Figure 3.5. The estimation by the monogenic curvelet transform using the anisotropic and two subsequent isotropic scales is much smoother than the result of (a) and does not suffer from the artifacts of (b).

where $\beta = \frac{1}{4}$.[2] This window behaves like a Gaussian window for high frequencies, so the space-frequency localization is rather good. Clearly, it lacks the compact frequency support, but is decays rapidly as $|\xi| \to \infty$ and $|\xi| \to 0$. As angular window, we used in all our experiments the classical Meyer window, cf. Section A.2.

3.6 Further references

Monogenic wavelets based on isotropic wavelets and the Riesz transform have been proposed in [OM09, USvdV09, HSMF10] and were applied to AM/FM analysis [USvdV09] or descreening and equalization of brightness [HSMF10]. However, image analysis often requires anisotropy, e.g., for the analysis of edge orientations. To that end, Olhede and Metikas [OM09] gain anisotropy by a directional wavelet transform with a fixed number of orientations. Unser and van de Ville propose in [UvdV09] higher order Riesz transforms, which lead to an approach similar to the steerable filters of Freeman and Adelson [FA91]. However, the degree of anisotropy of these approaches does not increase with scale, thus the resolution of the orientations of the singularities still has some uncertainty. In terms of microlocal analysis, cf. Chapter 4, these transforms do not resolve the wavefront set [CD05a].

Eventually, we provide in Table 3.2 an overview of the reasonable combinations of quadrature operators and wavelet transforms that we have seen in this chapter.

[2] This wavelet was communicated by S. Held [Hel10].

Primal wavelet type	Proper quadrature operator	Example
Isotropic	$\mathcal{R}$	Monogenic wavelets [USvdV09, HSMF10, OM09]
Anisotropic with shearing group	$\mathcal{H}_{\xi_0}$	Shearlets [LLKW05]
Anisotropic with rotation group	$\mathcal{R}$	Anisotropic monogenic wavelets [OM09], Monogenic curvelets (this work)

Table 3.2: Proper quadrature operators for selected wavelet constructions and examples.

Chapter 4

The wavelet amplitude for image analysis – Microlocal analysis and application to separation of edges in x-ray images

It is a classical finding in wavelet theory that the local degree of smoothness of a function can be determined by the decay rates of the amplitudes of the wavelet coefficients [Mal09, Ch. 6]. The connection between classical microlocal analysis and the amplitudes of curvelet coefficients has been established in the work of Candès and Donoho [CD05a]. They showed that the decay rates of the curvelet coefficient's amplitudes $|\langle f, \gamma_{ab\theta}\rangle|$ w.r.t. the scale a are directly related to the *wavefront set*. The wavefront set is the classical approach to the directional analysis of singularities[Hö03]. Analogous results have been shown for the shearlet transform by Kutyniok and Labate [KL09]. This characterization implies that the information we actually extract from the amplitudes of "microlocalizing" wavelet transforms (curvelets and shearlets) is coded in the wavefront set. With this insight, the problem of local image analysis by the amplitudes of (microlocalizing) wavelet transforms is directly connected to the analysis of the wavefront set.

In this chapter, we derive and analyze an new algorithm for the separation of crossing edges in x-ray images within the framework of microlocal analysis. In order to analyze our method we set up a suitable edge model based on the microlocal analysis of manifolds with corners. The connection to the decay rates of the curvelets amplitude enables us to numerically estimate the wavefront set. The chapter is organized as follows. In Section 4.1, we give a short introduction to the wavefront set. We describe its characterization by the decay rates of the curvelet amplitudes, and provide a least squares method for their estimation. In Section 4.2 we motivate and describe our method for the separation of edges in x-ray images. There we observe that the wavefront set of a single edge is connected in the space of locations and orientations (phase space), whereas two (non-tangential) crossing edges are disconnected. Thus, we can separate overlaying edges in x-ray images by a connected component analysis of the wavefront set. In Section 4.3, we mathematically analyze the proposed algorithm. To this end, we introduce an edge model based on the microlocal analysis of distributions acting on test functions by integration over manifolds with corners (Theorem 4.39). Loosely speaking, we say that a distribution defines an edge if its wavefront set has the structure of a (geometric) normal bundle of a manifold with corners (Definition 4.41). Using this edge model, we prove the functionality of our algorithm in a continuous setting, cf. Theorem 4.54.

Some preliminary results of this chapter have been announced in the short communication [Sto11b].

4.1 The wavelet amplitude for microlocal analysis of images

The *wavefront set* is the classical approach to define the orientation of a singularity. The wavefront set of a distribution f on $\mathbb{R}^n$ lives in the so called *phase space* $\mathbb{R}^n \times (\mathbb{R}^n \setminus \{0\})$, where the first component is a location and the second component is a direction.[1] Loosely speaking, a phase space vector (x, ξ) belongs to the wavefront set, if f is locally not smooth at x in the direction of ξ.

In the first part of this section, a short introduction to the wavefront set and its most important properties is given. We also recall the more refined notion of the H^s-wavefront set which is used for measuring the directional (Sobolev) regularity. In the second part we provide the connection to the decay rates of "microlocalizing" wavelet transforms, as established in [CD05a] for the curvelet and in [KL09] for the shearlet transform. This duality makes the computation of the wavefront set algorithmically tractable.

4.1.1 Determination of directional smoothness by the wavefront set

We recall the definition of the wavefront set of a distribution where we mainly follow the textbooks [Hö03, FJ98, Pet83, Sog93]. We start by introducing some notation. Throughout this chapter Ω and Ω' denote open subsets of $\mathbb{R}^n$. We say that a set $\Gamma \subset \mathbb{R}^n \setminus \{0\}$ is *conic* if for every $\xi \in \Gamma$ and every $t > 0$ it holds that $t\xi \in \Gamma$. We call Γ an *open cone* if Γ is conic and open. Likewise, we call a subset A of $\Omega \times (\mathbb{R}^n \setminus \{0\})$ *conic* if it is conic in the second variable, that is, if it $(x, \xi) \in A$ implies that $(x, t\xi) \in A$ for every $t > 0$. We say that $N \subseteq \mathbb{R}^n \setminus \{0\}$ is a *conic neighborhood* of $B \subseteq N$ if N is conic and if there is an open set O such that $B \subseteq O \subseteq N$.

We further say that a function g defined on $\mathbb{R}^n$ *decays rapidly* in a conic subset Γ of $\mathbb{R}^n$ if for every $N \in \mathbb{N}$ exists a constant $C_N > 0$ such that

$$|g(\xi)| \leq C_N (1 + |\xi|)^{-N}, \text{ for all } \xi \in \Gamma.$$

For $(x, \xi) \in \Omega \times (\mathbb{R}^n \setminus \{0\})$, we denote the projection onto the first variable by π_1 and the projection onto the second variable by π_2, that is,

$$\pi_1(x, \xi) = x \quad \text{and} \quad \pi_2(x, \xi) = \xi.$$

The definition of the wavefront set relies on the frequency set, which describes the set of singular directions of a distribution.

Definition 4.1. Let $f \in \mathcal{E}'(\Omega)$ be a distribution with compact support. The *frequency set,* denoted by $\Sigma(f) \subseteq \mathbb{R}^n \setminus \{0\}$, is the set of those $\xi \in \mathbb{R}^n \setminus \{0\}$ having no conic neighborhood to which the restriction of $\widehat{f}$ is of rapid decay. More formally,

$$\xi \notin \Sigma(f) :\Longleftrightarrow \text{there is a conic neighborhood } \Gamma \text{ of } \xi \text{ such that } \widehat{f}\,|_\Gamma \text{ is of rapid decay.} \qquad \lrcorner$$

[1] Since we use the term phase in this work also in a different context we note that the phase space is not related to the phase (angle) of a complex number.

Remark 4.2. Let $f \in \mathcal{E}'(\Omega)$ be a distribution with compact support. Since $\Sigma(f)$ is a conic set, its elements are determined on the unit sphere $\Sigma(f) \cap \mathbb{S}^{n-1}$. Hence we may consider $\Sigma(f)$ as a subset of $\mathbb{S}^{n-1}$. This justifies to call the elements of $\Sigma(f)$ *directions.*

Now assume that $f \in \mathcal{E}'(\Omega)$ is a real-valued distribution, that is, $\langle f, \psi \rangle \in \mathbb{R}$ for every real-valued C^∞-function $\psi \in \mathcal{E}(\Omega)$. Then the absolute value of Fourier transform $\hat{f}$ is symmetric with respect to the origin, that is,

$$|\widehat{f}(-\xi)| = |\widehat{f}(\xi)|, \qquad \text{for all } \xi \in \mathbb{R}^n.$$

In consequence, the frequency set $\Sigma(f)$ is symmetric with respect to the origin, so $\xi \in \Sigma(f)$ if and only if $\lambda\xi \in \Sigma(f)$ for every $\lambda \neq 0$. So we identify all points lying on a line passing through the origin by the equivalence relation

$$\xi \sim \eta \;:\Leftrightarrow\; \exists t \neq 0 :\; \eta = t\xi. \tag{4.1}$$

and consider the frequency set $\Sigma(f)$ as a subset of the *real projective space* $\mathbb{P}^{n-1} := \mathbb{R}^n/_\sim$. Whenever we consider $\Sigma(f)$ as a subset of $\mathbb{P}^{n-1}$, we implicitly assume that f is real-valued and we denote this with a tilde as superscript, i.e.,

$$\widetilde{\Sigma}(f) \;\subset \mathbb{P}^{n-1}.$$

We call the elements of $\widetilde{\Sigma}(f)$ also *orientations.* ⌟

We achieve spatial localization of the frequency set around some point $x_0 \in \Omega$ by computing the frequency set in a small neighborhood U of x_0. To this end, we multiply f by some smooth cutoff function $\psi \in \mathcal{D}(U)$ centered around x_0 and examine the frequency set $\Sigma(\psi f)$. It seems natural that the multiplication with the smooth function ψ does not introduce new singularities. Indeed, the following is true, cf. [Hö03, Theorem 8.1.1].

Lemma 4.3. *Let $\psi \in \mathcal{D}(\mathbb{R}^n)$ be a test function and $f \in \mathcal{E}'(\mathbb{R}^n)$ be a distribution with compact support. Then*

$$\Sigma(\psi f) \subset \Sigma(f).$$ ⌟

Now we may define the localized frequency set.

Definition 4.4. Let $f \in \mathcal{D}'(\Omega)$ be a distribution and let $x \in \Omega$. We define the *localized frequency set,* denoted by $\Sigma_x(f) \subset \mathbb{R}^n \setminus \{0\}$, by

$$\Sigma_x(f) = \bigcap_{\psi \in \mathcal{D}(\Omega), \psi(x) \neq 0} \Sigma(\psi f).$$ ⌟

The localized frequency set $\Sigma_x(f)$ contains the singular directions of f at x. It is empty if f is smooth at x. In fact, $x \in \operatorname{sing\,supp} f$ if and only if $\Sigma_x(f) \neq \emptyset$. The wavefront set is the bundle of all localized frequency sets.

Definition 4.5. Let $f \in \mathcal{D}'(\Omega)$. The *wavefront set* of f, denoted by $\mathrm{WF}(f) \subset \Omega \times \mathbb{R}^n \setminus \{0\}$, is defined by

$$\mathrm{WF}(f) = \bigcup_{x \in \operatorname{sing\,supp} f} \{x\} \times \Sigma_x(f).$$ ⌟

The wavefront set is a closed conic subset of $\Omega \times (\mathbb{R}^n \setminus \{0\})$ since its complement is a union of open sets. As mentioned in Remark 4.2 we may consider the localized frequency set $\Sigma_x(f)$ of a real-valued distribution f as a subset of $\mathbb{P}^{n-1}$. Likewise, we may consider $\mathrm{WF}(f)$ as a subset of $\Omega \times \mathbb{P}^{n-1}$. Whenever we do so, we use the notation

$$\widetilde{\mathrm{WF}}(f) \subset \Omega \times \mathbb{P}^{n-1}. \tag{4.2}$$

A very important property of the wavefront set is that it obeys the transformation law of a covector. To give the precise statement about the transformation law of the wavefront, we require the notion of pullbacks.

Definition 4.6. Let Ω, Ω' be open subsets of $\mathbb{R}^n$ and $\Phi : \Omega \to \Omega'$ a C^1-diffeomorphism. The *pullback* Φ^* of a subset U' of $\Omega' \times \mathbb{R}^n \setminus \{0\}$ is defined by

$$\Phi^* U' = \{(x, \xi) \in \Omega \times \mathbb{R}^n \setminus \{0\} : (\Phi(x), (\mathrm{d}\Phi_x^T)^{-1}\xi) \in U'\}. \tag{4.3}$$

The pullback of a function f is given by $\Phi^* f = f \circ \Phi$. Its natural extension to distributions is defined as follows, cf. [Sog93, p. 32].

Definition 4.7. Let Ω, Ω' be open subsets of $\mathbb{R}^n$, $\Phi : \Omega \to \Omega'$ be a C^∞-diffeomorphism, $\psi \in \mathcal{D}(\Omega)$ and $f \in \mathcal{D}'(\Omega')$. We define the operator $\Phi_* : \mathcal{D}(\Omega) \to \mathcal{D}(\Omega')$, called the *pushforward operator* of Φ, by

$$\Phi_* \psi(x') = (\psi \circ \Phi^{-1})(x') \,|\det \mathrm{d}\Phi_{x'}^{-1}|. \tag{4.4}$$

The *pullback operator* $\Phi^* : \mathcal{D}'(\Omega') \to \mathcal{D}'(\Omega)$ *of* Φ is defined by the duality

$$\langle \Phi^* f, \psi \rangle = \langle f, \Phi_* \psi \rangle. \tag{4.5}$$

By these definitions, the change of variable theorem for the wavefront set can be formulated in the following compact form, see [Sog93, Theorem 0.4.6].

Theorem 4.8. *Let Ω, Ω' be open subsets of $\mathbb{R}^n$ and $\Phi : \Omega \to \Omega'$ be a C^∞-diffeomorphism. Then, for any distribution $f \in \mathcal{D}'(\Omega')$ it holds that*

$$\mathrm{WF}(\Phi^* f) = \Phi^* \,\mathrm{WF}(f). \qquad \lrcorner$$

Recall that a phase space points (x, ξ) belongs to the wavefront set of f if f is not smooth (C^∞) at x in direction ξ. In order to differentiate between degrees of directional smoothness, we use the notion of H^s-wavefront, where $s \in \mathbb{R}$. Loosely speaking, a phase space point (x_0, ξ_0) is not in the H^s-wavefront set of f if f is a H^s-function locally at x_0 and into direction ξ_0. Before going to the definition of the H^s-wavefront, we require some notation. For $\xi \in \mathbb{R}^n$ we write

$$\langle \xi \rangle := (1 + |\xi|^2)^{\frac{1}{2}}.$$

We say that $f \in L^2(\mathbb{R}^n, \langle \bullet \rangle^{2s})$ if

$$\int_{\mathbb{R}^n} |f(\xi)|^2 \langle \xi \rangle^{2s} \mathrm{d}\xi < \infty.$$

A tempered distribution $f \in \mathcal{S}'(\mathbb{R}^n)$ belongs to the Sobolev space $H^s(\mathbb{R}^n)$ if $\hat{f}$ is a function and

$$\|f\|_s^2 := \int_{\mathbb{R}^n} |\hat{f}(\xi)|^2 \langle \xi \rangle^{2s} \, \mathrm{d}\xi < \infty.$$

We denote the space of compactly supported H^s-distributions by H_c^s,

$$H_c^s = \{f \in H^s : \operatorname{supp} f \text{ compact}\}.$$

Further, we define the space of distributions which are locally in H^s by

$$H_{\mathrm{loc}}^s = \{f \in \mathcal{D}'(\Omega) : \phi f \in H^s \text{ for all } \phi \in \mathcal{D}(\Omega)\}.$$

The definition of the H^s-wavefront set derives from the definition of the classical wavefront set by merely replacing the term "rapid decay" by "$\in L^2(\mathbb{R}^n, \langle \bullet \rangle^{2s})$".

Definition 4.9. Let $f \in \mathcal{E}'(\Omega)$ be a distribution with compact support. The *H^s-frequency set,* denoted by $\Sigma^s(f) \subseteq \mathbb{R}^n \setminus \{0\}$, is the set of those $\xi \in \mathbb{R}^n \setminus \{0\}$ having no conic neighborhood to which the restriction of $\widehat{f}$ is in $L^2(\mathbb{R}^n, \langle \bullet \rangle^{2s})$. More formally,

$$\xi \notin \Sigma^s(f) :\Longleftrightarrow \text{there is a conic neighborhood } \Gamma \text{ of } \xi \text{ such that } \widehat{f}\,|_\Gamma \in L^2(\mathbb{R}^n, \langle \bullet \rangle^{2s}). \qquad \lrcorner$$

The H^s-wavefront set is defined as follows.

Definition 4.10. Let $f \in \mathcal{D}'(\Omega)$. The *localized H^s-frequency set* $\Sigma_x^s(f)$ for $x \in \Omega$ is defined by

$$\Sigma_x^s(f) = \bigcap_{\psi \in \mathcal{D}'(\Omega), \psi(x) \neq 0} \Sigma^s(\psi f).$$

The *H^s-wavefront set* $\mathrm{WF}^s(f) \subset \Omega \times (\mathbb{R}^n \setminus \{0\})$ is the bundle of the localized H^s-frequency sets

$$\mathrm{WF}^s(f) = \bigcup_{x \in \Omega} \{x\} \times \Sigma_x^s(f). \qquad \lrcorner$$

Remark 4.11. In the literature we also find the following three notations expressing the fact $(x_0, \xi_0) \notin \mathrm{WF}^s(f)$, namely "$f$ is in H^s at (x_0, ξ_0)", "$f \in H^s(x_0, \xi_0)$" ([Hö85, CD05a]) and "f is microlocally in H^s at (x_0, ξ_0)" ([Pet83]). $\lrcorner$

Petersen [Pet83, Theorem 6.1] gives the following convenient characterization of the H^s-wavefront set.

Theorem 4.12. *Let $f \in \mathcal{D}'(\Omega)$, $(x_0, \xi_0) \in \Omega \times (\mathbb{R}^n \setminus \{0\})$, and $s \in \mathbb{R}$. Then $(x_0, \xi_0) \notin \mathrm{WF}^s(f)$ if and only if there exists $f_1 \in H_{\mathrm{loc}}^s(\Omega)$ and $f_2 \in \mathcal{D}'(\Omega)$ such that $f = f_1 + f_2$ and $(x_0, \xi_0) \notin \mathrm{WF}(f_2)$. Moreover we may choose $f_1 \in H_c^s(\Omega) := H^s \cap \mathcal{E}'(\Omega)$.* $\lrcorner$

This characterization has some immediate consequences.

Corollary 4.13. *Let $\psi \in \mathcal{D}(\mathbb{R}^n)$ be a test function and $f \in \mathcal{D}'(\mathbb{R}^n)$ be a distribution. Then*

$$\mathrm{WF}^s(\psi f) \subset \mathrm{WF}^s(f). \qquad \lrcorner$$

Proof. Let $(x_0, \xi_0) \notin \mathrm{WF}^s(f)$. By Theorem 4.12 there is $f_1 \in H^s_{\mathrm{loc}}(\Omega)$ and $f_2 \in \mathcal{D}'(\Omega)$ with $(x_0, \xi_0) \notin \mathrm{WF}^s(f_2)$. such that $f = f_1 + f_2$. We note that H^s is invariant under the multiplication of a test function (cf. [ES97, Theorem 14]), hence $\psi f_1 \in H^s(\Omega)$. From Lemma 4.3 follows $(x_0, \xi_0) \notin \mathrm{WF}(\psi f_2)$. Using again Theorem 4.12, we get that $(x_0, \xi_0) \notin \mathrm{WF}^s(\psi f)$. ∎

From Theorem 4.12, Theorem 4.8, and the fact that H^s_c is invariant under smooth diffeomorphisms (cf. [Pet83, Ch. 4, Theorem 6.9]) follows that also the H^s-wavefront set is invariant under smooth diffeomorphisms, see [Pet83, Ch. 4, Theorem 6.10].

Corollary 4.14. *Let Ω, Ω' be open subsets of $\mathbb{R}^n$ and $\Phi : \Omega \to \Omega'$ be a smooth diffeomorphism. Then, for any distribution $f \in \mathcal{D}'(\Omega')$ it holds that*

$$\mathrm{WF}^s(\Phi^* f) = \Phi^* \, \mathrm{WF}^s(f)$$ ⌟

We will later also use the fact that the classical wavefront set is the closure of the union of all H^s-wavefront sets

$$\mathrm{WF}(f) = \overline{\bigcup_{s \in \mathbb{R}} \mathrm{WF}^s(f)}, \tag{4.6}$$

see [Pet83, Ch. 4, Theorem 6.3].

Following [Hö85, p. 91], we define a local regularity function indicating for every point $(x_0, \xi_0) \in \Omega \times \mathbb{R}^n \setminus \{0\}$ the maximal directional smoothness index, that is, the maximal $s \in \mathbb{R}$ such that f is in H^s at (x_0, ξ_0).

Definition 4.15. Let $f \in \mathcal{D}'(\Omega)$. The *directional regularity function* $s^*_f : \Omega \times (\mathbb{R}^n \setminus \{0\}) \to \mathbb{R} \cup \{\infty\}$ is defined by

$$s^*_f(x, \xi) = \sup\{s \in \mathbb{R} : (x, \xi) \notin \mathrm{WF}^s(f)\}.$$ ⌟

At this point, expressing s^*_f in terms of the notation given in Remark 4.11, i.e.,

$$s^*_f(x, \xi) = \sup\{s \in \mathbb{R} : f \in H^s(x, \xi)\},$$

may give a more intuitive understanding (see [Hö85, p. 91].)

Since $\mathrm{WF}^s(f)$ is conic in $\Omega \times (\mathbb{R}^n \setminus \{0\})$, the regularity function is positively homogeneous of degree 0 in the second variable, so s^*_f can be regarded as a spherical function $s^*_f : \Omega \times \mathbb{S}^{n-1} \to \mathbb{R} \cup \{\infty\}$. If we additionally assume f to be real-valued, then s^*_f is even in the second variable, hence the domain of s^*_f can be identified with $\Omega \times \mathbb{P}^{n-1}$. In that case, we write $s^*_f : \Omega \times \mathbb{P}^{n-1} \to \mathbb{R} \cup \{\infty\}$ with

$$s^*_f(x, \theta) = \sup\{s \in \mathbb{R} : (x, \theta) \notin \widetilde{\mathrm{WF}}^s(f)\}.$$

The directional regularity function s^*_f contains rich information about the singularities of a distribution. So for a detailed analysis of signals and images, it is highly desirable to compute an estimate to s^*_f, which will be treated in the following.

4.1.2 Resolution of the wavefront set by amplitude coefficients of parabolic scaling transforms

Up to now, there is no obvious way to compute the wavefront set or the directional regularity function for an arbitrary tempered distribution. The difficulty in computing the wavefront set lies in the several limiting processes involved. The first one is the localization in space, the second one is the micro-localization with respect to direction, and the third one is the determination of the decay rate. It was proven in [CD05a] that these three limiting processes can be bundled into one single limiting processes $a \to 0$ using the curvelet transform, cf. (3.14) for its definition. Indeed there is a one-to-one correspondence between the decay rates of the curvelet coefficients and the wavefront set of a tempered distribution, which is stated in the following theorem, cf. [CD05a, Theorem 5.2]. Note that the second component of the wavefront set is identified with the sphere, that is, $\xi \in \mathbb{R}^2 \setminus \{0\}$ is represented by an angle between $[0, 2\pi)$, compare Remark 4.2.

Theorem 4.16. *Let f be a tempered distribution and*

$$\mathscr{R} := \{(x_0, \theta_0) \in \mathbb{R}^2 \times [0, 2\pi) : \Gamma_f \text{ decays rapidly near } (x_0, \theta_0) \text{ as } a \to 0\}.$$

Then $\mathrm{WF}(f)$ *is the complement of $\mathscr{R}$, that is,* $\mathrm{WF}(f) = (\mathbb{R}^2 \times [0, 2\pi)) \setminus \mathscr{R}$. ⌟

There is even a one-to-one correspondence between curvelet coefficients and the H^s-wavefront set, see [CD05a, Theorem 5.3]:

Theorem 4.17. *Let f be a tempered distribution and let $s \in \mathbb{R}$. Let $T^s(x, \theta)$ denote the square function*

$$T^s(x, \theta) = \left(\int_0^{\alpha_0} |\Gamma_f(a, x, \theta)|^2 a^{-2s} \frac{\mathrm{d}a}{a^3} \right)^{1/2}.$$

It holds that $(x_0, \theta_0) \notin \mathrm{WF}^s(f)$ if and only if

$$\int_{\mathcal{N}} (T^s(x, \theta))^2 \, \mathrm{d}x \, \mathrm{d}\theta < \infty$$

for some neighborhood $\mathcal{N}$ of (x_0, θ_0). ⌟

Remark 4.18. Kutyniok and Labate [KL09] showed results analogously to Theorem 4.16 and Theorem 4.17 for the complex shearlet transform. ⌟

Theorem 4.17 gives a precise connection between the asymptotic behavior of the amplitude of the curvelet coefficients and the local Sobolev regularity. In particular, with the curvelet transform (or alternatively the shearlet transform) we have a tool at hand to actually compute the directional regularity function s_f^* with a reasonable effort.

4.1.3 Numerical estimation of the wavefront set by curvelet amplitude regression

We now describe how we may estimate the directional regularity s_f^* in the discrete setting using the curvelet transform. To this end, assume that the curvelet transform is sampled at the discrete

values a_j, θ_l, and b_k. Since we are in discrete setting we may choose the neighborhood $\mathcal{N}$ of Theorem 4.17 as the discrete point (b_k, θ_l). Then, the condition of Theorem 4.17 reduces to

$$\int_0^{\alpha_0} |\Gamma_f(a, b_k, \theta_l)|^2 a^{-2s} \frac{\mathrm{d}a}{a^3} < \infty. \tag{4.7}$$

To estimate $s_f^*(b_k, \theta_l)$, we determine the maximum value s such that (4.7) is true. After the change of variable $u = a^{-1}$ this is equivalent to

$$\int_{\frac{1}{\alpha_0}}^{\infty} |\Gamma_f(u^{-1}, b_k, \theta_l)|^2 u^{2s+1} \, \mathrm{d}u < \infty. \tag{4.8}$$

A sufficient condition for the integral (4.8) to exist is that the integrand decays faster than u^{-1}. Thus the integral exists if there is $u_0 > \alpha_0^{-1}$ and $C > 0$ such that

$$\begin{aligned} & |\Gamma_f(u^{-1}, b_k, \theta_l)|^2 u^{2s+1} \leq C^2 \cdot u^{-1-\epsilon} \\ \Leftrightarrow \quad & |\Gamma_f(u^{-1}, b_k, \theta_l)|^2 \leq C^2 \cdot u^{-2-\epsilon-2s} \\ \Leftrightarrow \quad & |\Gamma_f(u^{-1}, b_k, \theta_l)| \leq C \cdot u^{-s-1-\epsilon/2} \end{aligned}$$

for every $u > u_0$ and every $\epsilon > 0$. The resubstitution $u = a^{-1}$ gives

$$|\Gamma_f(a, b_k, \theta_l)| \leq C \cdot a^{s+1+\epsilon/2}. \tag{4.9}$$

To estimate s from discrete samples $\Gamma_f(a_j, b_k, \theta_l)$, $j = 0, \ldots, J$, $J \in \mathbb{N}$, we adapt wavelet amplitude regression (see e.g. [AGV09, Chapter 11]) for curvelet coefficients. That is, we estimate the critical value of s by a least squares approach. To this end, we compute the least squares solution in C and s of

$$|\Gamma_f(a_j, b_0, \theta_0)| = C \cdot a_j^{s+1}. \tag{4.10}$$

Taking logarithms in (4.10) leads to

$$\underbrace{\ln |\Gamma_f(a_j, b_k, \theta_l)|}_{=: y_j} = \ln C + (s+1) \underbrace{\ln a_j}_{=: x_j},$$

hence the least squares solution of (4.10) is given by

$$s + 1 = \frac{\sum_{j=0}^N x_j y_j - N \overline{x}\,\overline{y}}{\sum_{j=0}^N x_j^2 - N \overline{x}^2}, \qquad \text{and} \qquad C = \exp(\overline{y} - (s+1)\overline{x}),$$

where $\overline{x} = \frac{1}{N} \sum_{j=0}^N x_j$ and $\overline{y} = \frac{1}{N} \sum_{j=0}^N y_j$. Overall, an estimate for $s_f^*(b_k, \theta_l)$ is given by

$$s_f^*(b_k, \theta_l) \approx \frac{\sum_{j=0}^N x_j y_j - N \overline{x}\,\overline{y}}{\sum_{j=0}^N x_j^2 - N \overline{x}^2} - 1. \tag{4.11}$$

Having estimated the directional regularity function s_f^* we may estimate the wavefront set $\mathrm{WF}(f)$ by applying a suitable threshold to s_f^*.

Using the described curvelet amplitude regression, we encounter the issue that the estimates for $s_f^*(b, \theta)$ are not sharply localized around the actual singularities, cf. Figure 3.5. In order to get sharply localized edges we use a standard post-processing step called *non-maximum suppression*. This eliminates those points in the function $b \mapsto s_f^*(b, \theta)$ which are not local maxima into a direction θ. This technique is used also in classical edge detection methods such as the Canny method, see e.g. [Can86].

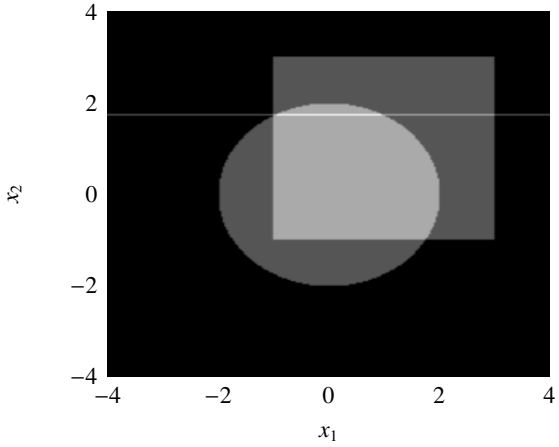

(a) A synthetic x-ray image f.

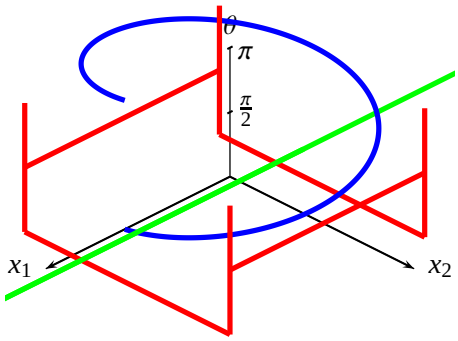

(b) Wavefront set $\mathrm{WF}(f)$ as subset of $\mathbb{R}^2 \times \mathbb{P}$.

Figure 4.1: Microlocal analysis of a synthetic x-ray type image consisting of three basic structures. We observe that each of the three edge structures of the image f (the circle, the line, and the square) corresponds to a connected subset of the wavefront set $\mathrm{WF}(f)$. Furthermore, these connected components do not intersect each other.

4.2 A new algorithm for separation of edges in x-ray images

We now exploit the connections between the wavefront set and the decay rates of the curvelet coefficients for the separation of overlaying edges in x-ray images. In this section, we motivate and develop our method, an appropriate edge model and a proof of functionality will be provided in the subsequent section.

Let us first state the problem. Assume we are given an *x-ray type image* f which is the linear combination of finitely many building blocks $f_1, ..., f_n \in \mathcal{D}'(\mathbb{R}^n)$, i.e.,

$$f = \sum_{j=1}^{N} f_j.$$

An example of a simple x-ray type image is depicted in Figure 4.1(a). That image consists of a circle $f_{\text{circle}} = \mathbb{1}_{B_2(0)}$, a square $f_{\text{square}} = \mathbb{1}_{[-1,3]^2}$, and an ideal line $f_{\text{line}} = \mathrm{dS}_{\{\sqrt{3}\}\times\mathbb{R}}$, where $\mathrm{dS}_{\{\sqrt{3}\}\times\mathbb{R}}$ denotes the distribution acting on test functions as integration along the line $\{\sqrt{3}\} \times \mathbb{R}$. Given the image

$$f = f_{\text{circle}} + f_{\text{line}} + f_{\text{square}},$$

our goal is to extract the edges of each single building block.

In order to see the difficulties of that task, let us assume that we have an edge detection method at hand which extracts the edges of the image f, which is the singular support of f in this example. The example is constructed such that the edges of the three structures intersect in the point $p = (1, \sqrt{3})$. In consequence, the intersection of their singular supports is

$$\operatorname{sing\,supp} f_{\text{circle}} \cap \operatorname{sing\,supp} f_{\text{line}} \cap \operatorname{sing\,supp} f_{\text{square}} = \{p\} \neq \emptyset.$$

Since each of the singular supports of f_{circle}, f_{line} and sing supp f_{square} is a connected set, the union

$$\text{sing supp } f = \text{sing supp } f_{\text{circle}} \cup \text{sing supp } f_{\text{line}} \cup \text{sing supp } f_{\text{square}}$$

is connected as well. Hence an analysis of the topology of sing supp f gives us just one single connected component, even though f consists of three different structures.

The idea of our method is to consider the wavefront set instead of the singular support, thus to lift the problem by one dimension to the phase space $\mathbb{R}^2 \times \mathbb{P}$. Inspecting the wavefront set of the image f, cf. Figure 4.1(b), we observe that the wavefront sets corresponding to each of the three building blocks are connected, but they do not intersect each other. This is because the intersecting image structures have different orientations at their intersection points. These observations give rise to the following method for the separation of edges in x-ray type images. We compute the wavefront set of the image, extract its connected components and project these connected components back to the image domain. The method is outlined in Algorithm 1.

Algorithm 1: Separation of edges in x-ray type images

input : X-ray type image $f = \sum_{i=1}^{N} f_i$.
output: Separate edges E_i corresponding to each of the edges of f_i, $i = 1, ..., N$.
begin

1. Compute the wavefront set $\widetilde{\text{WF}}(f) \subset \mathbb{R}^2 \times \mathbb{P}$ (e.g. by the decay rates of curvelet or shearlet coefficients);
2. Extract the connected components $W_1, \ldots, W_N$ of $\widetilde{\text{WF}}(f)$;
3. Project the connected components $W_i \subset \mathbb{R}^2 \times \mathbb{P}$ back to the image domain $\mathbb{R}^n$. The edges E_i correspond (up to reordering) to the projection to the first component of W_i, i.e., $E_i = \pi_1(W_i)$, $i = 1, \ldots, N$;

end

We now give a more detailed description of the implementation of the single steps of our algorithm. In the first step of Algorithm 1, we need to estimate the wavefront set. To this end, we estimate $s_f^*(x, \theta)$ and consider (x, θ) to belong the wavefront set, whenever $s_f^*(x, \theta)$ is smaller than a fixed threshold value $\tau \in \mathbb{R}$. As described in Section 3.5 and Subsection 4.1.3, we may use the curvelet transform to estimate the directional regularity function $s_f^*(x, \theta)$. In practice, a discrete estimate of $s_f^*(x, \theta)$ is given as a three dimensional array $s_{k_1,k_2,l}$, where k_1 and k_2 are discretizations of the spatial variable $x = (x_1, x_2)$ and l is the discretization of the directional variable θ. In our experiments, k_1 and k_2 are in $\{1, 2, ..., 512\}$ and l is in $\{0, \frac{\pi}{16}, ..., \frac{15\pi}{16}\}$. We mentioned in Subsection 4.1.3 that the estimates obtained from curvelet amplitude regression are not sharply localized. A common method to get sharply localized edges is non-maximum suppression. In this step, the value ∞ is assigned to each entry $s_{(k_1,k_2,l)}$ if (k_1, k_2) is not a local maximum of $s_{\bullet,\bullet,l}$ with respect to direction l. In the concrete implementation, we use the function `nonmaxsup` of [Kov08]. After the non-maximum suppression, we apply a threshold operation with respect to a threshold value $\tau \in \mathbb{R}$ to the array s. The arising binary array w, given by

$$w_{k_1,k_2,l} = \begin{cases} 1, & \text{if } s_{k_1,k_2,l} < \tau \\ 0, & \text{if } s_{k_1,k_2,l} \geq \tau. \end{cases} \quad \text{for each } k_1, k_2, \text{ and } l,$$

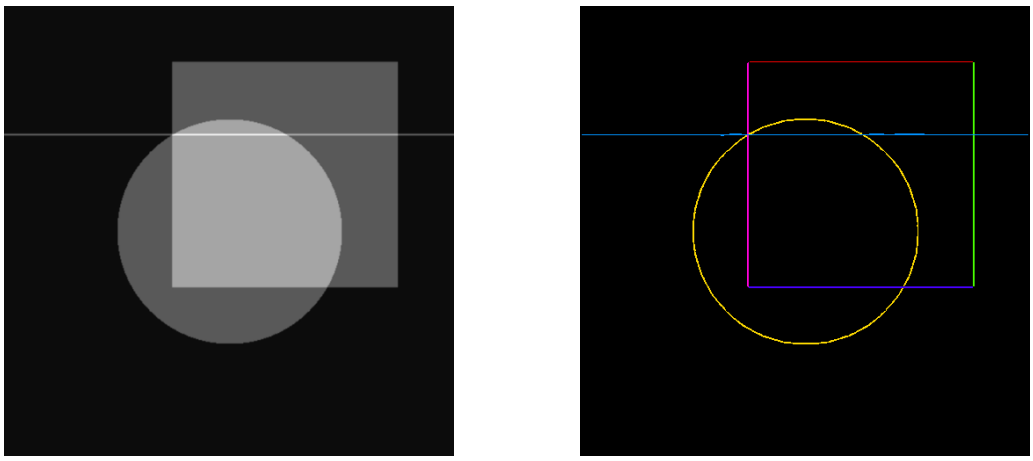

(a) (b)

Figure 4.2: (a) A synthetic x-ray image. (b) Result of the separation of edges algorithm, $\tau = 5.25$. The connected edges are marked in same color. We see that the crossing of the three structures is nicely resolved. However, we also see a shortcoming of the numerical approximation. The boundary of the square is not detected as a single connected edge, but consists of four components.

forms our estimate of the wavefront set. The threshold parameter τ has to be adjusted empirically. In the experiments, it turned out that choices between 3 and 8 give mostly satisfactory results.

In the second step of Algorithm 1, we compute the connected components of the wavefront set in $\mathbb{R}^2 \times \mathbb{P}$. This corresponds in the discrete setting to the extraction of the connected components of the binary array w, which we have computed in the first step. To this end, we use Matlab's connected component algorithm for binary arrays (`bwlabeln`) with the following necessary modification. The third component of w, which codes the orientations, needs to be considered as periodic, since it expresses the discretization of the real projective space. Thus we link the corresponding connected components in the third component at the boundaries of w.

As the last step, we assign a random color to each connected component of w and project these connected components back to the image domain $\{1, ..., 512\}^2$. As result we get an image where each connected edge is marked in a different color, see Figure 4.2(b) for instance.

Now let us turn to the numerical experiments. At first, we apply the separation of edges to the synthetic x-ray type image we considered at the beginning of the section. The results are depicted in Figure 4.2. We see in Figure 4.2(b) that our algorithm indeed separates all three intersecting edges. However, we also observe one shortcoming of our numerical estimate. The edge defined by the square is detected to consist of four single edges, which should in theory be detected as one single edge (compare Theorem 4.54 of the next section). This issue at the corners mainly seems to stem from two sources. First, the non-maximum suppression tends to suppress point-like local maxima. And second, the local regularity s_f^* is lower in the non-compass directions than in the compass directions (compare Theorem 4.37 of the next section). Thus, the non-compass directions of the corner points are more likely to fall beyond the threshold τ, and hence, are more likely to be estimate to lie outside the wavefront set.

Next we look at the x-ray image of a human shoulder, see Figure 4.3(a). In that image, we find many crossing edges arising from the boundaries of the shoulder and the thorax bones. In most

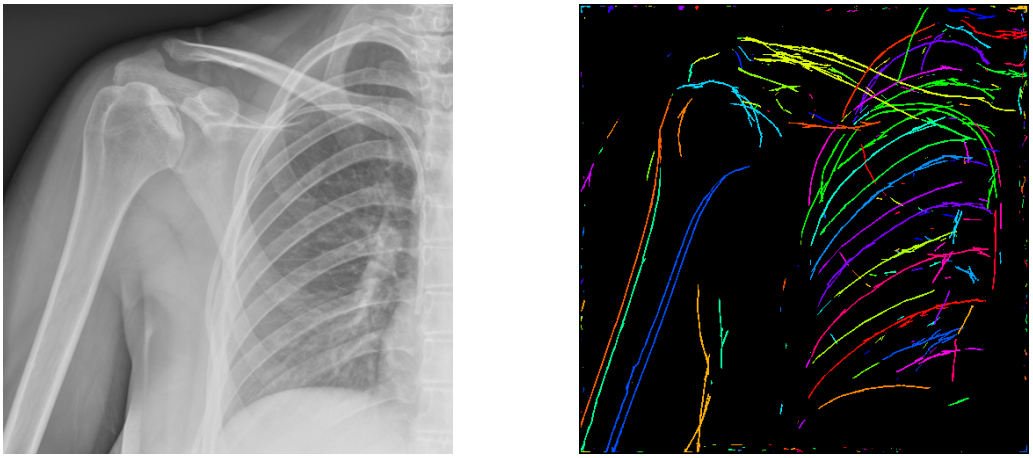

(a) (b)

Figure 4.3: (a) A typical x-ray image, taken from [Rad12]. (b) Separation of edges algorithm applied to the x-ray image, $\tau = 6.75$. Connected edges are marked in same color. Most crossing structures, for example the shoulder bones and the ribs, are separated from each other. As the number of edges exceeds the number of distinguishable colors, some edges appear to have the same color, even though they are not connected in the image domain.

cases, the bones intersect non-tangetially, so the separation of edges algorithm is able to resolve the crossings edges. A particular example are the intersections of the shoulder and the rib bones; see Figure 4.3(b).

4.3 Edge model and microlocal analysis of the separation of edges algorithm

Our next goal is the mathematical analysis of our algorithm for the separation of edges in x-ray images. To this end, we require a suitable mathematical model for edges in x-ray images, which we will develop in the following. With that edge model we will be able to derive conditions under which our algorithm works properly.

Edges are classically modeled as those points of an image f where the modulus of the gradient $|\nabla f|$ attains a local maximum in the gradient direction. The direction of an edge point is then considered to be the gradient direction $\frac{\nabla f}{|\nabla f|}$. This classical edge model is particularly easy to interpret and has proven its plausibility in many applications, see e.g. [Can86]. However, it has two major drawbacks. The first one is that it requires the image to be differentiable. This constraint conflicts with the model of "ideal" edges, for example an ideal step edge $f = \mathbb{1}_{[0,\infty)\times\mathbb{R}}$. The second disadvantage of the classical edge model concerns the resolution of multiple edge directions. The gradient is in particular a function on the image domain, thus it assigns a unique direction to every spatial point. Thus if a point possesses multiple edge directions, such as at corner points or at the intersection of edges in x-ray images, then the gradient returns only an averaged direction. But this average direction only in rare cases coincides with one of the actually expected edge directions. The first shortcoming can be resolved relatively easy by a convolution

of the image with a smooth function, at the cost of a some uncertainty with respect to edge locations. The exact resolution of multiple directions, on the other hand, is much harder to achieve.

In this section, a novel edge model is presented, which resolves both of the mentioned issues. It applies to non-differentiable and even to distributional images. Even more important, it allows for the resolution of arbitrarily many orientations at each spatial point. We motivate our edge model as follows. First consider a planar geometric figure $Y \subset \mathbb{R}^2$ such that its (topological) boundary $E := \partial_{\mathbb{R}^2} Y$ is a smooth manifold. The natural edge of f is the boundary E, the natural orientations of the edge points are the normal vectors to the boundary E. Thus the edge points and their orientations can be identified with the normal bundle of E, i.e.,

$$\bigcup_{x \in E} \{x\} \times (\mathrm{N}_x E \setminus \{0\}) =: \mathrm{N}\, E \setminus \{0\},$$

where $N_x E \subset \mathbb{R}^2$ denotes the normal space of E at x. Now assume that the figure Y is given implicitly as the function $f = \mathbb{1}_Y$, that is, the figure is coded in an image $f : \mathbb{R}^2 \to \mathbb{R}$. It is easy to see that the edge set E coincides with the singular support of f. It is a classical result of microlocal analysis [Hö03, Ch. VIII] that the normal bundle of the boundary of Y is equal to the wavefront set of the indicator function $\mathbb{1}_Y$, that is,

$$\mathrm{WF}(\mathbb{1}_Y) = \mathrm{N}\, E \setminus \{0\}. \tag{4.12}$$

Our edge model mainly bases on this correspondence between geometric objects and wavefront sets of the associated function. We will say that a distribution defines an edge if its wavefront set has the structure of the normal bundle of a manifold, cf. Definition 4.41.

In our example, we have assumed that the boundary of Y is a smooth manifold. In order to be able to treat corner points, we extend the model to manifolds with corners. Note that in this case, the equality in (4.12) is not any more valid as it stands. However, we establish in Theorem 4.39 an equation analogous to (4.12) for manifolds with corners, which employs a geometrically motivated definition of normal space.

4.3.1 Submanifolds with corners as geometric edge models

We now introduce submanifolds with corners in $\mathbb{R}^n$, which will serve as our geometric edge model. We loosely follow the notations and definitions of [Joy09], [Kö04] and [Lee03]. We start with recalling the definition of a submanifold in $\mathbb{R}^n$, following [Kö04, p. 116].

Definition 4.19. Let $l \in \mathbb{N} \cup \{\infty\}$. A non-empty subset M of $\mathbb{R}^n$ is called *d-dimensional C^l-submanifold* if for every point $p \in M$ there is an open neighborhood $U \subset \mathbb{R}^n$ and a C^l-diffeomorphism $\Phi : U \to V$ onto an open subset V of $\mathbb{R}^n$ such that

$$\Phi(M \cap U) = V \cap (\mathbb{R}^d \times \{0\}^{n-d}).$$

We call the diffeomorphism Φ *chart* and $M \cap U$ its *chart domain.* A set of charts $\{\Phi_i\}_{i \in I}$ with chart domains $M \cap U_i$ is called *atlas,* if $\{U_i\}_{i \in I}$ forms a covering of M. ⌟

In the following, the index $l \in \mathbb{N} \cup \{\infty\}$ denotes the order of differentiability of the manifold and the integer d, where $0 \leq d \leq n$, denotes the dimension of the manifold.

Definition 4.20. Let M be a subset of $\mathbb{R}^n$. A vector $v \in \mathbb{R}^n$ is called *geometric tangent vector* to M at $p \in M$ if there is a differentiable curve $\alpha : (-\epsilon, \epsilon) \to M$, $\epsilon > 0$, such that $\alpha(0) = p$ and $\alpha'(0) = v$. We call the cone of all geometric tangent vectors to M at p, defined by

$$\mathrm{GT}_p M \coloneqq \{v \in \mathbb{R}^n : v \text{ is a tangent vector to } M \text{ at } p\},$$

the *geometric tangent cone.* If it is a vector space, we call $\mathrm{GT}_p M$ *geometric tangent space of* M *at* p. ⌟

We comment at the end of the subsection on the differences of the geometric tangent vectors to the tangent vectors which are most frequently used in modern differential geometry.

Since the submanifold M is embedded in $\mathbb{R}^n$, we can express the tangent space explicitly by the differential of the charts, cf. [Kö04, p. 120].

Lemma 4.21. *Let $M \subset \mathbb{R}^n$ be a d-dimensional C^l-submanifold, and Φ a chart for $p \in M$. Then the geometric tangent space to M at p is an d-dimensional vector space given by*

$$\mathrm{GT}_p M = (\mathrm{d}\Phi_p)^{-1}(\mathbb{R}^d \times \{0\}^{n-d}).$$ ⌟

For subsets of $\mathbb{R}^n$ we define the geometric normal cone and geometric normal space as follows.

Definition 4.22. Let M be a arbitrary subset of $\mathbb{R}^n$. A vector $v \in \mathbb{R}^n$ is called *geometric normal vector* to M at $p \in M$ if v is orthogonal to all geometric tangent vectors at p, that is, if $v \perp u$ for every $u \in \mathrm{GT}_p M$. We call the space of all geometric normal vectors to M at p, defined by

$$\mathrm{GN}_p M \coloneqq (\mathrm{GT}_p M)^{\perp} = \left\{\xi \in \mathbb{R}^n : \langle \xi, \zeta \rangle = 0 \text{ for every } \zeta \in \mathrm{GT}_p M\right\},$$

the *geometric normal space.* ⌟

The geometric tangent bundle and the geometric normal bundle are defined as follows.

Definition 4.23. Let M be a subset of $\mathbb{R}^n$. We define the *geometric tangent bundle* of M, denoted by $\mathrm{GT}\, M$ to be the disjoint union of the tangent cones at all points of M, that is,

$$\mathrm{GT}\, M = \coprod_{p \in M} \mathrm{GT}_p M = \bigcup_{p \in M} \{p\} \times \mathrm{GT}_p M.$$

Analogously, the *geometric normal bundle* is defined by

$$\mathrm{GN}\, M = \coprod_{p \in M} \mathrm{GN}_p M = \bigcup_{p \in M} \{p\} \times \mathrm{GN}_p M.$$ ⌟

Submanifolds with corners are defined analogously to classical submanifolds. The only difference is that the charts map on quadrants instead of subspaces. In the following, we use the notation

$$Q_d^n \coloneqq [0, \infty)^d \times \{0\}^{n-d}$$

for the positive d-dimensional quadrant in $\mathbb{R}^n$.

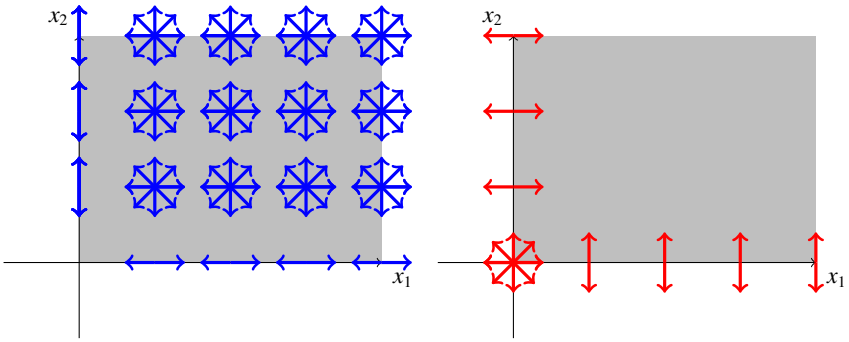

Figure 4.4: Geometric tangent (blue) and normal vectors (red) of the submanifold with corners $Q_2^2 = [0, \infty)^2$.

Definition 4.24. Let $l \in \mathbb{N} \cup \{\infty\}$. A non-empty subset M of $\mathbb{R}^n$ is called *d-dimensional C^l-submanifold with corners* of $\mathbb{R}^n$ if for every point $p \in M$ there is an open neighborhood $U \subset \mathbb{R}^n$ and a C^l-diffeomorphism $\Phi : U \to V$ onto an open subset V of $\mathbb{R}^n$ such that

$$\Phi(M \cap U) = V \cap Q_d^n. \tag{4.13}$$

We call the diffeomorphism Φ *chart with corners* and U its *chart domain.* A set of charts with corners $\{\Phi_i\}_{i \in I}$ with chart domains U_i is called *atlas with corners,* if $\{U_i\}_{i \in I}$ forms a covering of M. ⌟

We refer to Figure 4.4 for an illustration of a simple manifold with corners and its geometric tangent and normal bundles. We call a d-dimensional C^l-submanifold (with corners) also shortly *manifold (with corners).* Note that each manifold is in particular a manifold with corners but not the other way round. Let us illustrate this in an example.

Example 4.25.
1. The open d-dimensional cube $K = (0, 1)^d \times \{0\}^{n-d}$ in $\mathbb{R}^n$ is a d-dimensional C^∞-manifold.
2. The closed d-dimensional cube $\overline{K} = [0, 1]^d \times \{0\}^{n-d}$ in $\mathbb{R}^n$ is a d-dimensional C^∞-manifold with corners, but not a manifold. ⌟

Remark 4.26. Definition 4.24 follows the classical constructions of manifolds with corners using the quadrants of $\mathbb{R}^n$ as model spaces, see e.g. [Lee03, Joy09]. We mention that these model spaces cannot model polytopes in $\mathbb{R}^n$, $n \geq 3$, whose vertices have more than n edges. For example, a pyramid whose basis is a polygon of 4 or more vertices is not a submanifold with corners of $\mathbb{R}^3$. Note that this issue does not occur in two dimensions, thus such restrictions do not apply for the modeling of two dimensional images. ⌟

In order to distinguish different types of corners, we next define the rank of a point on the manifold. This allows in particular for the discrimination between corner and non-corner points.

Definition 4.27. Let M be d-dimensional C^l-submanifold with corners of $\mathbb{R}^n$ and Φ a chart for $p \in M$. We define the *rank of p,* denoted by $\operatorname{rank}_M p$, by

$$\operatorname{rank}_M p = \#\operatorname{supp} \Phi(p).$$

We say that p is a *non-corner point* if $\operatorname{rank}_M p = d$ and a *corner point* if $\operatorname{rank}_M p < d$. ⌟

In Definition 4.24, a chart Φ may map a point $p \in M$ to a rather arbitrary point in $Q_d^n = [0,\infty)^d \times \{0\}^{n-d}$. In order to simplify subsequent definitions and proofs, a distinguished type of charts with corners is now defined, called canonical charts. Such charts map points on the manifold to a certain subset of points in Q_d^n.

Definition 4.28. Let $M \subset \mathbb{R}^n$ be a d-dimensional C^l-submanifold with corners of $\mathbb{R}^n$ and Φ a chart with corners for $p \in M$. Further let $r = \operatorname{rank}_M p$. We say that Φ is a *canonical chart with corners* if the non-vanishing components of $q = \Phi(p)$ are exactly its first r components, that is, if

$$\Phi(p) = (q_1, \ldots, q_r, 0, \ldots, 0)$$

and $q_1, \ldots, q_r \neq 0$. ⌟

We show that every manifold with corners possesses a canonical chart with corners.

Lemma 4.29. *Let $M \subset \mathbb{R}^n$ be a d-dimensional C^l-submanifold with corners of $\mathbb{R}^n$. For every $p \in M$ there is a canonical C^l-chart with corners.* ⌟

Proof. Let $p \in M$, Φ be a chart with corners for p and let $r = \operatorname{rank}_M p$. We construct a canonical chart Ψ for p. Denote $i_1, \ldots, i_r$ the non-vanishing indices of $q = \Phi(p)$, that is, $q_{i_1}, \ldots, q_{i_r} \neq 0$. Let $\sigma : \{1, \ldots, n\} \to \{1, \ldots, n\}$ be a permutation and define the action of σ to a vector $x \in \mathbb{R}^n$, denoted by σx, by

$$(\sigma x)_i = x_{\sigma(i)}$$

for every $i \in \{1, \ldots, n\}$. We can choose σ such that it satisfies $\sigma(k) = i_k$ for $k = 1, \ldots, r$ and $\sigma(k') = k'$ for $k' = d+1, \ldots, n$. We set $\Psi = \sigma^{-1} \circ \Phi$. Ψ is an l-times differentiable map and $\Psi(U) \subset [0,\infty)^d \times \{0\}^{n-d}$. By construction, Ψ satisfies $\Psi(p_k) \neq 0$ for $k = 1, \ldots, r$ and $\Psi(p_{k''}) = 0$ for $k'' = r+1, \ldots, n$. Hence, Ψ is a canonical chart with corners for p. ∎

Canonical charts allow for a convenient representation of the geometric tangent space of a manifold with corners by the differential of the chart.

Proposition 4.30. *Let $M \subset \mathbb{R}^n$ be a d-dimensional C^l-submanifold with corners, and let Φ be a canonical chart with corners for $p \in M$. Denote $r = \operatorname{rank}_M p$. Then the geometric tangent space to M at p is an r-dimensional vector space given by*

$$\mathrm{GT}_p M = (\mathrm{d}\Phi_p)^{-1}(\mathbb{R}^r \times \{0\}^{n-r}).$$

and the geometric normal space to M at p is an r-dimensional vector space given by

$$\mathrm{GN}_p M = \mathrm{d}\Phi_p^T(\{0\}^r \times \mathbb{R}^{n-r}).$$ ⌟

Proof. The proof is analogous to the case of manifolds without corners in [Kö04, p. 120]. We first look at the geometric tangent space of the prototype manifold $Q_d^n = [0,\infty)^d \times \{0\}^{n-d}$. For $q = (q_1, \ldots, q_r, 0, \ldots, 0)$, where $q_1, \ldots, q_r \neq 0$ and $r \leq d$, we observe that

$$\mathrm{GT}_q Q = \mathbb{R}^r \times \{0\}^{n-r}. \tag{4.14}$$

Now let $U \subset \mathbb{R}^n$ be the chart domain of Φ. The diffeomorphism Φ maps any differentiable curve $\alpha : (-\epsilon, \epsilon) \to M \cap U$ to a differentiable curve $\overline{\alpha} \coloneqq \Phi \circ \alpha$ on the quadrant $\Phi(U) \cap Q_d^n$. For any such curve $\beta : (-\epsilon, \epsilon) \to \Phi(U) \cap Q_d^n$ on the quadrant there is a curve $\overline{\beta}$ such that $\Phi \circ \overline{\beta} = \beta$. So there is a one-to-one correspondence between the set differentiable curves $\alpha : (-\epsilon, \epsilon) \to M \cap U$ with $\alpha(0) = p$. By the chain rule, the tangent vectors of such corresponding curves α and $\overline{\alpha}$ are related by

$$\overline{\alpha}'(0) = (\Phi \circ \alpha)'(0) = \mathrm{d}\Phi_p(\alpha'(0)),$$

and, inversely, $\alpha'(0) = (\mathrm{d}\Phi_p)^{-1}\overline{\alpha}'(0)$. So it follows

$$\mathrm{GT}_p M = (\mathrm{d}\Phi_p)^{-1}\mathrm{GT}_{\Phi(p)} Q.$$

Since Φ is a canonical chart, it holds that exactly the first r components of $\Phi(p)$ do not vanish, so it follows by (4.14) that

$$\mathrm{GT}_p M = (\mathrm{d}\Phi_p)^{-1}(\mathrm{GT}_{\Phi(p)} Q) = (\mathrm{d}\Phi_p)^{-1}(\mathbb{R}^r \times \{0\}^{n-r}),$$

which is the first claim. The computation

$$\begin{aligned}
\mathrm{GN}_p M &= \left\{\xi \in \mathbb{R}^n : \ \langle \xi, \zeta \rangle = 0 \text{ for every } \zeta \in \mathrm{GT}_p M\right\} \\
&= \left\{\xi \in \mathbb{R}^n : \ \langle \xi, \mathrm{d}\Phi_p^{-1}\eta \rangle = 0 \text{ for every } \eta \in \mathbb{R}^r \times \{0\}^{n-r}\right\} \\
&= \left\{\xi \in \mathbb{R}^n : \ (\mathrm{d}\Phi_p^{-1})^T \xi \in \{0\}^r \times \mathbb{R}^{n-r}\right\} \\
&= \mathrm{d}\Phi_p^T(\{0\}^r \times \mathbb{R}^{n-r})
\end{aligned}$$

proves the second assertion. ∎

As a direct consequence, we can compute the geometric tangent and normal spaces for arbitrary points on the quadrant Q_d^n, thus for $p \in Q_d^n$ the geometric tangent space is given by

$$\mathrm{GT}_p Q_d^n = \operatorname{span}\{\mathbf{e}_i : i \in \operatorname{supp} p\} \tag{4.15}$$

and the geometric normal space by

$$\mathrm{GN}_p Q_d^n = \operatorname{span}\{\mathbf{e}_i : i \notin \operatorname{supp} p\}. \tag{4.16}$$

The geometric tangent and normal bundles of Q_2^2 are depicted schematically in Figure 4.4. Another immediate consequence of Proposition 4.30 is the following statement.

Corollary 4.31. *Let $M \subset \mathbb{R}^n$ be a d-dimensional C^l-submanifold with corners. For the dimensions of the geometric tangent and normal spaces it holds that*

$$\dim(\mathrm{GT}_p M) = \operatorname{rank}_M p \quad \textit{and} \quad \dim(\mathrm{GN}_p M) = n - \operatorname{rank}_M p. \qquad ⌟$$

We summarize the most important differences between classical manifolds and manifolds with corners in Table 4.1.

	Classical submanifolds	Submanifolds with corners
Charts Φ	mapping to $\mathbb{R}^d \times \{0\}^{n-d}$	mapping to $Q_d^n = [0,\infty)^d \times \{0\}^{n-d}$
Classical tangent space $\mathrm{T}_p M$	$\mathrm{d}\Phi_p^{-1}(\mathbb{R}^d \times \{0\}^{n-d})$	$\mathrm{d}\Phi_p^{-1}(\mathbb{R}^d \times \{0\}^{n-d})$
Geometric tangent space $\mathrm{GT}_p M$	$\mathrm{d}\Phi_p^{-1}(\mathbb{R}^d \times \{0\}^{n-d})$	$\mathrm{d}\Phi_p^{-1}(\mathbb{R}^{\operatorname{rank}_M p} \times \{0\}^{n-\operatorname{rank}_M p})$

Table 4.1: Comparison between classical manifolds and manifolds with corners.

Remark 4.32. Now we can explain why we have chosen the distinct notation $\mathrm{GT}_p M$ for the geometric tangent space, instead of the classical notation $\mathrm{T}_p M$. In modern differential geometry, the tangent space is defined by an algebraic property, abstract from the geometric interpretation. The (algebraic) tangent space $\mathrm{T}_p M$ of M at a point p is defined as the space of all linear mappings $\widetilde{v} : C^l(M) \to \mathbb{R}$, called *derivations,* which satisfy the product rule

$$v(fg) = f(p)v(g) + g(p)v(f)$$

for all $f, g \in C^l(M)$. For classical submanifolds *without* corners, the algebraic and the geometric definitions lead to the same spaces, that is, there is an isomorphism between $\mathrm{T}_p M$ and $\mathrm{GT}_p M$, (see [Jä93, Chapter 2]). For manifolds with corners, in contrast, the algebraic and the geometric definitions of the tangent space are not equivalent. The algebraic tangent space of a d-dimensional submanifold of $\mathbb{R}^n$ leads to the expression given in Lemma 4.21, that is,

$$\mathrm{T}_p M = (\mathrm{d}\Phi_p)^{-1}(\mathbb{R}^d \times \{0\}^{n-d}).$$

In particular, the dimension of the algebraic tangent $\mathrm{T}_p M$ space coincides with the dimension d of the manifold, no matter if $p \in M$ is a corner point or not. On the other hand, the dimension of the geometric tangent space $\mathrm{GT}_p M$ depends on the locus of the point p. Indeed, from Corollary 4.31 we see that the rank of a point on the manifold determines the dimension of the geometric tangent space. For example, the algebraic and the geometric tangent space do not coincide for the manifold with corners $M = [0,\infty) \times \mathbb{R}$ at $p = 0$; that is,

$$\mathrm{GT}_0 M = \{0\} \times \mathbb{R} \subsetneq \mathbb{R}^2 = \mathrm{T}_0 M.$$

We also note that, since the dimensions of the tangent spaces are not constant, the geometric tangent bundle does not necessarily fulfill the so-called local triviality condition. Thus the geometric tangent bundle of a manifold with corners is not a fiber bundle in general. ⌟

Let us now turn to the geometric edge model. In the following, we write $\partial_{\mathbb{R}^n} M$ for the (topological) boundary of a submanifold with corners M of $\mathbb{R}^n$, that is, $p \in \partial_{\mathbb{R}^n} M$ if and only if for every neighborhood U of p it holds that $U \cap M \neq \emptyset$ and $U \cap (\mathbb{R}^n \setminus M) \neq \emptyset$. The following definition fixes our geometric model for edges based on manifold with corners.

Definition 4.33. Let M be a C^l-submanifold with corners of $\mathbb{R}^n$. We call M an *C^l-edge defining manifold* if M is (topologically) closed in $\mathbb{R}^n$ and its boundary $\partial_{\mathbb{R}^n} M$ is connected. We call the boundary $\partial_{\mathbb{R}^n} M$ a *C^l-edge.* ⌟

Definition 4.33 may be interpreted as follows. The locus of an edge is considered to be the topological boundary of a submanifold with corners. (We notice that $\partial_{\mathbb{R}^n} M$ is in general not a manifold with corners.) The structure of an edge is determined by the structure of its defining manifold. In particular, the orientations indicated by the (geometric) normal vectors of the manifold determine the edge orientations. The connectedness of the boundary assures that each edge defining manifold models exactly one connected edge.

4.3.2 A microlocal edge model

We have just clarified how we understand the geometry of edges in $\mathbb{R}^n$. Since images are not given as geometric objects, but as functions or distributions expressing light intensities, we have to formulate an analytic model which fits to the geometric model of Definition 4.33. To this end, we consider initially the volume forms dS_M, where M is an edge defining manifold. The volume form dS_M can be considered as distribution which acts on test functions by integration along M, that is,

$$\langle \mathrm{dS}_M, \phi \rangle = \int_M \phi \, \mathrm{dS}, \qquad \text{for all } \phi \in \mathcal{D}(\mathbb{R}^n).$$

We will based our analytic edge model (Definition 4.41) on the equality of the geometric normal bundle of M and the wavefront set of dS_M. To establish that equality we need some preliminary results.

In the following we write in a slight abuse of notations

$$\mathrm{GN}\, M \setminus \{0\} \coloneqq \bigcup_{p \in M} \{p\} \times (\mathrm{GN}_p M \setminus \{0\})$$

for the geometric normal bundle with the zero section removed. To make computations in the following easier, we introduce the class of separable bump functions.

Definition 4.34. We say that $\phi \in \mathcal{D}(\Omega)$ is a *separable bump function* centered around x_0 in $\mathbb{R}^n$ if there are functions $\psi_1, \ldots, \psi_N \in \mathcal{D}(\mathbb{R})$, satisfying $\psi_j \geq 0$ and $\psi_j = 1$ in a neighborhood of x_0, such that

$$\phi(x) = \prod_{j=1}^{N} \psi_j(x_j).$$

We denote the class of separable bump functions centered around x_0 by $\mathcal{D}_{\mathrm{sep}}(\Omega; x_0)$. ⌟

It follows from the next two lemmas that it is sufficient to consider the separable bump functions for the computation of the localized frequency set.

Lemma 4.35. *Let $f \in \mathcal{D}'(\mathbb{R}^n)$ and $y \in \mathbb{R}^n$. Let $\phi \in \mathcal{D}(\mathbb{R}^n)$ such that $\phi(y) \neq 0$. Then there exist an open neighborhood U of y such that for every $\psi \in \mathcal{D}(U)$*

$$\Sigma^s(\psi f) \subseteq \Sigma^s(\phi f). \qquad ⌟$$

Proof. Let $\epsilon > 0$. As $\phi(y) \neq 0$ there exist an open neighborhood $U \subset \operatorname{supp} \phi$ of y such that $|\phi(x)| > \epsilon$ for every $x \in U$. Let $\psi \in \mathcal{D}(U)$ and define

$$g(x) \coloneqq \begin{cases} \frac{\psi(x)}{\phi(x)}, & \text{if } \phi(x) \neq 0, \\ 0, & \text{else.} \end{cases}$$

As $g \in C^\infty$ and $\phi f \in \mathcal{E}'$ we may apply Corollary 4.13 to conclude

$$\Sigma^s(\psi f) = \Sigma^s(g\phi f) \subset \Sigma^s(\phi f).$$

■

Lemma 4.36. *Let $f \in \mathcal{D}'(\Omega)$ and $x \in \Omega$. If $\phi \in \mathcal{D}(\Omega)$ such that $\phi(x) \neq 0$, then there exist $\psi \in \mathcal{D}_{\text{sep}}(\Omega)$*

$$\Sigma^s(\psi f) \subseteq \Sigma^s(\phi f).$$

In particular,

$$\Sigma^s_x(f) = \bigcap_{\phi \in \mathcal{D}_{\text{sep}}(\Omega; x)} \Sigma^s(\phi f).$$

⌟

Proof. By Lemma 4.35 there exist a neighborhood $U \subset \operatorname{supp}\phi$ of y such that for every $\psi \in \mathcal{D}(U)$

$$\Sigma^s(\psi f) \subseteq \Sigma^s(\phi f).$$

Let $l > 0$ so small such that $x + [-l, l]^n \subset U$. For every $j = 1, \dots, n$ choose $\psi_j \in \mathcal{D}(\mathbb{R})$ such that $\operatorname{supp}\psi_j \subset x_j + [-l, l]$, $\psi_j(y) \geq 0$ for all $y \in \mathbb{R}$ and $\psi_j(y_j) = 1$ for all y_j in a neighborhood of x_j. Then

$$\psi(x) \coloneqq \prod_{j=1}^n \psi_j(x_j)$$

is in $\mathcal{D}_{\text{sep}}(U; x)$ and by Lemma 4.35 holds that $\Sigma^s(\psi f) \subseteq \Sigma^s(\phi f)$. The second claim is a direct consequence. ■

Now we are able to compute the frequency sets of the distributions $\mathrm{dS}_{Q^n_d}$.

Theorem 4.37. *Let $0 \leq k \leq d$ and $p \in Q^n_d$ such that $p = (p_1, \dots, p_k, 0, \dots, 0)$, where $p_1, \dots, p_k \neq 0$. Then $\xi \in \mathbb{R}^n \setminus \{0\}$ belongs to the H^s-frequency set $\Sigma^s_p(\mathrm{dS}_{Q^n_d})$ of the distribution $\mathrm{dS}_{Q^n_d}$ if and only if*

$$\xi_1 = \dots = \xi_k = 0 \quad \text{and} \quad \#\{l : k+1 \leq l \leq d : \xi_l \neq 0\} \leq 2s + n - d.$$

In particular,

$$\Sigma_p(\mathrm{dS}_{Q^n_d}) = \mathrm{GN}_p Q^n_d \setminus \{0\}.$$

⌟

Proof. Let $\phi \in \mathcal{D}_{\text{sep}}(\mathbb{R}^n; p)$ be a separable bump function supported in a sufficiently small ball around p. Since ϕ is a separable bump function there are $\psi_j \in \mathcal{D}(\mathbb{R})$ such that

$$\phi(x) = \prod_{j=1}^n \psi_j(x)$$

where $\psi_j \geq 0$ and $\psi_j(y_j) = 1$ for all y_j in a neighborhood of p_j, for all $j = 1, ..., n$. We have to check for which $s \in \mathbb{R}$ there is an open cone V such that the integral

$$\int_V |\widehat{\phi f}(\eta)|^2 \langle \eta \rangle^{2s} \, \mathrm{d}\eta < \infty. \tag{4.17}$$

Since $\widehat{\phi f}$ is continous, $|\widehat{\phi f}(\eta)|^2\langle\eta\rangle^{2s}$ is integrable on every ball of radius $R > 0$ around the origin so it it sufficient to check for which s the integral

$$\int_{V\setminus B_R(0)} |\widehat{\phi f}(\eta)|^2\langle\eta\rangle^{2s}\,\mathrm{d}\eta \tag{4.18}$$

exists, where R may be chosen arbitrarily large. To this end, we first compute

$$\begin{aligned}
\widehat{\phi f}(\eta) &= \int_{Q_d^n} \phi(x) e^{-2\pi i\, x\cdot\eta}\mathrm{dS}(x) = \int_{Q_d^n} \prod_{j=1}^{n} \psi_j(x_j) e^{-2\pi i\, x\cdot\eta}\mathrm{dS}(x) \\
&= \int_{-\infty}^{\infty}\cdots\int_{-\infty}^{\infty}\int_{0}^{\infty}\cdots\int_{0}^{\infty} \prod_{j=1}^{d} \psi_j(x_j) e^{-2\pi i\, x_j\cdot\eta_j}\,\mathrm{d}x_1\cdots\mathrm{d}x_k\,\mathrm{d}x_{k+1}\cdots\mathrm{d}x_d \prod_{j=d+1}^{n} \underbrace{\psi_j(p_j)}_{=1} \\
&= \prod_{j=1}^{k}\int_{-\infty}^{\infty} \psi_j(x_j) e^{-2\pi i\, x_j\cdot\eta_j}\,\mathrm{d}x_j \prod_{j=k+1}^{d}\int_{0}^{\infty} \psi_j(x_j) e^{-2\pi i\, x_j\cdot\eta_j}\,\mathrm{d}x_j.
\end{aligned} \tag{4.19}$$

Now we write $\xi = (\xi', \xi'', \xi''') \in \mathbb{R}^k \times \mathbb{R}^{d-k} \times \mathbb{R}^{n-d}$ and distinguish the two cases $\xi' \neq 0$ and $\xi' = 0$.

We start with the case $\xi' \neq 0$. In this case, there exists l with $1 \leq l \leq k$ such that $\xi_l \neq 0$. Then we find a conic neighborhood V of ξ such that $\eta_l \neq 0$ for all $\eta \in V$. Since all ψ_j are compactly supported and continuous, g is bounded for each $\eta \in V$ by

$$|\widehat{\phi f}(\eta)| \leq \left|\widehat{\psi_l}(\eta_l)\right| \cdot \prod_{\substack{j=1\\ j\neq l}}^{k}\int_{-\infty}^{\infty}\left|\psi_j(x_j)\right|\,\mathrm{d}\eta_j \cdot \prod_{j=k+1}^{d}\int_{0}^{\infty}\left|\psi_j(x_j)\right|\,\mathrm{d}x_j \leq \left|\widehat{\psi_l}(\eta_l)\right| \cdot \prod_{\substack{j=1\\ j\neq l}}^{d}\left\|\psi_j\right\|_1.$$

As ψ_l is smooth, $\widehat{\psi_l}$ is of rapid decay. So $\widehat{\phi f}$ is of rapid decay on the cone V. In particular, (4.18) exists for all $s \in \mathbb{R}$. In consequence, $\xi \notin \Sigma_p^s(Q_d^n)$ for every $s \in \mathbb{R}$.

Now we come to the second case $\xi' = 0$, where ξ is of the form $(0, \xi'', \xi''')$. We denote the number of non-zero elements of ξ'' by m, that is,

$$m := \#\mathrm{supp}\,\xi''.$$

Without loss of generality, we may assume that $\xi_{k+1}, \ldots, \xi_{d-m} = 0$ and $\xi_{d-m+1}, ..., \xi_d \neq 0$. The other cases follow from a permutation of the indices. Furthermore, we may assume that $|\xi| = 1$. So ξ reads as

$$\xi = (0, ..., 0, \xi_{d-m+1}, ..., \xi_n) \quad \text{with } |\xi| = 1.$$

We aim for estimating $|\widehat{\phi f}(\eta)|^2\langle\eta\rangle^{2s}$ and we begin with an estimate for the factor $\langle\eta\rangle^{2s}$. We set

$$\alpha_0 = \frac{1}{2}\min_{i=d-m+1,\ldots,d}|\xi_i|$$

and define a truncated cone around ξ of aperture $0 < \alpha < \alpha_0$ by

$$V_{\alpha,R} = \{\eta \in \mathbb{R}^n : \left|\xi - \frac{\eta}{|\eta|}\right| < \alpha \text{ and } |\eta| > R\}.$$

The cone was chosen so narrow that the maximal entry of each vector $\eta \in V_{\alpha,R}$ is within the last $d-m+1$ components, that is,

$$|\eta|_\infty = \max_{i=1,\dots,n} |\eta_i| = \max_{i=d-m+1,\dots,d} |\eta_i| = |(\eta_{d-m+1},\dots,\eta_n)|_\infty.$$

By the equivalence of the norms in $\mathbb{R}^n$, there are constants $C, C' > 0$ such that

$$|(\eta_{d-m+1},\dots,\eta_n)| \le |\eta| \le C \cdot |\eta|_\infty = C \cdot |(\eta_{d-m+1},\dots,\eta_n)|_\infty \le C' \cdot |(\eta_{d-m+1},\dots,\eta_n)|$$

Thus, for every $s \in \mathbb{R}$, there are $R_s > 0$ and $C_s, C_s' > 0$ such that

$$C_s \cdot (1 + |(\eta_{d-m+1},\dots,\eta_n)|^2)^s \le (1+|\eta|^2)^s \le C_s' \cdot (1 + |(\eta_{d-m+1},\dots,\eta_n)|^2)^s \tag{4.20}$$

for all η in the truncated cone V_{α,R_s}.

We next estimate $|\widehat{\phi f}(\eta)|$ by estimating the factors of (4.19) for the indices $j = d-m+1,\dots d$. Integrating by parts gives for all $j = d-m+1,\dots d$ that

$$\begin{aligned}\int_0^\infty \psi_j(x_j) e^{-2\pi i\, x_j\cdot\eta_j}\,\mathrm{d}x_j &= \left[\psi_j(x_j)\frac{1}{-2\pi i\,\eta_j} e^{-2\pi i\, x_j\cdot\eta_j}\right]_0^\infty - \frac{1}{-2\pi i\,\eta_j}\int_0^\infty \psi_j'(x_j) e^{-2\pi i\, x_j\cdot\eta_j}\,\mathrm{d}x_j \\ &= \frac{1}{2\pi i\,\eta_j}\left(\psi_j(0) + \int_0^\infty \psi_j'(x_j) e^{-2\pi i\, x_j\cdot\eta_j}\,\mathrm{d}x_j\right) \end{aligned} \tag{4.21}$$

Since $\psi_j \equiv 1$ in a neighborhood U_j of p_j, we have that $\psi_j'(y_j) = 0$ for all y_j in U_j. Thus the remaining integral is the Fourier transform of a the smooth function $\mathbb{1}_{[0,\infty]}\psi_j'(x_j)$, hence of rapid decay in η_j. Therefore we obtain

$$\psi_j(0) + \int_0^\infty \psi_j'(x_j) e^{-2\pi i\, x_j\cdot\eta_j} \to \psi_j(0) \neq 0.$$

and hence asymptotically

$$\left|\int_0^\infty \psi_j(x_j) e^{-2\pi i\, x_j\cdot\eta_j}\,\mathrm{d}x_j\right| \asymp \frac{1}{|\eta_j|} \qquad \text{for all } j = d-m+1,\dots d. \tag{4.22}$$

For the estimate of the remaining factors of (4.19), i.e., for the indices $j = 1,\dots,d-m$, we note that there are constants $E, E' > 0$ such that for all $b > R_s$ and all it holds

$$E \le \int_{-b}^{b} |\hat{\psi}_j(\eta_j)|^2 \mathrm{d}\eta_j \le E' \tag{4.23}$$

and

$$E \le \int_{-b}^{b} \left|\int_0^\infty \psi_j(x_j) e^{-2\pi i x_j \eta_j} \mathrm{d}x_j\right|^2 \mathrm{d}\eta_j \le E'. \tag{4.24}$$

This is because the integrands in (4.23) and (4.24) are square-integrable and non-zero.

By the equations (4.20), (4.22), (4.23), and (4.24) we have estimated each factor of $|\widehat{\phi f}(\eta)|^2\langle\eta\rangle^{2s}$ from above and from below. From these estimates, we conclude that

$$\int_{V_{\alpha,R_s}} |\widehat{\phi f}(\eta)|^2 \langle\eta\rangle^{2s}\,\mathrm{d}\eta < \infty$$

if and only if

$$\int_{V'_{\alpha,R_s}} \frac{1}{|\eta_{d-m+1}|^2 \cdots |\eta_d|^2}(1+\eta_{d-m+1}^2+\ldots+\eta_n^2)^s \mathrm{d}\eta_{d-m+1}\cdots\mathrm{d}\eta_n < \infty, \tag{4.25}$$

where V'_{α,R_s} denotes the projection of V_{α,R_s} to the last $n-d+m$ components. Since the angle of aperture α was arbitrarily small, we may choose it so small that $|\eta_{d-m+1}|, ..., |\eta_d| > C \cdot \alpha > 0$ on V'_{α,R_s}, for some constant $C > 0$. Therefore we may transform (4.25) into polar coordinates and notice that the integral over the angular terms exists and is non-zero. Hence, the integral of (4.25) exists if and only if

$$\int_{R_s}^{\infty} r^{-2m}(1+r^2)^s r^{n-d+m-1}\mathrm{d}r < \infty.$$

This integral, in turn, exists if and only if

$$-2m+2s+n-d+m-1 < -1,$$

which is equivalent to

$$m > 2s+n-d.$$

Therefore, $\xi \in \Sigma_p^s(Q_d^n)$ if and only if

$$\xi_1 = ... = \xi_k = 0 \quad \text{and} \quad m \leq 2s+n-d.$$

Now we come to the second claim. By (4.6), the classical frequency set is the closure of the union of all H^s-frequency sets. Hence, we have

$$\Sigma_p(f) = \overline{\bigcup_{s\in\mathbb{R}} \Sigma_p^s(f)} = (\{0\}^k \times \mathbb{R}^{d-k}) \setminus \{0\} = \mathrm{GN}_p Q_d^n \setminus \{0\},$$

where the last equality follows from Proposition 4.30 by noting that here $\mathrm{rank}_{Q_d^n} p = k$. ∎

We give some particular examples of Theorem 4.37.

Example 4.38. 1. For the Dirac distribution $f = \mathrm{dS}_{\{0\}} = \delta$ in $\mathcal{D}'(\mathbb{R}^n)$ we have for $p = 0$ that $k = 0$ and $d = 0$, thus

$$\Sigma_0^s(f) = \begin{cases} \emptyset, & \text{if } s \in (-\infty, -\frac{n}{2}), \\ \mathbb{R}^n \setminus \{0\}, & \text{if } s \in [-\frac{n}{2}, \infty). \end{cases}$$

2. For the half line $f = \mathrm{dS}_{[0,\infty)}$ in $\mathcal{D}'(\mathbb{R}^2)$ and $p = (t, 0)$, $t > 0$, we have that $k = 1$, $d = 1$, so

$$\Sigma_p^s(f) = \begin{cases} \emptyset, & \text{if } s \in (-\infty, -\frac{1}{2}), \\ \{0\} \times (\mathbb{R} \setminus \{0\}), & \text{if } s \in [\frac{1}{2}, -\infty). \end{cases}$$

For $p = 0$, we have $k = 0$ and $d = 1$, so

$$\Sigma_0^s(f) = \begin{cases} \emptyset, & \text{if } s \in (-\infty, -\frac{1}{2}), \\ \{0\} \times (\mathbb{R} \setminus \{0\}), & \text{if } s \in [-\frac{1}{2}, 0), \\ \mathbb{R}^2 \setminus \{0\}, & \text{if } s \in [0, \infty). \end{cases}$$

3. For the quadrant $f = \mathrm{dS}_{[0,\infty)^2}$ in $\mathcal{D}'(\mathbb{R}^2)$ and $p = (t, 0)$, $t > 0$, we have that $k = 1$, $d = 2$, hence
$$\Sigma_p^s(f) = \begin{cases} \emptyset, & \text{if } s \in (-\infty, \tfrac{1}{2}). \\ \{0\} \times (\mathbb{R} \setminus \{0\}), & \text{if } s \in [\tfrac{1}{2}, \infty). \end{cases}$$
For $p = 0$, we have $k = 0$ and $d = 2$, so
$$\Sigma_0^s(f) = \begin{cases} \emptyset, & \text{if } s \in (-\infty, \tfrac{1}{2}), \\ \{(0, \lambda) : \lambda \in \mathbb{R} \setminus \{0\}\} \cup \{(\lambda, 0) : \lambda \in \mathbb{R} \setminus \{0\}\}, & \text{if } s \in [\tfrac{1}{2}, 1), \\ \mathbb{R}^2 \setminus \{0\}, & \text{if } s \in [1, \infty). \end{cases}$$
For $p = (p_1, p_2)$, where $p_1, p_2 \neq 0$, the H^s-frequency set is empty for every $s \in \mathbb{R}$, because p is not in the boundary of Q_d^n. ⌟

Having computed the frequency set of distinct points of the distributions $\mathrm{dS}_{Q_d^n}$ we now are able to compute the wavefront set of distributions integrating over a general submanifold with corners.

Theorem 4.39. *Let M be a C^∞-submanifold with corners which is closed $\mathbb{R}^n$. Then*
$$\mathrm{WF}(\mathrm{dS}_M) = \mathrm{GN}\, M \setminus \{0\}. \qquad ⌟$$

Proof. For $x \notin M$ we trivially have $\Sigma_x(\mathrm{dS}_M) = \emptyset = \mathrm{GN}_x M$. For $x \in M$, we choose a canonical chart with corners Φ for a neighborhood U of x. By the definition of canonical chart, $\Phi(x) = y$ is of the form $(y_1, ..., y_k, 0, ..., 0)$ for some $k \in \mathbb{N}$, where $y_1, ..., y_k \neq 0$. For $\psi \in \mathcal{D}(U)$, we have
$$\langle \mathrm{dS}_M, \psi \rangle = \int_{M \cap U} \psi \, \mathrm{dS}_M = \int_{Q_d^n \cap \Phi(U)} \psi(\Phi^{-1}(x)) |\det \mathrm{d}\Phi_x^{-1}| \, \mathrm{dS}_{Q_d^n} = \langle \Phi^* \mathrm{dS}_{Q_d^n}, \psi \rangle.$$
Hence, since the localized frequency set is local, it holds that
$$\Sigma_x(\mathrm{dS}_M) = \Sigma_x(\Phi^* \mathrm{dS}_{Q_d^n}).$$
This allows us to apply Theorem 4.8 (change of variables of the wavefront set) and Theorem 4.37 to obtain
$$\Sigma_x(\mathrm{dS}_M) = \Sigma_x(\Phi^* \mathrm{dS}_{Q_d^n}) = \mathrm{d}\Phi_x^T(\Sigma_{\Phi(x)}(\mathrm{dS}_{Q_d^n})) = \mathrm{d}\Phi_x^T(\mathrm{GN}_{\Phi(x)} Q_d^n) = \mathrm{GN}_x M.$$
Hence,
$$\mathrm{WF}(\mathrm{dS}_M) = \bigcup_{x \in M} \{x\} \times \Sigma_x(\mathrm{dS}_M) = \bigcup_{x \in M} \{x\} \times \mathrm{GN}_x M = \mathrm{GN}\, M,$$
which proves the assertion. ∎

Remark 4.40. If we restrict ourselves to classical manifolds, then Theorem 4.39 is a classical result for the wavefront set, see [Hö03, p. 265]. ⌟

Theorem 4.39 shows that the geometric normal bundle of a manifold with corners $\mathrm{GN}\, M \setminus \{0\}$ coincides with the wavefront set of its corresponding volume form dS_M. This correspondence now gives rise to the following edge model. We say that a distribution defines an edge if its wavefront set has the structure of a geometric normal bundle.

Definition 4.41. Let $f \in \mathcal{D}'(\mathbb{R}^n)$. We say that f is an *C^l-edge defining distribution* if there is a C^l-edge defining manifold M such that

$$\mathrm{WF}(f) = \mathrm{GN}\, M \setminus \{0\}.$$

We call $\operatorname{sing\,supp}(f) = \partial_{\mathbb{R}^n} M$ the *edge set of f*. ⌟

Remark 4.42.

- For any given f the edge set is uniquely determined, but the corresponding edge defining manifold M may be not unique. For example, the wavefront sets of the corresponding volume forms of the closed unit disk $\mathbb{D} = \{x \in \mathbb{R}^2 : |x| \leq 1\}$ and the torus $\mathbb{T} = \{x \in \mathbb{R}^2 : |x| = 1\}$ coincide, that is, $\mathrm{WF}(\mathrm{dS}_{\mathbb{D}}) = \mathrm{WF}(\mathrm{dS}_{\mathbb{T}})$.
- We could have used the volume forms dS_M themselves as edge model, but images composed exclusively of such volume forms then we would be "cartoon" images. But we would like to allow also smooth parts in between the edges, so we only postulate that the non-smooth part of a distribution has the structure of a volume form. ⌟

Up to now, we only have seen examples of C^∞ edge defining distributions. The existence of C^l-edge defining distributions, $l \in \mathbb{N}$, follows from the fact that we can find for each closed conic subset S of $\Omega \times (\mathbb{R}^n \setminus \{0\})$ a distribution $f \in \mathcal{D}'(\Omega)$ such that $\mathrm{WF}(f) = S$, cf. [Hö03, Theorem 8.1.4].

We see in the following that edge defining distributions are stable under the action of elliptic differential operators, which are defined as follows, cf. [Hö03, Section 8.3].

Definition 4.43. Let $\Omega \subset \mathbb{R}^n$ be open and $m \in \mathbb{N}_0$. A differential operator $P(x, D)$ of the form

$$P(x, D) \coloneqq \sum_{|\alpha| \leq m} a_\alpha(x) D^\alpha,$$

where $x \in \Omega$ and $a_\alpha \in C^\infty(\Omega)$, is called *differential operator with C^∞-coefficients of order m*. P is called *elliptic* its the principal part $P_m(x, \xi)$, defined by

$$P_m(x, \xi) = \sum_{|\alpha| = m} a_\alpha(x) \xi^\alpha,$$

has no zeros on $\Omega \times (\mathbb{R}^n \setminus \{0\})$. ⌟

The most prominent example of an elliptic differential operator is the Laplacian, denoted by Δ. An elliptic differential operator with C^∞-coefficients P has the important property that it does not alter the wavefront set, i.e., for any distribution f holds that

$$\mathrm{WF}(Pf) = \mathrm{WF}(f),$$

see [Hö03, Corollary 8.3.2]. This property provides us a way of how to construct a large variety of edge distribution from existing ones, for example from the volume forms dS_M.

Proposition 4.44. *Let $f \in \mathcal{D}'(\Omega)$ be a C^l-edge defining distribution and let $P(x, D)$ an elliptic differential operator with C^∞-coefficients. Then Pf is a C^l-edge defining distribution as well.* ⌟

Proof. Since P is elliptic, the wavefront sets of f and Pf coincide, see [Hö03, Corollary 8.3.2]. In particular, Pf is a C^l-edge defining distribution. ∎

To conclude this subsection, we summarize the relations between the geometric and the analytic edge model in Table 4.2.

	Geometric model	Analytic prototype
Edge defining objects	Submanifold with corners M	Volume form dS_M
Edge locations	Topological boundary $\partial_{\mathbb{R}^n} M$	Singular support $\operatorname{sing\,supp}(\mathrm{dS}_M)$
Edge orientations at $x \in \Omega$	Geom. normal space $\mathrm{GN}_x M \setminus \{0\}$	Frequency set $\Sigma_x(\mathrm{dS}_M)$

Table 4.2: Correspondence between a submanifold with corners M and its corresponding distribution dS_M.

4.3.3 Proof of functionality of the separation of edges in x-ray images

In the following, we derive conditions such that the proposed method for the separation of edges in x-ray images (Algorithm 1) works properly.

In analogy to the notation (4.2), we use the notation

$$\widetilde{\mathrm{GN}}_p M := (\mathrm{GN}_p M \setminus \{0\})/_\sim \subset \mathbb{P}^{n-1},$$

when we consider the geometric tangent or normal space as subset of the projective space $\mathbb{P}^{n-1}$, and likewise,

$$\widetilde{\mathrm{GN}}\, M := \bigcup_{p \in M} \{p\} \times (\mathrm{GN}_p M \setminus \{0\})/_\sim \subset \mathbb{R}^n \times \mathbb{P}^{n-1}.$$

Our first goal is to show that the edges we have modeled are connected in the phase space $\mathbb{R}^n \times \mathbb{P}^{n-1}$. To this end, we need the following preparations. We mention that connectedness is equivalent to path-connectedness for manifolds, see e.g. [Lee03].

Lemma 4.45. *Let M be a d-dimensional C^l-submanifold with corners of $\mathbb{R}^n$. Then $\mathrm{GN}_p M \neq \{0\}$ if $p \in \partial_{\mathbb{R}^n} M$ and $\mathrm{GN}_p M = \{0\}$ if $p \in M \setminus \partial_{\mathbb{R}^n} M$.* ⌟

Proof. Let $p \in M$ and Φ be a canonical chart with corners for p. Since Φ is a homeomorphism, $p \in \partial_{\mathbb{R}^n} M$ if and only if $\Phi(p) \in \partial_{\mathbb{R}^n} Q_d^n$. Assume that $p \in \partial_{\mathbb{R}^n} M$. Then $\Phi(p)$ lies on the boundary of the quadrant Q_d^n, so at least one component of $\Phi(p)$ vanishes. In consequence $r = \operatorname{rank}_M p \leq n-1$. By Proposition 4.30 it follows that $\dim(\mathrm{GN}_p M) = \dim(\{0\}^r \times \mathbb{R}^{n-r}) \geq \dim(\{0\}^{n-1} \times \mathbb{R}^1) = 1$. This implies in particular that $\mathrm{GN}_p M \neq \{0\}$. On the other hand, if we assume that $p \notin \partial_{\mathbb{R}^n} M$, then $\Phi(p)$ is an interior point of Q_d^n. This implies that the tangent space at p equals $\mathbb{R}^n$, and in consequence, for the normal space it holds that $\mathrm{GN}_p M = \{0\}$. ∎

Noting that $0 \in \mathbb{R}^n$ does not correspond to a point in projective space we get the following consequence.

Corollary 4.46. *Let M be a d-dimensional C^l-submanifold with corners of $\mathbb{R}^n$. Then, $\widetilde{\mathrm{GN}}_p M \neq \emptyset$ if and only if $p \in \partial_{\mathbb{R}^n} M$. In particular,*

$$\widetilde{\mathrm{GN}}\, M = \bigcup_{p \in \partial_{\mathbb{R}^n} M} \{p\} \times \widetilde{\mathrm{GN}}_p M.$$ ⌟

Lemma 4.47. *Let M be a d-dimensional C^l-submanifold with corners of $\mathbb{R}^n$. Then $\widetilde{\mathrm{GN}}_p M$ is connected for every $p \in \partial_{\mathbb{R}^n} M$.* ⌟

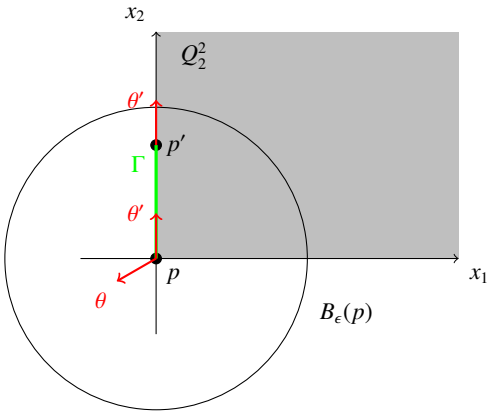

Figure 4.5: Illustration of the path construction in the proof of Lemma 4.48.

Proof. As $p \in \partial_{\mathbb{R}^n} M$ it follows that $\operatorname{rank}_M p \leq n-1$. First assume that $\operatorname{rank}_M p \leq n-2$. Since $\widetilde{\mathrm{GN}}_p M$ is a vector space of dimension greater or equal 2, the set $\mathrm{GN}_p M \setminus \{0\}$ is connected. Hence, the quotient space $(\mathrm{GN}_p M \setminus \{0\})/_\sim$ is connected as well. Next assume that $\operatorname{rank}_M p = n-1$. Then $\widetilde{\mathrm{GN}}_p M = (\mathrm{GN}_p M \setminus \{0\})/_\sim$ consists of single point which is connected. ∎

Now we can prove that the geometric normal bundle of a manifold with corners is connected.

Lemma 4.48. *Let $1 \leq d \leq n$. For each $p \in \partial_{\mathbb{R}^n} Q_d^n$ there is a neighborhood U of p such that $\widetilde{\mathrm{GN}}_{U \cap \partial_{\mathbb{R}^n} Q_d^n} Q_d^n$ is connected as subset of $\mathbb{R}^n \times \mathbb{P}^{n-1}$.* ⌟

Proof. Let (p, θ) be a point in the geometric normal bundle of the quadrant $\widetilde{\mathrm{GN}}_{\partial_{\mathbb{R}^n} Q_d^n} Q_d^n$. If $p = 0$, let

$$\epsilon = \begin{cases} \frac{1}{2} \min_{i \in \operatorname{supp} p} p_i, & \text{if } p \neq 0, \\ 1, & \text{if p = 0.} \end{cases}$$

Then, for each $q \in V := B_\epsilon(p) \cap \partial_{\mathbb{R}^n} Q_d^n$ any straight line between p and q is a subset of V. Choose any p' in $B_\epsilon(p)$ and any orientation $\theta' \in \widetilde{\mathrm{GN}}_{p'} Q_d^n$. We construct a path from (p, θ) to (p', θ'). First, construct a path Γ from p to p' by the parametrization

$$\gamma(t) = tp + (1-t)p', \qquad 0 \leq t \leq 1,$$

see also Figure 4.5. Since p and p' are both in V and since ϵ was chosen sufficiently small, the path Γ is in V. Further, it follows from the choice of ϵ that

$$\operatorname{supp} \gamma(s) = \operatorname{supp} p' \qquad \text{for each } s \in (0, 1].$$

Hence, it follows from (4.16) that

$$\mathrm{GN}_{\gamma(s)} M = \mathrm{GN}_{p'} M \subseteq \mathrm{GN}_p M, \qquad \text{for each } s \in (0, 1].$$

and the same relation holds true for the factor spaces

$$\widetilde{\mathrm{GN}}_{\gamma(s)} M = \widetilde{\mathrm{GN}}_{p'} M \subseteq \widetilde{\mathrm{GN}}_p M, \qquad \text{for each } s \in (0, 1].$$

In consequence, θ' is in $\widetilde{\mathrm{GN}}_{\gamma(t)}M$ for each $t \in [0,1]$, so $t \mapsto (\gamma(t), \theta')$ describes a path from (p, θ') to (p', θ') within $\widetilde{\mathrm{GN}}_V Q_d^n$. Since $\widetilde{\mathrm{GN}}_p M$ is connected (Lemma 4.47), there is a path from θ to θ' in $\widetilde{\mathrm{GN}}_p M$. Joining both paths together, we get a path from (p, θ) to (p', θ'). ∎

Theorem 4.49. *Let M be a d-dimensional C^l-submanifold with corners of $\mathbb{R}^n$. The geometric normal bundle $\widetilde{\mathrm{GN}}\, M$ is connected in $\mathbb{R}^n \times \mathbb{P}^{n-1}$ if and only if $\partial_{\mathbb{R}^n} M$ is connected in $\mathbb{R}^n$.* ⌟

Proof. If $\partial_{\mathbb{R}^n} M = \emptyset$, the statement is trivial, so we assume that $\partial_{\mathbb{R}^n} M \neq \emptyset$. First suppose that $\partial_{\mathbb{R}^n} M$ is connected in $\mathbb{R}^n$ and let $(p, \theta), (p', \theta') \in \widetilde{\mathrm{GN}}_{\partial_{\mathbb{R}^n} M} M$. Since $\partial_{\mathbb{R}^n} M$ is connected, there is a path Γ between p and p' in $\partial_{\mathbb{R}^n} M$. Let q be an arbitrary point on the path Γ and let Φ be a canonical chart with chart domain $U \subset \mathbb{R}^n$. By Lemma 4.48 we find an open neighborhood $V \subseteq \Phi(U)$ of $\Phi(q)$ such that

$$\widetilde{\mathrm{GN}}_{V \cap \partial_{\mathbb{R}^n} Q_d^n} Q_d^n$$

is connected. Now set $U' \coloneqq \Phi^{-1}(V) \subset U$. Since the pullback Φ^* is a homeomorphism, the set

$$\widetilde{\mathrm{GN}}_{U' \cap \partial_{\mathbb{R}^n} M} M = \Phi^* \widetilde{\mathrm{GN}}_{V \cap \partial_{\mathbb{R}^n} Q_d^n} Q_d^n$$

is connected. Since q was chosen arbitrarily, we find for every $q \in \Gamma$ such an open neighborhood U'. These U' form an open covering of Γ. As Γ is compact there is a finite covering say $U'_0, ..., U'_N$, where $N \in \mathbb{N}$. Further, since Γ is connected, we may assume that the U'_i are ordered such that

$$U'_{i-1} \cap U'_i \cap \Gamma \neq \emptyset, \quad \text{for all } i = 1, ..., N.$$

So there exists points $(q_i, \theta_i) \in U'_{i-1} \cap U'_i \cap \Gamma$ for all $i = 1, ..., N$. Since all the $\widetilde{\mathrm{GN}}_{U'_i \cap \partial_{\mathbb{R}^n} M} M$ are connected, there is a path from (q_{i-1}, θ_{i-1}) to (q_i, θ_i) in $\widetilde{\mathrm{GN}}_{U'_i \cap \partial_{\mathbb{R}^n} M} M$ for each $i = 1, ..., N$ and also from (p, θ) to (q_1, θ_1) and from (q_N, θ_N) to (p', θ'). Joining these paths together, we get a path from (p, θ) to (p', θ') in $\widetilde{\mathrm{GN}}_{\partial_{\mathbb{R}^n} M} M$. Hence, $\widetilde{\mathrm{GN}}_{\partial_{\mathbb{R}^n} M} M$ is connected.

For the opposite direction assume that $\widetilde{\mathrm{GN}}\, M$ is connected in $\mathbb{R}^n \times \mathbb{P}^{n-1}$. Since the projection onto the first component π_1 is continuous, $\partial_{\mathbb{R}^n} M = \pi_1(\widetilde{\mathrm{GN}}\, M)$ is connected. ∎

Theorem 4.49 in particular implies that the geometric normal bundle of an edge defining manifold, considered as subset of $\mathbb{R}^n \times \mathbb{P}^{n-1}$, is connected.

The key assumption for the functionality of our separation of edges algorithm will be the transversality of the edges, which we define in the following. First recall the definition of transversality for classical submanifolds. Two submanifolds (without corners) M_1, M_2 of $\mathbb{R}^n$ are said to be *transversal,* if for each $p \in M_1 \cap M_2$ the union of the tangent spaces $\mathrm{T}_p N_1$ and $\mathrm{T}_p N_2$ span the $\mathbb{R}^n$, cf. [Lee03, p. 128]. Analogously, we define a geometrically motivated transversality relation for manifolds with corners as follows.

Definition 4.50. Let M_i be a d_i-dimensional C^{l_i}-submanifold with corners of $\mathbb{R}^n$, where $0 \leq d_i \leq n$, $l_i \in \mathbb{N} \cup \{\infty\}$, and $i = 1, 2$. We define the relation

$$M_1 \pitchfork M_2 \quad :\Longleftrightarrow \quad \mathrm{GT}_p M_1 + \mathrm{GT}_p M_2 = \mathbb{R}^n \text{ for every } p \in M_1 \cap M_2.$$

If $M_1 \pitchfork M_2$, we say that M_1 and M_2 are *geometrically transversal*. If there exists $p \in M_1 \cap M_2$ such that $\mathrm{GT}_p M_1 + \mathrm{GT}_p M_2 \neq \mathbb{R}^n$, we say that M_1 and M_2 *intersect geometrically non-transversally.* ⌟

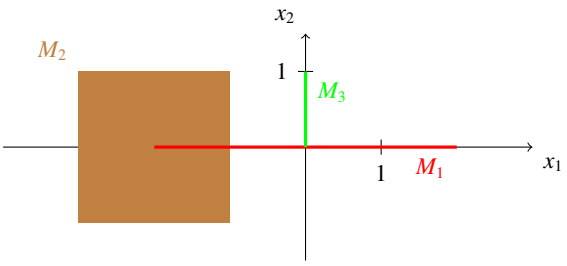

Figure 4.6: Illustration of the geometrically transversal intersection of the manifolds with corners $M_1 = [-2,2] \times \{0\}$, $M_2 = [-3,-1] \times [-1,1]$, and $M_3 = \{0\} \times [0,1]$. M_1 and M_2 intersect at the set $S = \{(t,0) : t \in [-1,0]\}$, but since $\mathrm{GT}_p M_1 + \mathrm{GT}_p M_2 = \mathbb{R}^2$, for each $p \in S$, M_1 and M_2 are geometrically transversal. As $M_2 \cap M_3 = \emptyset$, the manifolds M_2 and M_3 are geometrically transversal, as well. M_1 and M_3 do not intersect transversally, since the geometric tangent spaces at the intersection point $(0,0)$ do not span the $\mathbb{R}^2$.

The geometric transversality relation is illustrated in Figure 4.6. Geometric transversality can be characterized as follows.

Lemma 4.51. *Let M_i be a d_i-dimensional C^{l_i}-submanifold with corners of $\mathbb{R}^n$, where $0 \leq d_i \leq n$, $l_i \in \mathbb{N} \cup \{\infty\}$, and $i = 1,2$. Then the following statements are equivalent:*

(1) *M_1 and M_2 are geometrically transversal.*

(2) *$\mathrm{GT}_p M_1 + \mathrm{GT}_p M_2 = \mathbb{R}^n$ for every $p \in \partial_{\mathbb{R}^n} M_1 \cap \partial_{\mathbb{R}^n} M_2$.*

(3) *The intersection of the geometric normal spaces is the zero-space; that is, for every $p \in M_1 \cap M_2$ holds*

$$\mathrm{GN}_p M_1 \cap \mathrm{GN}_p M_2 = \{0\}. \tag{4.26}$$

(4) $\widetilde{\mathrm{GN}}\, M_1 \cap \widetilde{\mathrm{GN}}\, M_2 = \emptyset$. ⌟

Proof. *(1) ⇒ (2).* Clear by definition.

(2) ⇒ (1). By proposition $\mathrm{GT}_p M_1 + \mathrm{GT}_p M_2 = \mathbb{R}^n$ for $p \in \partial_{\mathbb{R}^n} M_1 \cap \partial_{\mathbb{R}^n} M_2$. As a consequence of Lemma 4.45, it holds $\mathrm{GT}_p M_i = \mathbb{R}^n$ if $p \in \mathrm{int}(M_i)$, $i = 1,2$. Since $M_1 \cap M_2 \subset \mathrm{int}(M_1) \cup \mathrm{int}(M_2) \cup (\partial_{\mathbb{R}^n} M_1 \cap \partial_{\mathbb{R}^n} M_2)$, we get $\mathrm{GT}_p M_1 + \mathrm{GT}_p M_2 = \mathbb{R}^n$ for every $p \in M_1 \cap M_2$, which is the definition of transversality.

(1) ⇔ (3). By definition holds $\mathrm{GT}_p M_1 + \mathrm{GT}_p M_2 = \mathbb{R}^n$ for every $p \in M_1 \cap M_2$, thus

$$\{0\} = (\mathbb{R}^n)^\perp = (\mathrm{GT}_p M_1 + \mathrm{GT}_p M_2)^\perp \supseteq (\mathrm{GT}_p M_1)^\perp \cap (\mathrm{GT}_p M_2)^\perp = \mathrm{GN}_p M_1 \cap \mathrm{GN}_p M_2.$$

(3) ⇔ (4). The assertion follows by

$$\widetilde{\mathrm{GN}}\, M_1 \cap \widetilde{\mathrm{GN}}\, M_2 = (\mathrm{GN}_p M_1 \cap \mathrm{GN}_p M_2 \setminus \{0\})/_\sim = \emptyset/_\sim = \emptyset.$$

■

Recalling the equality of the geometric normal bundle of a manifold with corners and the wavefront set of the corresponding volume form, cf. Theorem 4.39, equation (4.26) gives rise to the following definition of a transversality relation for distributions.

Definition 4.52. We say that two distributions $f, g \in \mathcal{D}'(\Omega)$ are *transversal,* if

$$\mathrm{WF}(f) \cap \mathrm{WF}(g) = \emptyset.$$ ⌟

As last lemma for the proof of the main theorem of this section, we need an elementary assertion about the wavefront set of the sum of distributions.

Lemma 4.53. *Let $f, g \in \mathcal{D}'(\Omega)$. Then*

$$(\mathrm{WF}(f) \cap \mathrm{WF}(g)) \cup \mathrm{WF}(f+g) = \mathrm{WF}(f) \cup \mathrm{WF}(g). \qquad \lrcorner$$

Proof. It is sufficient to show

$$(\Sigma(f) \cap \Sigma(g)) \cup \Sigma(f+g) = \Sigma(f) \cup \Sigma(g)$$

for compactly supported f and g. The assertion then follows from the definition of the wavefront set.

First assume that $\xi_0 \notin \Sigma(f) \cup \Sigma(g)$. Then there is a common conic neighborhood V of ξ_0 such that both $|\hat{f}|$ and $|\hat{g}|$ are of rapid decay in V. Hence $|\widehat{f+g}| \leq |\hat{f}| + |\hat{g}|$ is of rapid decay in V, meaning that $\xi_0 \notin \Sigma(f+g)$. Since the relation $\xi_0 \notin \Sigma(f) \cap \Sigma(g)$ is trivial, the inclusion "$\subset$" is proven.

Next let $\xi_0 \in \Sigma(f) \cup \Sigma(g)$. For $\xi_0 \in \Sigma(f) \cap \Sigma(g)$ there is nothing to show. So without loss of generality we may assume that $\xi_0 \in \Sigma(f)$ and $\xi_0 \notin \Sigma(g)$, the remaining case follows from interchanging f and g. We show that $\xi_0 \in \Sigma(f+g)$ by contradiction. To this end we suppose that $\xi_0 \notin \Sigma(f+g)$. Then there is a conic neighborhood V of ξ_0 such that $|\hat{f}|$ is not of rapid decay and both $|\hat{g}|$ and $|\widehat{f+g}|$ are of rapid decay in V. So we get from

$$|\hat{f}| \leq |\hat{f} + \hat{g} - \hat{g}| \leq |\widehat{f+g}| + |\hat{g}|$$

that $\hat{f}$ is of rapid decay on V. This contradicts the assumption $\xi_0 \in \Sigma(f)$. So $\xi_0 \in \Sigma(f+g)$, which completes the second inclusion "$\supset$". ∎

We now use the results obtained so far to prove the functionality of Algorithm 1 under the geometric condition that the C^l-edges M_j are pairwise transversal.

Theorem 4.54. *Let f_j be C^l-edge defining distributions with corners for $j = 1, ..., N$, where $N \in \mathbb{N}$. Consider the x-ray type image*

$$f = \sum_{j=1}^{N} f_j,$$

and let W_k, $k = 1, ..., N'$ be the $N' \in \mathbb{N}$ connected components of $\mathrm{WF}(f)$. *If the f_j are pairwise transversal, then $N = N'$, and there is a permutation $\sigma : \{1, \ldots, N\} \to \{1, \ldots, N\}$ such that*

$$W_{\sigma(j)} = \mathrm{WF}(f_j), \qquad \textit{for all } j = 1, \ldots, N.$$

In particular,

$$\pi_1(W_{\sigma(j)}) = \operatorname{sing\,supp} f_j, \qquad \textit{for all } j = 1, \ldots, N. \qquad \lrcorner$$

Proof. Since f_j is an edge defining distribution, $j = 1, ..., N$, there is by definition a manifold with corners M_j such that $\partial_{\mathbb{R}^n} M_j$ is connected and

$$\widetilde{\mathrm{WF}}(f_j) = \widetilde{\mathrm{GN}}\, M_j.$$

From Theorem 4.49 it follows that the geometric normal bundle $\widetilde{\mathrm{GN}}\, M_j$ is connected in $\mathbb{R}^n \times \mathbb{P}^{n-1}$, hence $\widetilde{\mathrm{WF}}(f_j)$ is connected in $\mathbb{R}^n \times \mathbb{P}^{n-1}$ for all $j = 1, ..., N$. Since the f_j are pairwise transversal, i.e.,

$$\widetilde{\mathrm{WF}}(f_j) \cap \widetilde{\mathrm{WF}}(f_i) = \emptyset, \qquad \text{for each } i \neq j,$$

it follows from Lemma 4.53 that

$$\widetilde{\mathrm{WF}}(f) = \widetilde{\mathrm{WF}}(\sum_{j=1}^{N} f_j) = \widetilde{\mathrm{WF}}(f_1) \dot{\cup} \ldots \dot{\cup} \widetilde{\mathrm{WF}}(f_N),$$

where the union is disjoint. Since the wavefront set is a closed subset of $\mathbb{R}^n \times \mathbb{P}^{n-1}$, we get that $\widetilde{\mathrm{WF}}(f_j) \dot{\cup} \widetilde{\mathrm{WF}}(f_k)$ is not connected whenever $j \neq k$. Hence, the wavefront set of f consists indeed of N connected components. Altogether, the connected components of the wavefront set of f correspond, up to a reordering, to the wavefront sets of the distributions $f_1, ..., f_N$, which is the first part of the claim.

The second assertion is a direct consequence, because the singular support is the projection of the wavefront set onto the first component. ∎

4.4 Further references

The wavefront set was developed mainly by Hörmander for the analysis of linear partial differential operators in the 1970ies; see the textbook [Hö03]. The usability of the wavefront set for imaging was recognized in the work of Quinto [Qui93] where microlocal analysis is used to characterize reconstructable image structures in limited angle tomography. A recent application in this context are edge-preserving limited angle reconstruction algorithms which exploit the correspondence of the wavefront set and curvelet coefficients [Fri12].

The one-to-one correspondence between the wavefront set and the decay rates of curvelet coefficients has been established by Candès and Donoho [CD05a], analogous results for the shearlet coefficients have been shown by Kutyniok and Labate [KL09]. Frequently occurring edge structures, such as corners, lines and curves, have been investigated in terms of decay rates of curvelet and shearlet coefficients in [CD05a] and [GL09], respectively.

Edge models have been proposed in various forms. Probably the most widely known is the Canny-type model [Can86], where edges are considered to be local maxima of the gradient with respect to the gradient direction. Another approach is to consider an image as the composition of functions belonging to a class of model functions. For example, in [CD04], images are considered to consist of functions which are two-times differentiable except on a set of piecewise C^2-curves. Edge detection based on shearlet coefficients was considered in [GL09] for that model. Besides these local models, there exist non-local edge models relying on variational analysis. For example, the Mumford-Shah functional [MS89] seeks for the optimal trade-off between the approximation error by a function which is smooth except from an edge set and the length of that edge set. An overview of the mentioned edge models is given in Table 4.3. Note that this list only contains the most frequently used models and is not exhaustive.

The processing of crossing structures in x-ray images has been investigated by Duits [Dui05] and Franken [Fra08] who analyze crossing elongated structures by a so called orientation score.

	Edge model	Mathematical basis
Canny [Can86]	Local maxima of gradient w.r.t. gradient direction	Image gradient
Donoho/Candès [CD04]	C^2-functions away from C^2-curves	Class of model functions
Mumford/Shah [MS89]	Edges determined by best approximation piecewise smooth approximation	Variational approach
This work	Distributions whose wavefront set have the structure of a geometric normal bundle	Wavefront set

Table 4.3: Comparison of the proposed edge models to some important classical edge models.

An orientation score is a decomposition of an image into different orientations but only on one fixed scale. Thus, the orientation score lacks a multiscale aspect.

A geometric separation problem related to the separation of edges has been investigated in the work of Donoho and Kutyniok [KL12]. There, curvilinear structures are separated from point-like structures by the joint sparsity of wavelet-shearlet frame.

Chapter 5

Signal and image analysis based on complex wavelet signs

We have seen in the last chapter that the amplitudes of the wavelet coefficients are closely connected to the classical theory of microlocal analysis. The signs of the wavelet coefficients, in contrast, do not correspond to such a well established theory. Although first indications to the usability of the signs of the wavelet coefficients have been given in [KMMG87], [Hol95], and [Mal09], wavelet signs are still poorly understood and thus rarely used for signal and image analysis. This stands in contrast to the fact that the wavelet signs carry a great portion of the signal and image structure, which we illustrate in Section 5.1.

In this chapter, we derive a novel method for local signal analysis based on complex wavelet signs, called *discrete signature,* which we apply for the detection of salient points or edges. To this end, we first study the behavior of the wavelet signs for basic one-dimensional signals (Section 5.2). We observe that the wavelet signs stay nearly constant at salient points but vary strongly at non-salient points. These observations motivate to measure the local variation of the wavelet signs and to consider the points of low variation as salient points. We use directional statistics to measure the variation of the wavelet signs. We verify in a series of numerical experiments that our method reliably detects salient points of a signal, such as jumps and cusp. Our experiments further indicate that the discrete signature distinguishes between locally symmetric and locally antisymmetric feature points. This gives complementary information to the amplitude-based signal analysis, which determines the local order of smoothness.

We generalize the discrete signature to higher dimensions using monogenic wavelets and apply this approach to edge detection (Section 5.3). We shall see that our sign based method competes with the phase congruency based edge detection methods of [Kov99] and [FS00]. In many of our experiments, the discrete signature yields a better balance between the detection of the pronounced structures and of the fine details than phase congruency.

In Section 5.4, we point out the main conceptual advantages of the discrete signature over phase congruency. Whereas phase congruency requires several additional heuristics, which introduce extra parameters, it is remarkable that our discrete signature neither requires pre- or post-processing nor any further heuristics.

5.1 The importance of wavelet signs in images

The goal of this section is to illustrate the importance of the sign of the wavelet coefficients for the image structure. To this end, we decompose an image $f \in L^2(\mathbb{R}^2, \mathbb{R})$ into its complex wavelet coefficients and shuffle either their amplitudes or their signs. (See Section 1.2 for the definitions

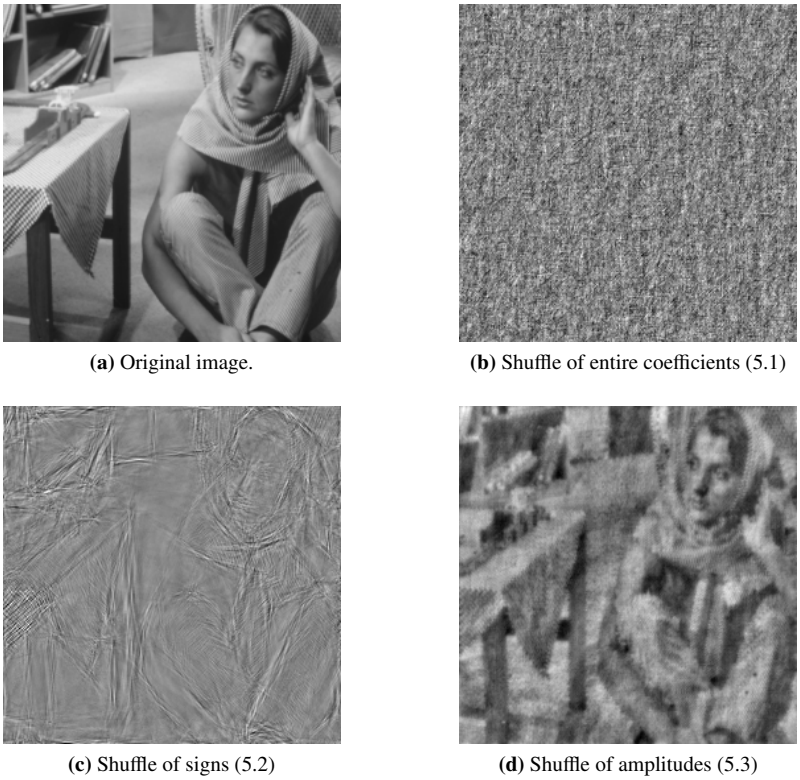

(a) Original image.

(b) Shuffle of entire coefficients (5.1)

(c) Shuffle of signs (5.2)

(d) Shuffle of amplitudes (5.3)

Figure 5.1: The effect of shuffling the wavelet coefficients of an image. (b) A random shuffle of the entire coefficients totally destroys the image structure as expected. (c) The shuffled sign destroys nearly all the image structure. Only the locations of the edges can be recognized. (d) After shuffling the amplitudes, the image appears noisy but the image structure is clearly recognizable. In order to emphasize the described effects the highpass and lowpass residuals were removed in all three experiments.

of amplitude and sign of a complex number.) We will see that a loss of sign information destroys much more of the image structure than a loss of amplitude information, cf. Figure 5.1. This indicates that the signs of the wavelet coefficients are more important for the reconstruction process.

The concrete experiment is as follows. Let ψ be a real-valued wavelet such that the family $\{\psi_{j,k,l}\}_{j,k,l}$ forms a Parseval frame for $L^2(\mathbb{R}^2, \mathbb{R})$, and thus the reconstruction formula

$$f = \sum_{j,k,l} \langle f, \psi_{j,k,l} \rangle \psi_{j,k,l}, \quad \text{in } L^2(\mathbb{R}^2, \mathbb{R}),$$

is valid. Let $c_{j,k,l} = \langle \mathcal{R}' \psi_{j,k,l}, f \rangle$ be the $\mathcal{R}$-complex wavelet coefficients of f and let π be a random permutation. We compare the following three types of reconstruction. The random permutation the raw wavelet coefficients,

$$f_{\mathrm{rc}} = \sum_{j,k,l} c_{j,\pi(k),l} \, \psi_{j,k,l}, \tag{5.1}$$

the random permutation of the signs of the coefficients

$$f_{\mathrm{rs}} = \sum_{j,k,l} |c_{j,k,l}| \operatorname{sgn}\left(c_{j,\pi(k),l}\right) \psi_{j,k,l}, \tag{5.2}$$

and the random permutation of the amplitudes of the coefficients,

$$f_{\mathrm{ra}} = \sum_{j,k,l} |c_{j,\pi(k),l}| \operatorname{sgn}\left(c_{j,k,l}\right) \psi_{j,k,l}. \tag{5.3}$$

The outcome of this experiment is presented in Figure 5.1. As expected, the image information gets completely lost after a shuffle of the wavelet coefficients (Figure 5.1b). In Figure 5.1d we observe that most of the image structure is preserved if the coefficients' amplitudes are shuffled and the signs are kept. The reconstruction appears noisy but the picture is still well recognizable. On the other hand, a permutation of the coefficients' signs destroys the structure of the image almost completely, only slight contours remain visible; see Figure 5.1c. In this experiment, we chose ψ to be a directional wavelet of the type (3.10) with $N = 8$ orientations and the Riesz transform as quadrature operator. However note that the choice of the wavelet is not critical for the outcome of this experiment, similar results can be obtained using for example isotropic monogenic wavelets [Sto08, HSMF10], monogenic curvelets, or shearlets.

To summarize, this experiment illustrates that a great portion of an image's information content is coded in the wavelet signs.

Remark 5.1. Analogous observations about the importance of signs in images have been made in [OL81] for Fourier coefficients, in [Lee96] for Gabor wavelet coefficients, and in [HSMF10] for steerable wavelets based on the Riesz transform. To the author's knowledge there is no rigorous mathematical explanation for these observations. A positive result in that direction has been given by Logan [LJ77] in a one-dimensional setting. Logan showed that, under mild assumptions, bandpass signals are determined up to a constant by their sign information.

5.2 The wavelet sign for local signal analysis

We have motivated the important role of the wavelet signs in the last section. We now aim for exploiting the rich information coded in the wavelet signs for signal analysis.

In what follows we restrict ourselves to those wavelets whose Fourier transforms are real-valued, smooth, and supported in a compact subset of the positive real-axis. To fix ideas, we use the Meyer-type complex wavelet κ, which is defined by the inverse Fourier transform of the (one-sided) Meyer window W; that is,

$$\kappa(x) = \mathcal{F}^{-1}(W)(x). \tag{5.4}$$

The graphs of κ and W are depicted in Figure 5.2. The exact definition of W is provided in Section A.2. Because of its one-sided frequency spectrum, κ is a complex wavelet of the form

$$\kappa = \psi + i\mathcal{H}\psi, \tag{5.5}$$

where $\psi = \operatorname{Re}\kappa$ is a real-valued bandpass wavelet; cf. Section 2.1.

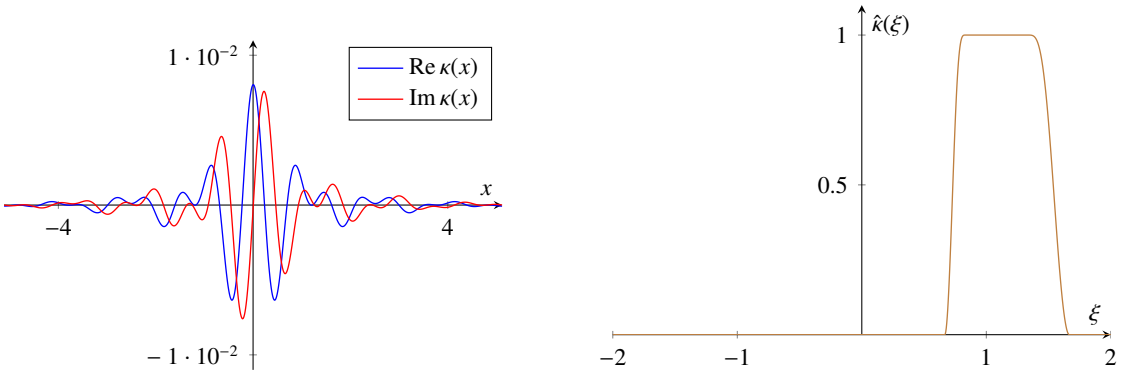

Figure 5.2: The complex Meyer-type wavelet κ (left) and its Fourier transform $\hat{\kappa} = W$ (right).

Behavior of wavelet signs at salient and non-salient points To derive a sign-based signal analysis tool, we investigate the fine scale behavior of the wavelet signs, $\operatorname{sgn}\langle f, \kappa_{a,b}\rangle$, for some typical salient signal structures such as jumps and cusps. Let us start with the unit step function $u = \mathbb{1}_{[0,\infty)}$. The wavelet coefficients centered around the origin are given by

$$\langle u, \kappa_{a,0}\rangle = \langle \widehat{u}, (\kappa_{a,0})^\vee\rangle = \sqrt{a}\int_{\mathbb{R}} \frac{\kappa^\vee(a\xi)}{i\pi\xi}\,\mathrm{d}\xi = i\frac{\sqrt{a}}{\pi}\int_{\mathbb{R}} \frac{\hat{\kappa}(a\xi)}{\xi}\,\mathrm{d}\xi. \tag{5.6}$$

(See Table A.1 for the Fourier transform of the unit step.) As $\hat{\kappa}$ is one-sided, non-negative and supported in a compact set away from the origin, the integral is positive. Thus, the sign of the wavelet coefficient equals i for all scales $a > 0$, i.e.,

$$\operatorname{sgn}\langle u, \kappa_{a,0}\rangle = i. \tag{5.7}$$

Likewise, we calculate the wavelet signs of a cusp function $x \mapsto |x|^\gamma$, where $0 < \gamma \leq 1$. By the formula for the Fourier transform of $|\bullet|^\gamma$, cf. [GSS64, II.2.3, eq. 12], we get that

$$\langle |\bullet|^\gamma, \kappa_{a,0}\rangle = \langle \widehat{|\bullet|^\gamma}, (\kappa_{a,0})^\vee\rangle = -\sin\left(\frac{\pi\gamma}{2}\right)\Gamma(\gamma+1)\int_{\mathbb{R}} \frac{(\kappa_{a,0})^\vee(\xi)}{|\xi|^{\gamma+1}}\mathrm{d}\xi. \tag{5.8}$$

Thus, the wavelet signs are equal to

$$\operatorname{sgn}\langle |\bullet|^\gamma, \kappa_{a,0}\rangle = -1, \quad \text{for all } a > 0. \tag{5.9}$$

Now let us consider the case where the wavelet is not centered around the origin, thus for $b \neq 0$. Then, the translation by b introduces a modulation in the integrals of (5.6) and (5.8), and thus, the integrals are not any more strictly positive. In consequence, the wavelet signs are not any more constant with respect to the scale a, that is, the functions $a \mapsto \operatorname{sgn}\langle u, \kappa_{a,b}\rangle$ and $a \mapsto \operatorname{sgn}\langle |\bullet|^\gamma, \kappa_{a,b}\rangle$ are oscillatory.

The discrete signature as measurement of wavelet sign variation In the above examples, the signs of the wavelet coefficients are constant for all scales a at the singular point $b = 0$ and non-constant at the non-singular points $b \neq 0$. This observation motivates to consider a point $b \in \mathbb{R}$ as

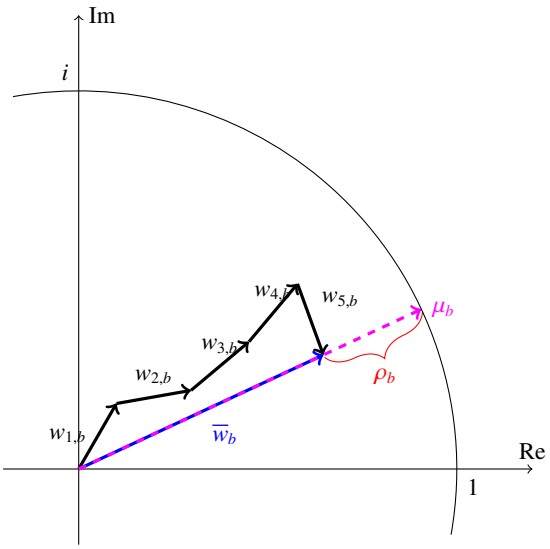

Figure 5.3: Illustration of the moments of the directional statistics of the wavelet signs $w_{j,b}$ for a fixed location b and five scale samples a_j, where $j = 1, ..., 5$. The signs $w_{j,b}$ of all scales $j = 1, \dots, 5$ are composed head to tail in the complex plane. The length of the mean resultant vector $\overline{w}_b = \frac{1}{5}\sum_{j=1}^{5} w_{j,b}$ equals to one minus the directional variance, i.e., $|\overline{w}_b| = 1 - \rho_b$. The directional mean μ_b is the orientation of the mean resultant vector, that is, $\mu_b = \operatorname{sgn} \overline{w}_b$.

a salient point of the signal if the wavelet signs $\operatorname{sgn}\langle f, \kappa_{a,b}\rangle$ are constant or only slowly varying in a. Those points where the signs are far from being constant at are considered to be regular points.

Our next goal is to realize these observations as a numerically tractable indicator to local feature points. To that end, we switch to a semi-discrete setting, i.e., we take a finite number of scale samples $\{a_j\}_{j=1}^N$ and denote the corresponding wavelet signs by

$$w_{j,b} := \operatorname{sgn}\langle f, \kappa_{a_j,b}\rangle.$$

Following our observations about the basic signals, we aim for measuring whether the wavelet signs $w_{j,b}$ are close to being constant or whether they have strong variations with respect to j. To achieve this we regard the signs of the wavelet coefficients as directions within the complex plane and then utilize the framework of *directional statistics* to measure their variation. Directional statistics describes the statistical properties of a sample set of directions; see e.g. [Fis96] for an introduction to this topic. The basic descriptor of the data set $\{w_{j,b}\}_{j=1}^N$ is the ordinary mean value of the sample set, given by

$$\overline{w}_b = \frac{1}{N}\sum_{j=1}^{N} w_{j,b} \quad \in \mathbb{C}. \tag{5.10}$$

In the context of directional statistics, the magnitude $\overline{w}_b$ is called *mean resultant vector*. The moments of the data set, the *directional mean* $\mu_b \in \mathbb{C}$ and the *directional variance* $\rho_b \in [0, 1]$, derive directly from that mean resultant vector. The directional mean is defined by

$$\mu_b = \operatorname{sgn} \overline{w}_b$$

Signal	Feature type	Wavelet signs at $b = 0$
Unit step u	Step to right	$+i$
Negative unit step $-u$	Step to left	$-i$
Negative power of modulus $-\lvert\bullet\rvert^\gamma$	Cusp upwards	$+1$
Power of modulus $\lvert\bullet\rvert^\gamma$	Cusp downwards	-1

Table 5.1: Correspondence of feature types and wavelet signs at location $b = 0$ for unit steps and pure cusp singularities. For the steps, the wavelet signs are imaginary. For the cusps, the wavelet signs are real.

and the directional variance by

$$\rho_b = 1 - |\overline{w}_b| \,.$$

The moments of directional statistics are illustrated in Figure 5.3. The directional variance can be interpreted as a measure for the variation of the orientations in the complex plane. Thus, we consider the wavelet signs to be slowly varying if their directional variance is low; more precisely, if the directional variance ρ_b falls below some threshold $\tau' \in [0, 1]$. In that case, the directional mean μ_b can be interpreted as an estimate of the overall orientation of the sample set. This motivation gives rise to define the quantity

$$\overline{\sigma} f(b) := \begin{cases} \mu_b, & \text{if } \rho_b < \tau', \\ 0, & \text{else,} \end{cases}$$

which we call *discrete signature.* The discrete signature is equal to zero in the case of high directional variance, and is equal to the directional mean in the case of low directional variance. We can rewrite this directly in terms of the mean resultant vector $\overline{w}_b$ as

$$\overline{\sigma} f(b) = \begin{cases} \operatorname{sgn} \overline{w}_b, & \text{if } |\overline{w}_b| > \tau, \\ 0, & \text{else,} \end{cases} \tag{5.11}$$

where $\tau = 1 - \tau'$. Let us summarize the idea of the discrete signature. The discrete signature is a complex number of modulus 1 at a salient point of a signal and equal to 0 at a non-salient point.

So far, we only have an interpretation for the modulus of the discrete signature. However, the discrete signature gives further information about the local shape of a salient point. To motivate this, let us again take a look at the wavelet signs of the step and the cusp singularities. We on the one hand observe that the symmetric cusp singularity has real wavelet signs, see (5.9). At the antisymmetric step singularity, on the other hand, the wavelet signs are imaginary, cf. (5.7). These correspondences, which are tabulated in Table 5.1, suggest to interpret the discrete signature as an indicator of local symmetry. A real discrete signature indicates a locally symmetric feature point, such as a cusp, and an imaginary discrete signature indicates a locally antisymmetric feature point, such as a step.

Numerical experiments We confirm by a series numerical experiments that the discrete signature indeed is in accordance with our interpretations made in the previous paragraphs. Here, we use the scale sample sequence $a_j = 2^{-\frac{j}{3}}$, where $j = 1, ..., 12$. The threshold value $\tau = 0.7$

turned out to be a reasonable choice. The first experiment (Figure 5.4) shows that the numerical estimates coincides with our observations for steps and cusps made in the beginning of the section. In particular, the directional variance is low at the salient points and high at the regular parts away from the jump and cusp locations (second row in Figure 5.4). We further observe that the peaks in the moduli of the mean resultant vector are sharply localized around the salient points, so no further post-processing, such as non-maximum suppression, is required. Also for a more complex signal, we observe that the discrete signature has a large absolute value at the salient points; see Figure 5.5. The experiments also show that the discrete signature clusters around the imaginary axis for locally antisymmetric step-type singularities and around the real axis for locally symmetric cusp-like singularities (third rows in Figure 5.4 and Figure 5.5). This backs our interpretation of the discrete signature as indicator to local symmetry and antisymmetry.

5.3 An extension of the discrete signature to higher dimensions

Our next goal is the generalization of the discrete signature to higher dimensions. To this end, let us reconsider its one-dimensional definition (5.11). The difficulty of a generalization to higher dimensions lies mainly in the generalization of the complex wavelet κ. But recall that we already know from Chapter 3 several reasonable constructions of higher dimensional complex wavelets. We here focus for the sake of simplicity on the following isotropic monogenic wavelets, a comment on the use of anisotropic complex wavelets is given at the end of the section. Let ψ be real-valued and isotropic bandpass wavelets of the form

$$\psi(x) = \mathcal{F}^{-1}(W(|\bullet|))(x), \tag{5.12}$$

where W is again the Meyer window function, see Section A.2. Recall from Chapter 2 that the Riesz transform is the natural quadrature operator for isotropic wavelets, so we deal with the isotropic monogenic wavelet $\kappa : \mathbb{R}^n \to \mathbb{R}^{1+n}$ defined by

$$\kappa = \psi + \mathcal{R}\psi.$$

The isotropic discrete signature Although the wavelet coefficients with respect to κ are vectors in $\mathbb{R}^{1+n}$, the moments of directional statistics in $1+n$ dimensions are defined in complete analogy to the planar case, see e.g. [FLE93]. Thus, we may proceed in exactly the same way as in the one dimensional case. We choose a scale sampling set $\{a_j\}_{j=1}^N$ and compute the mean resultant vector at some point $b \in \mathbb{R}^n$ by

$$\overline{w}_b = \frac{1}{N}\sum_{j=1}^{N} \operatorname{sgn}\langle f, \kappa_{a_j,b}\rangle \quad \in \mathbb{R}^{1+n}. \tag{5.13}$$

Then, in analogy to the one-dimensional formula (5.11), we define the *discrete isotropic signature* by

$$\overline{\sigma} f(b) = \begin{cases} \operatorname{sgn} \overline{w}_b, & \text{if } |\overline{w}_b| > \tau, \\ 0, & \text{else,} \end{cases} \tag{5.14}$$

where τ is a threshold parameter between 0 and 1. Following the ideas of the one dimensional case, the isotropic discrete signature is a vector of modulus one at an "edge" and is equal to zero

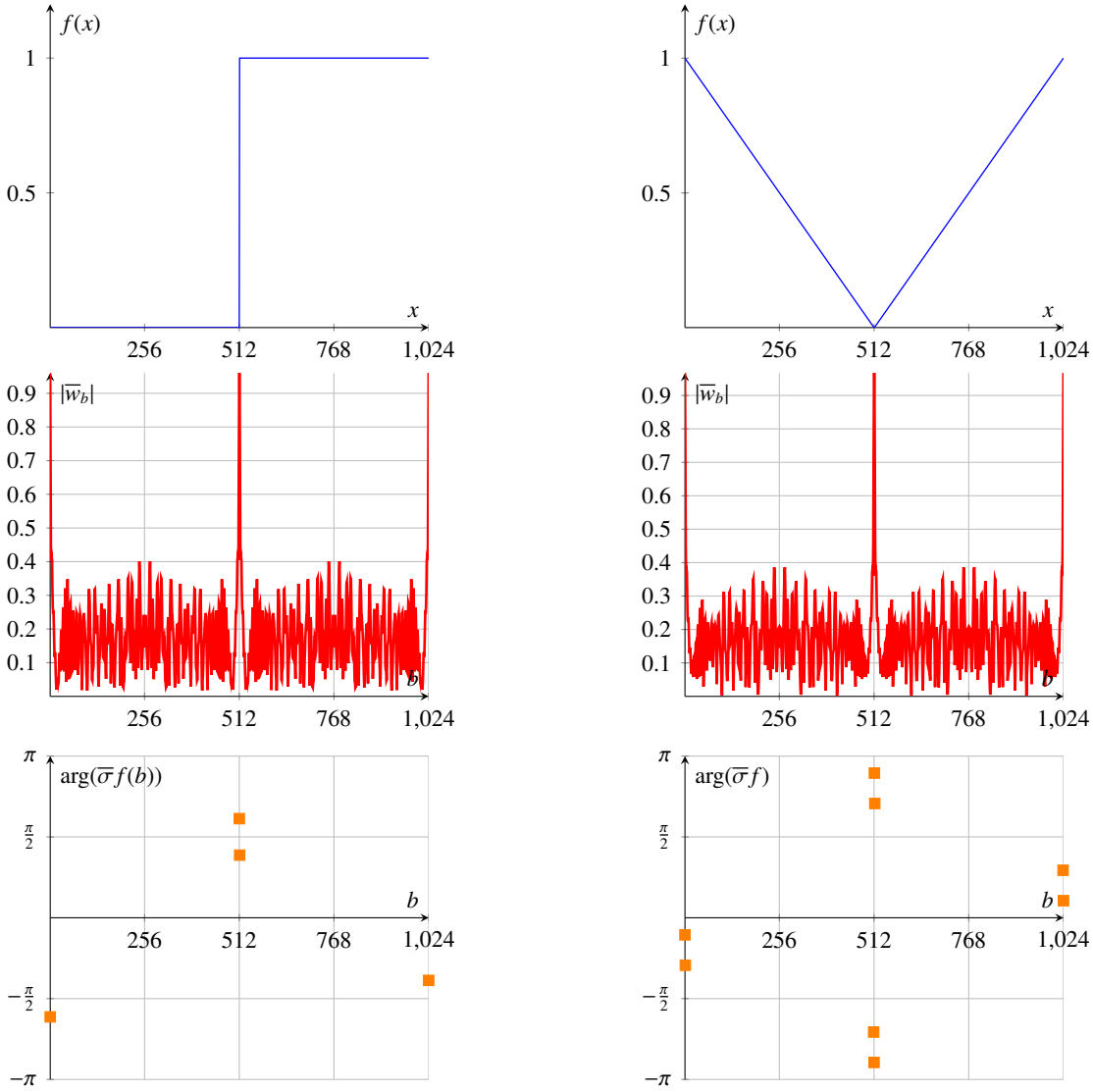

Figure 5.4: The discrete signature of two sample signals. We observe that the absolute value of the resultant vector $\overline{w}_b$ is close to one at the salient points, here a step and a cusp, and much lower at the remaining points (second row). We also see that the peaks are sharply localized, so we do not necessarily require a non-maximum suppression here. In the third row, the discrete signature according to (5.11) is depicted as phase angle (threshold $\tau = 0.7$). We see that the orientations in the complex plane of the discrete signature is close to the angle $\pm\frac{\pi}{2}$ at the step singularity (right). At the cusp, the signature angles group around the angle π (or $-\pi$). Note that the extra points at the interval boundaries are due to the periodization of the signal.

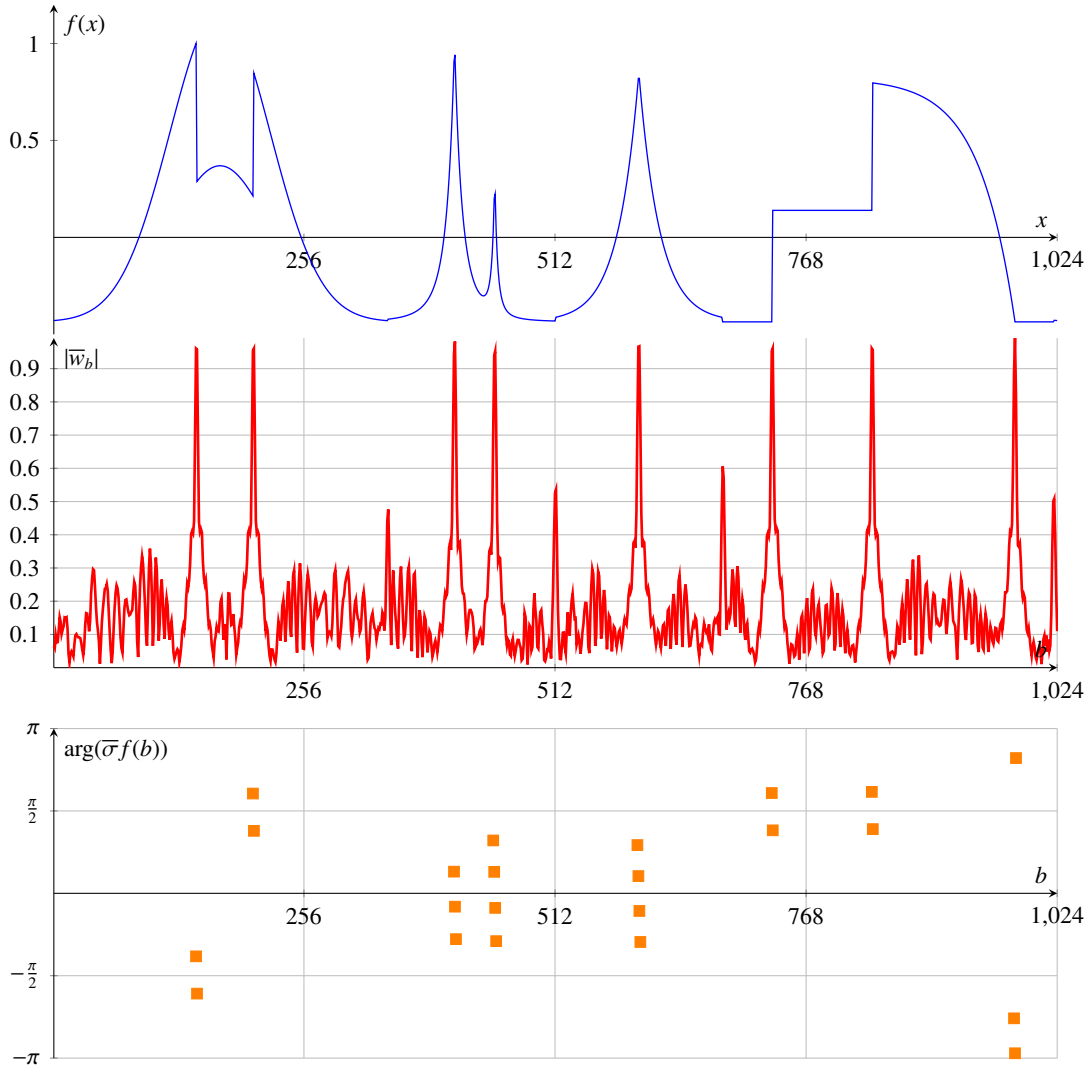

Figure 5.5: The discrete signature of a sample signal, taken from Wavelab [DMS06]. We observe that the absolute value of the resultant vector $\overline{w}_b$ is close to one at the salient points, here a step and a cusp, and much lower at the remaining points. We also see that the peaks are sharply localized, so we do not require a non-maximum suppression here. In the third row, the discrete signature according to (5.11) is depicted as phase angle (threshold $\tau = 0.7$). We see that the signature is close to the angle $\pm\frac{\pi}{2}$, at the steps, whereas at the cusps, the signature angles group around π and 0.

at a regular point of the image. Note that the term "edge" has to be understood in an abstract sense in this context, since no rigorous characterization of the points of non-zero discrete signature is known. In particular, an edge detected by the discrete signature need not to be in the singular support of the image, which was postulated in our microlocal edge model of the last chapter.

Numerical experiments We evaluate the performance of the discrete signature for edge detection in a series of numerical experiments. The results are presented in the Figures 5.6, 5.7, and 5.8. The set-up for the experiments is as follows. We use again a scale sampling of $a_j = 2^{-\frac{j}{3}}$, where $j = 1, ..., 12$. If not indicated otherwise the threshold value $\tau = 0.7$ is used. In Figure 5.6, we see the edge detection capabilities of the discrete signature. The discrete signature equals zero at the regular points of the image, whereas is a vector of modulus one at the edges or salient points. In the color-coded Figure 5.7, we observe that the imaginary part of the discrete signature dominates the real part at step edges, and that it behaves the other way round at line edges. This gives rise to the conjecture that the orientation of $\overline{\sigma} f(b)$ within the $\mathbb{R}^{1+2}$ can discriminate between line-like and step-like edges. The final experiment in Figure 5.8 illustrates that our edge detection method directly applies to three dimensional images.

Remark 5.2. We also could build a generalized discrete signature on anisotropic complex wavelet transforms, such as monogenic curvelets or shearlets. We here have focused on isotropic monogenic wavelets because these provided the best immediate edge detection results amongst the complex wavelets construction we have seen in Chapter 3. ⌟

To summarize, we have seen how the discrete signature can be generalized to higher dimensions by monogenic wavelets. We emphasize that this generalization yields a direct method for edge detection without any pre- and post-processing, or any further heuristics.

5.4 Comparison to phase congruency

We point out the differences between the discrete signature and the related concept *phase congruency*, [Kov99, Kov08, FS00], and compare the phase congruency based edge detection to our method.

The phase congruency PC as proposed in [Kov99] is the modulus of the complex quantity

$$\widetilde{\mathrm{PC}}(b) = \frac{\sum_{j=1}^{N} \langle f, \kappa_{a_j,b} \rangle}{\epsilon + \sum_{j=1}^{N} |\langle f, \kappa_{a_j,b} \rangle|}, \tag{5.15}$$

thus

$$\mathrm{PC}(b) = |\widetilde{\mathrm{PC}}(b)|. \tag{5.16}$$

Here, κ is a complex wavelet and $\{a_j\}_{j=1}^{N}$ a scale sampling. The parameter $\epsilon > 0$ prevents division by zero.

Conceptual comparison of phase congruency and discrete signature We compare discrete signature to phase congruency and begin with a common feature. Both phase congruency and

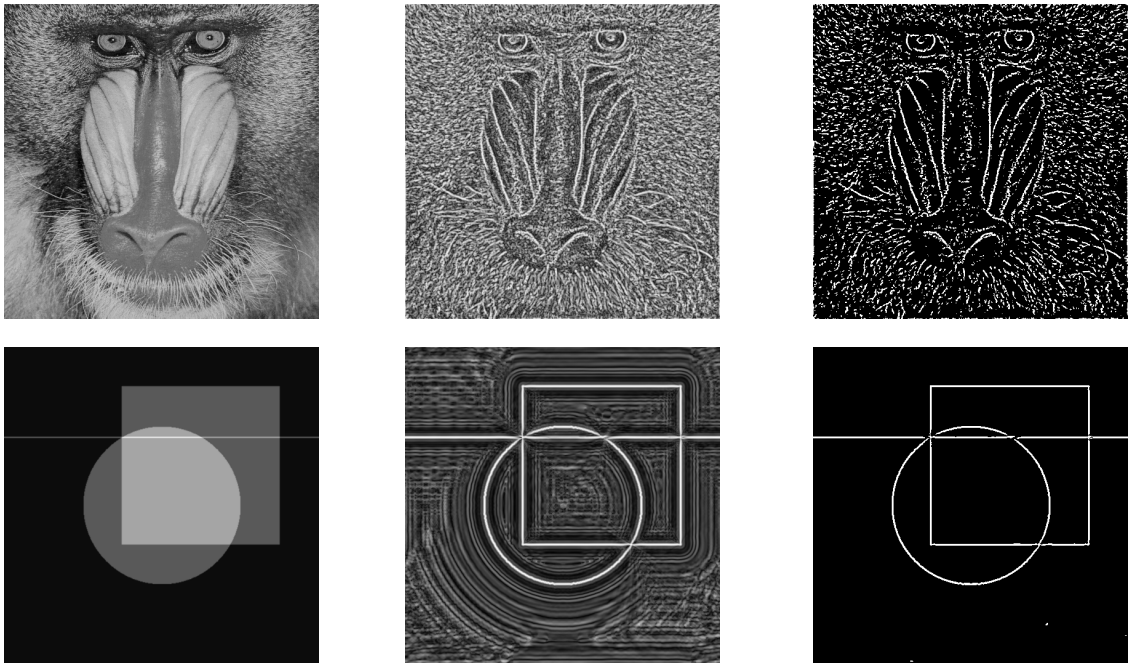

(a) Original **(b)** $|\overline{w}_b|$ **(c)** $|\overline{\sigma}f(b)|$.

Figure 5.6: The discrete isotropic signature for a natural (top row) and a synthetic image (bottom row). (b) We nicely see that the absolute value of the resultant vector $|\overline{w}_b|$ is large at the pronounced edges (e.g. face contours of the monkey, boundaries of the geometric figures) and also responds to fine details such as the hair of the monkey. (c) Those points where the discrete signature is of modulus one correspond to the edges of the image (threshold $\tau = 0.7$).

the modulus of the discrete signature equal one if all complex wavelet coefficients point into the same direction within the complex plane.

In contrast, if the wavelet coefficients are not aligned then phase congruency and discrete signature differ as follows. We first notice that phase congruency does not involve the signs (or phases) of the wavelet coefficients. In particular, the wavelet coefficients are not normalized before summation. In consequence, phase congruency is small only if the wavelet coefficients are not aligned *and* if they are in the same order of magnitude. If only one single wavelet coefficient $\langle f, \kappa_{a_{j_0},b}\rangle$ is much larger in absolute value than the other coefficients, i.e., if

$$|\langle f, \kappa_{a_{j_0},b}\rangle| \gg |\langle f, \kappa_{a_j,b}\rangle|, \quad \text{for all} j \neq j_0,$$

then phase congruency is close to 1, even though the wavelet coefficients may point into completely different orientations. Since this leads to false positive edges Kovesi [Kov99] tackles this "frequency spread"-issue by a sigmoidal weight function $W_{\gamma,c}$ depending on $\sum_j |\langle f, \kappa_{a_j,b}\rangle|$ and two extra real parameters γ and c. With these heuristics, the phase congruency reads as

$$\mathrm{PC}_W(b) = \frac{\left|\sum_{j=1}^N W_{\gamma,c}(b)\langle f, \kappa_{a_j,b}\rangle\right|}{\epsilon + \sum_{j=1}^N |\langle f, \kappa_{a_j,b}\rangle|}. \tag{5.17}$$

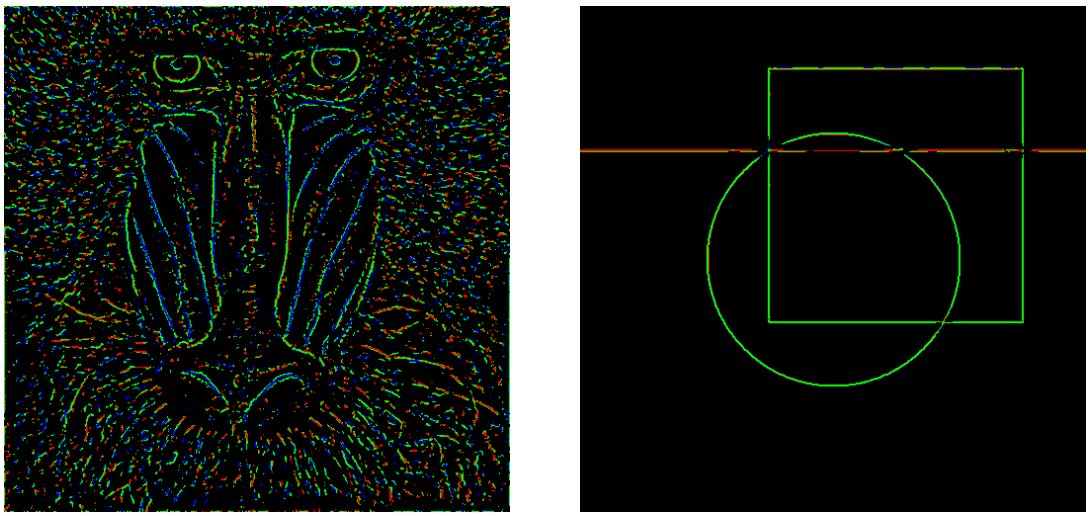

Figure 5.7: The discrete isotropic signature $\overline{\sigma} f$ in a color code. The points b where the imaginary part is in absolute value larger than the real part, i.e. $|\operatorname{Im} \overline{\sigma} f(b)| > \operatorname{Re} \overline{\sigma} f(b)$, have green color. Otherwise, if $\operatorname{Re} \overline{\sigma} f(b) > 0$, the color is red, and if $\operatorname{Re} \overline{\sigma} f(b) < 0$ the color is blue. The points of the image whose discrete isotropic signature is equal to 0 remain black. We observe that the green color is dominant at step edges (boundaries of circle and square in the synthetic image). Bright lines on dark ground corresponds to red color (see horizontal line in synthetic image), dark lines on bright ground to blue color (see lines in the face of the monkey). We emphasize that no noise suppression and no post-processing, such as non-maximum suppression, were required. The left picture was created using a threshold τ of 0.7 and the right one using a slightly higher threshold of 0.8.

All in all, the phase congruency proposed in [Kov99] involves three empirical parameters. In contrast, the discrete signature measures the variation of the wavelet signs. In particular, the normalization is carried out *before* summation. This way every wavelet coefficient is weighted equally, hence we do not need any further heuristics for the handling of dominant wavelet coefficients. The comparison of phase congruency and discrete signature is tabulated in Table 5.2.

Comparison of edge detection by phase congruency and by discrete signature Before comparing the edge detection results of phase congruency and discrete signature, we first look at further differences which arise in two dimensions. The two dimensional phase congruency method of Kovesi [Kov99] uses directional log-Gabor wavelets based on the partial Hilbert transform. The different orientations are combined by simple summation. The analogous method of Felsberg [FS00] utilizes monogenic wavelets based on isotropic difference of Gaussian wavelets. Discrete signature is based on monogenic wavelets based on isotropic Meyer-type wavelets.

We eventually compare the edge detection capabilities of the discrete signature and the phase congruency. The test images are displayed in Figure 5.9. In Figure 5.10, we compare the raw output of the edge detectors and in Figure 5.11, the thresholded images. In all images, white corresponds to 1 and black to 0. We here give a short summary of the results, for a detailed description of the experiments we refer to the captions of the figures. First note that it is in general difficult to objectively compare the performance of edge detectors because there is no ground truth for edges of natural images. Thus the following conclusions are based on the authors

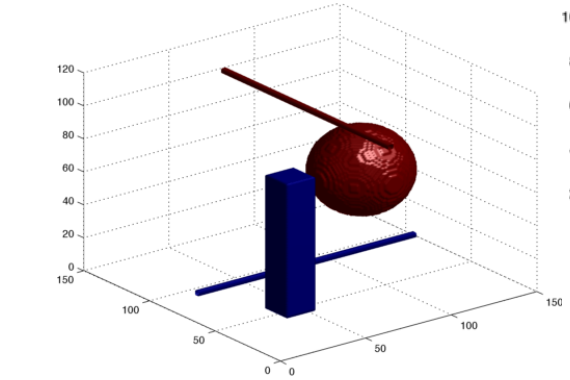

(a) Function f on a synthetic volume. f is equal to -1 on the blue objects, equal to 1 on the red objects, and 0 elsewhere.

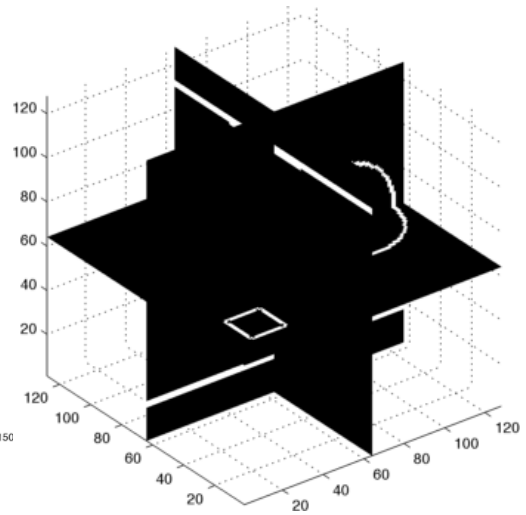

(b) $|\overline{w}_b| > \tau = 0.7$.

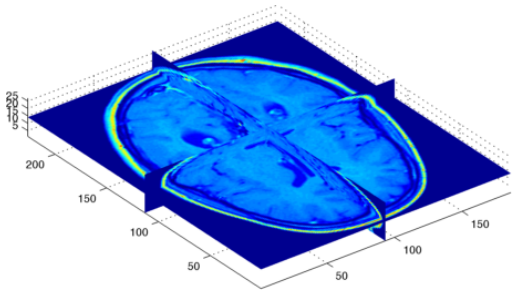

(c) MRI-image of a brain.

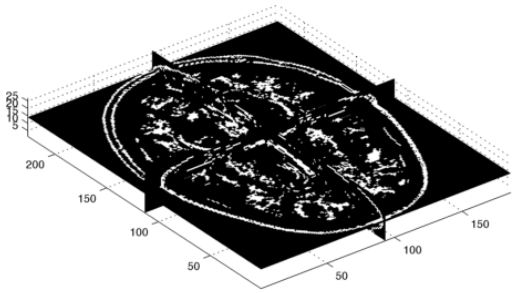

(d) $|\overline{w}_b| > \tau = 0.7$.

Figure 5.8: Edge detection by the discrete isotropic signature in 3D of a synthetic image (a) and a tomographic image (c). We see that all the edges of the synthetic volume are detected (b). Also in the MRI-image (c), most of the expected edges are detected, e.g., the skull bone (d).

subjective impressions. We may observe the following differences. Kovesi's method shows best performance at the overlaying edges of the x-ray image, which is due to the directional filters. The discrete signature has higher response to small details than Kovesi's phase congruency. Felsberg's method on the other hand overemphasizes fine details. The discrete signature appears to have the best balance between the detection of pronounced edges and fine details. This can be seen for example in the results of "Barbara" and "Mandrill".

To summarize, our discrete signature on the one hand has competitive edge detection capabilities to phase congruency, and on the other hand, does not require heuristics or extra parameters as phase congruency does.

	Phase congruency	Discrete signature
Salient point	Low variation of wavelet signs or presence of a dominant wavelet coefficient	Low variation of wavelet signs
Regular point	High variation of wavelet signs and amplitudes of same order of magnitude	High variation of wavelet signs

Table 5.2: Comparison of phase congruency and discrete signature. The presence of a (in absolute value) dominant wavelet coefficient leads to false positives in the edge detection process by phase congruency ("frequency spread"). In contrast, that issue does not occur for the discrete signature because all wavelet coefficients are weighted equally.

5.5 Further references

The importance of the Fourier coefficients' signs in images has been described in the work of Oppenheim and Lim [OL81]. They observed that the important structures of images can be reconstructed by the signs of the Fourier coefficients without the knowledge of their moduli. The reconstruction of images from the wavelet signs appears in the context of 1-bit quantization of wavelet coefficients, see e.g. [Lee96].

It has been indicated by Kronland-Martinet, Morlet, and Grossmann [KMMG87] that the wavelet signs may be useful for the analysis of singularities. They observed that the lines of constant phase in the scalogram $(a, b) \mapsto \langle f, \theta_{a,b} \rangle$ converge towards the singularities as $a \to 0$, where θ is a complex Gaussian wavelet. However, to the authors knowledge, these observations were not realized in a numerical method.

Phase congruency was first introduced by Morrone and Owens [MO87] as descriptor of feature points in signals and images. It was originally proposed as a measure of how much the Fourier coefficients of a signal are in phase. Since a Fourier expansion is poorly localized, Kovesi [Kov99] refined this idea using complex log-Gabor wavelets which found applications to edge detection.

It was observed by Holschneider [Hol95] that the phase of the wavelet coefficients at fine scale describe the local shape of a signal. Kovesi [Kov99] uses the orientation of the phase congruency in the complex plane to distinguish between step and cusp singularities.

A deeper mathematical treatment of signal analysis based on complex wavelet signs will be given by the author in a forthcoming work with collaborators [DMS12]. There we derive the discrete signature as discretization of a continuous model without using directional statistics.

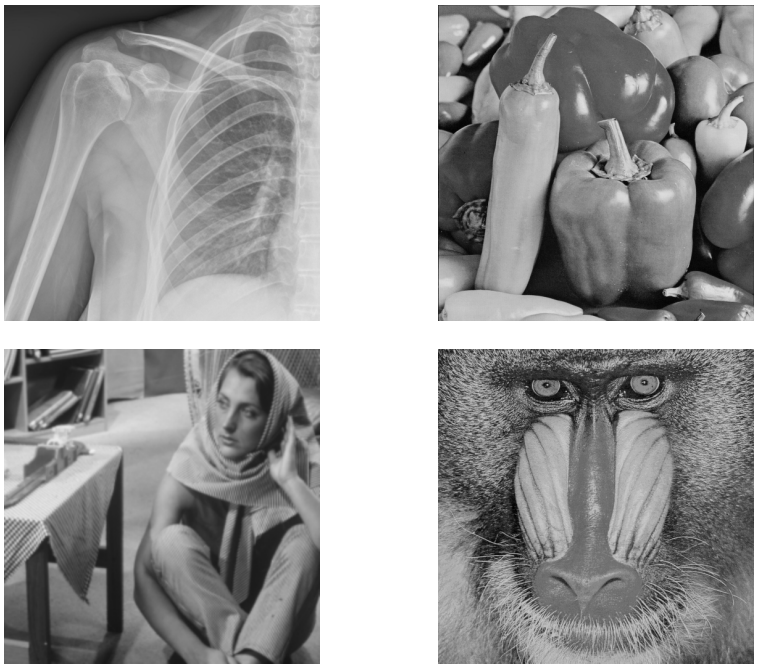

Figure 5.9: Original test images used for the experiments in Figure 5.10 and Figure 5.11; in clockwise order, X-ray, Peppers, Mandrill, and Barbara.

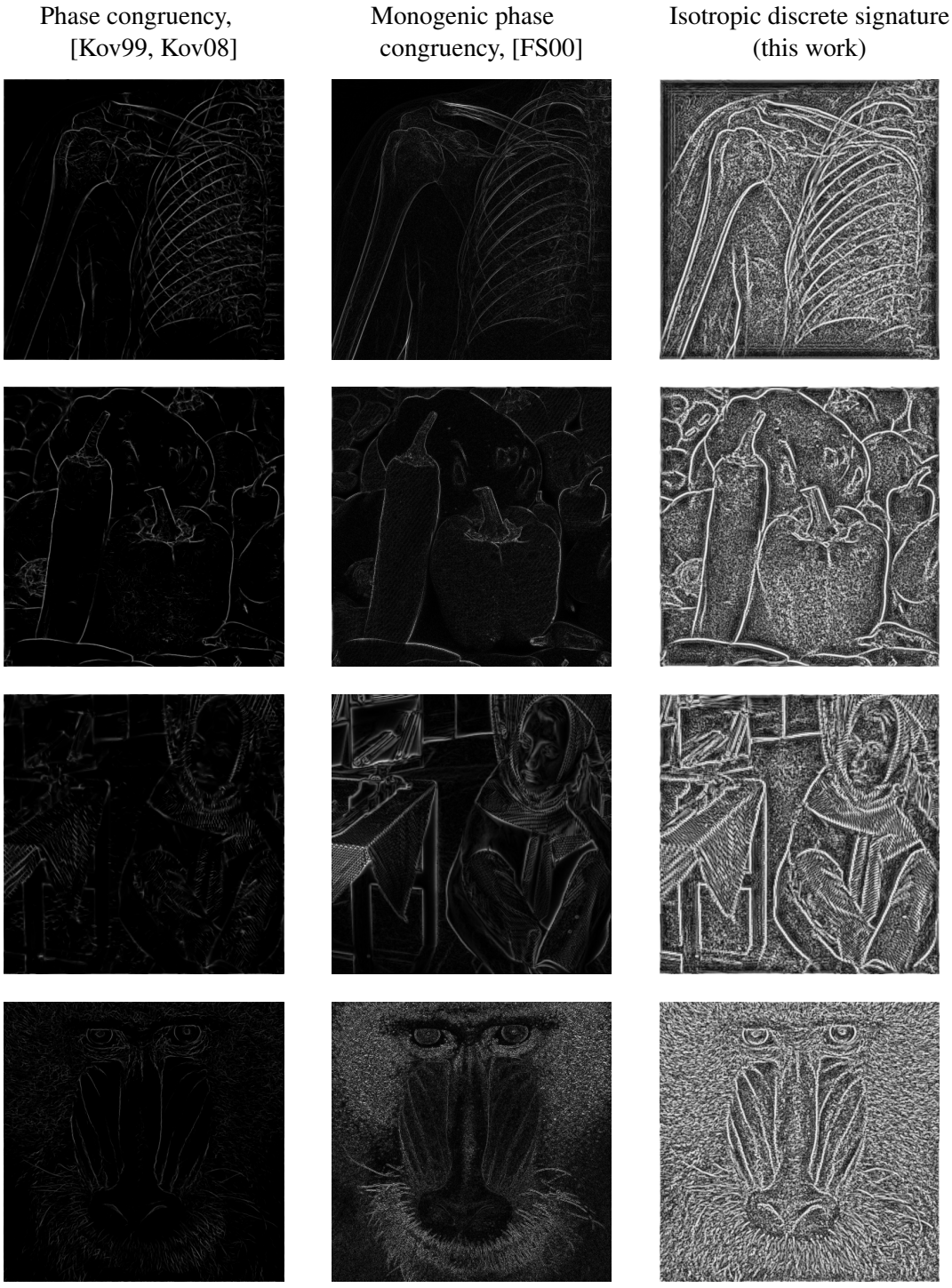

Figure 5.10: The phase congruency (first column) has high response to the most pronounced edges, but also misses several structures, e.g., in the face of the monkey. The monogenic phase congruency gives a high output at high frequency details, e.g., the hair of the monkey, but does not sufficiently emphasize some very pronounced edges such as the legs of the woman. The discrete signature responds well to both low and high-frequency patterns. For instance at the monkey's face contours are nicely detected, as well as the single hairs.

Figure 5.11: Comparison of phase congruency based edge detectors versus the our sign-based edge detector. The phase congruency (left column) detects the most pronounced edges and has good performance at the overlaying edges of the x-ray image, due to the directional filters. The monogenic phase congruency (central column) highly responds to fine details, such as the clothes of the woman. The edge detection by the discrete isotropic signature (right column) appears to give the best balance between the most important edges, e.g., the shape of the woman, and the fine details, such as the face of the woman.

Chapter 6

Amplitude and sign decompositions in mammalian vision and the simulation of brightness illusions

We now set the findings about amplitude and sign decompositions in connection with the perception of brightness illusions. A brightness illusion is a type of optical illusion where our perception of brightness partially fails. The classical explanation states that filter operations on a retinal level are the reason for this phenomenon [Bau60]. However, that theory had been doubted and has recently been disproved by a simple counterexample [GBHS08]. Currently, it is conjectured that brightness illusions originate in so called simple cells [SC05]. Simple cells are neurons in the visual cortex which act on an observed scene as oriented wavelets, cf. [HW59, DVAT82, Dau85, Lee96, Pal99]. The insight about the oriented wavelet nature of the simple cells gives rise to computational simulations of the perception process, and there have been several attempts to reproduce the brightness illusions. The common approach is to expand an image into wavelet coefficients and to reconstruct from suitably manipulated coefficients [MM99, BM99, OVAP08, HSMF10]. Although this leads in many cases to successful reproductions of brightness illusions, the choice of the particular wavelet model and/or the purpose of the manipulations of the wavelet coefficients for the visual system have not been justified sufficiently.

In this work, we simulate brightness illusions using the complex Gabor wavelet model for simple cells, established by Daugman and Lee in [Dau85, Dau88, Lee96]. We exploit that the complex wavelet coefficients are represented within the visual cortex by a quadruple of simple cells and that this induces a natural split into amplitude and sign (Section 6.2). The signs are coded in the activation of a simple cell component, the amplitudes of the coefficients are transmitted by the neuronal firing rates [Lee96, Pal99]. In Section 6.3, we argue that the unary representation of the amplitudes in terms of neuronal discharges causes a quantization of the wavelet amplitudes to a small discrete set of positive numbers. We derive a suitable function which models this quantization and simulate reconstructions from quantified coefficients. We shall see that our model yields a very good reconstruction quality for natural images, but that it causes visible distortions if applied to brightness illusions. These distortions coincide qualitatively and quantitatively with the illusory effects perceived by the human observer. In our experiments we accurately reproduce the illusory effects of many classical brightness illusions like the Hermann grid and a series of its variants, the Mach bands, the White illusion, and the Chevreul illusion. In particular, our model correctly reproduces the vanishing illusory effect of the counterexample to the classical retinal theory given in [GBHS08]. In contrast to related simulations of brightness illusions, we in detail justify the purpose and the implementability of our model within the visual system.

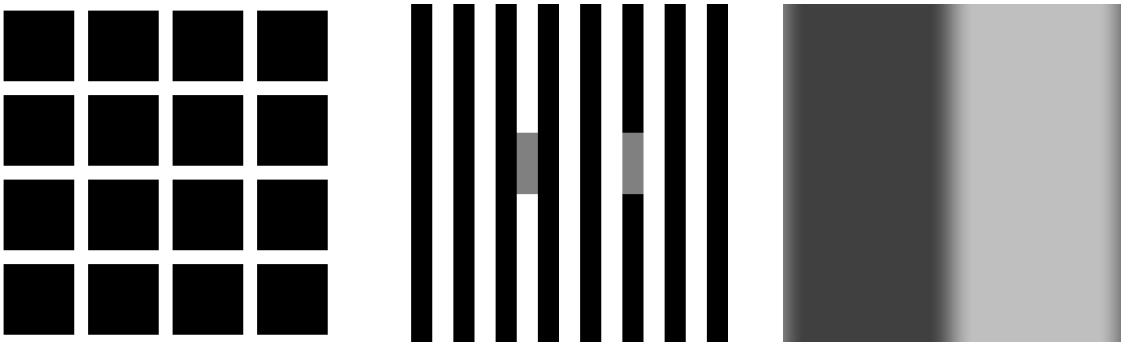

(a) The Hermann grid. **(b)** The White illusion. **(c)** The Mach bands.

Figure 6.1: Some famous brightness illusions: (a) Illusory gray circles are seen at the crossings, (b) The right gray patch appears brighter that the left one, though they have equal gray values, (c) Illusory stripes are seen at the left and the right of the slope.

6.1 The Daugman-Lee model of Gabor wavelet expansion in the visual cortex

In their pioneering work, Hubel and Wiesel discovered that the visual cortex of the mammalians possesses neuronal structures acting as oriented linear filters, called *simple cells;* see e.g. [HW59, Pal99]. In the visual cortex, there is a large set of simple cells, which are tuned to different orientations and spatial frequencies, cf. [DVAT82] and Figure 6.2. Daugman [Dau85] found that the impulse responses of simple cells can be modeled by a family of Gabor wavelets. Lee [Lee96] derived concrete model parameters for these Gabor wavelets and proposed the following wavelet family. The complex-valued *Gabor mother wavelet* $\psi_{1,0,0}$ is defined in the frequency domain by

$$\hat{\psi}_{1,0,0}(\xi_1,\xi_2) = \sqrt{8\pi}\left(e^{-\frac{1}{2}((\xi_1-\kappa)^2+4\xi_2^2)} - e^{-\frac{1}{2}(\xi_1^2+4\xi_2^2+\kappa^2)}\right) \tag{6.1}$$

where $\kappa = \sqrt{2\ln 2}\left(\frac{2^\omega+1}{2^\omega-1}\right)$ and $\omega > 0$ denotes the bandwidth of the function in octaves. The Gabor wavelet family, defined by

$$\psi_{a,b,\theta}(x) = \frac{1}{a}(\rho_\theta\psi_{1,0,0})\left(\frac{x-b}{a}\right), \qquad a \in \mathbb{R}^+, b \in \mathbb{R}^2, \theta \in [0, 2\pi), \tag{6.2}$$

constitutes a wavelet frame[1] for appropriate discretizations of the scale a, the location b, and the orientation θ, cf. [Lee96]. In [Lee96], the author establishes the following biologically motivated conditions on the discretization:

- About 16 to 20 orientations are sampled.
- The human visual system has a spatial frequency range of 3 to 5 octaves.
- The sampling interval of the scale parameter a amounts to $\frac{1}{2}$ octaves in the cat's and to $\frac{1}{3}$ in the monkey's visual cortex.

[1] To avoid possible confusions of the terminology, we notice that the function system (6.2) is a wavelet frame (of Gabor wavelets), but not a Gabor frame. The latter would employ modulations instead of dilations, cf. [Chr03].

- The bandwidth ω of the simple cells ranges from 0.5 to 2.5 octaves and clusters around 1.2 and 1.5 octaves.

Based on these assumptions, the following parameter set was proposed in [Lee96], which we will use throughout this chapter. The bandwidth is set to $\omega = 1.5$ octaves. The scale parameter a is sampled at five octaves and three voices per octave, i.e., $a_j = 2^{-j/3}$, where $j = 1, ..., 15$. The spatial parameter b is sampled at an integer grid, i.e., $k \in \mathbb{Z}^2$. Further, we expand into the sixteen orientations $\theta = \frac{\pi l}{16}$, where $l = 0, ..., 15$. To summarize, we deal with the discrete Gabor wavelet family

$$\psi_{j,k,l}(x) = 2^{j/3}(\rho_{\frac{\pi l}{16}}\psi_{1,0,0})(2^{j/3}(x-k)). \tag{6.3}$$

The scale and orientation sampling of the Gabor wavelet system leads to a nearly tight frame [Lee96]. That is, the lower frame constant, denoted by A, is close to the upper frame constant, denoted by B; compare Definition 3.12. The modeling of the simple cells by the family of Gabor wavelets (6.3) is referred in the following as *Daugman-Lee model.*

Now let us combine the low frequency Gabor functions into a lowpass filter ϕ_k, i.e.,

$$\phi_k = \sum_{l=0}^{15} \sum_{j=0}^{-\infty} \psi_{j,k,l}.$$

According to [Lee96], the Gabor wavelet family has an approximate reproducing formula, i.e.,

$$f \approx \frac{2}{A+B} \sum_{k\in\mathbb{Z}^2} \sum_{j=1}^{15} \sum_{l=0}^{15} \langle f, \psi_{j,k,l}\rangle \psi_{j,k,l} + \langle f, \phi_k\rangle \phi_k, \tag{6.4}$$

compare [Lee96]. In the numerical experiment Figure 6.6(b), we may verify that formula (6.4) indeed gives a good approximate reconstructions.

Let us create the link of the Daugman-Lee model to complex wavelets. From formula (6.1) we see that the Fourier spectrum of the mother Gabor wavelet $\psi_{1,0,0}$ lies essentially in the half-space $\xi_1 > 0$. Therefore, we have the approximate quadrature relationship

$$\operatorname{Im}\psi_{1,0,0} \approx \mathcal{H}_{(1,0)} \operatorname{Re}\psi_{1,0,0},$$

so the Gabor wavelet can be seen as an approximate complex wavelet in the sense of the partial Hilbert transform, compare Lemma 2.19 and also [Mal09, p. 111ff].

6.2 Amplitude and sign representation of Gabor coefficients by simple cells

We have just seen that simple cells can be modeled by complex Gabor wavelets. We now explain how the complex wavelet coefficients are realized on a neuronal level, where we follow mainly the articles [Dau85, Lee96] and the textbook [Pal99]. We shall see that the simple cell representation of the wavelet coefficients induces a natural amplitude and sign decomposition.

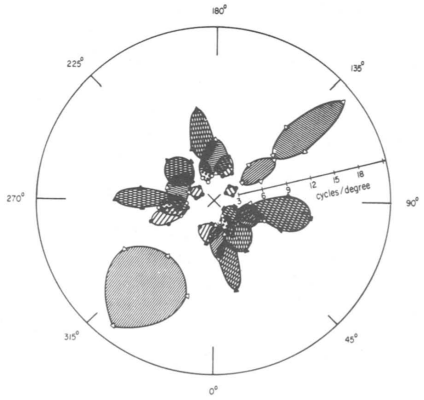

Figure 6.2: Frequency responses of several simple cells in the macaque visual cortex (picture taken from [DVAT82]). The gray shaded regions each depict the support of the frequency spectrum of a simple cell. We see that the simple cells are tuned to different scales and orientations. Daugman [Dau85] and Lee [Lee96] model the impulse response of simple cells by a family of Gabor wavelets.

Natural amplitude and sign decomposition by simple cells In the visual cortex, a complex Gabor coefficient is represented by a quadruple of simple cells, corresponding to the positive and the negative parts of the real and imaginary component, respectively. This split representation is very natural because neurons transmit information by series of subsequent discharges *(firing rates),* which are positive quantities [Lee96, Pal99]. The decomposition of the complex Gabor coefficients is reflected by the following four types of simple cells in the visual cortex. There are

- light line detectors, denoted by L^+,
- dark line detectors, denoted by L^-,
- dark-to-light step edge detectors, denoted by E^+,
- and light-to-dark step edge detectors, denoted by E^-,

which are approximately proportional to the positive and the negative parts of the real and the imaginary component of the wavelet coefficients of the Daugman-Lee model, respectively (cf. [Lee96] and [Pal99, p. 151]). In mathematical terms, a simple cell tuned to some frequency-space-orientation index $\mu = (j, k, l)$ is a non-negative functional, acting on an observed scene f approximately as evaluation versus a Gabor wavelet, i.e.,

$$\begin{aligned} L^+_\mu f &\approx (\mathrm{Re}\langle \psi_\mu, f\rangle)_+, \\ L^-_\mu f &\approx (\mathrm{Re}\langle \psi_\mu, f\rangle)_-, \\ E^+_\mu f &\approx (\mathrm{Im}\langle \psi_\mu, f\rangle)_+, \\ E^-_\mu f &\approx (\mathrm{Im}\langle \psi_\mu, f\rangle)_-, \end{aligned} \tag{6.5}$$

where

$$(x)_+ = \begin{cases} x, & \text{for } x > 0, \\ 0, & \text{else,} \end{cases} \qquad \text{and} \qquad (x)_- = \begin{cases} x, & \text{for } x < 0, \\ 0, & \text{else.} \end{cases}$$

The activation of the (+) and the (−) cells is exclusive; that is, if for a fixed index μ the (+) cell is active, then the corresponding (−) cell is inactive. For example, a wavelet coefficient $w_\mu = 0.6 - i\,0.2$ corresponds to the activation of L_μ^+ and E_μ^- and the deactivation of L_μ^- and E_μ^+. To summarize, the Gabor coefficient representation by simple cells is expressed by

$$\begin{aligned}\langle f, \psi_\mu \rangle &= (\mathrm{Re}\langle \psi_\mu, f\rangle)_+ - (\mathrm{Re}\langle \psi_\mu, f\rangle)_- + i\,[(\mathrm{Im}\langle \psi_\mu, f\rangle)_+ - (\mathrm{Im}\langle \psi_\mu, f\rangle)_-] \\ &\approx L_\mu^+ f - L_\mu^- f + i\,[E_\mu^+ f - E_\mu^- f], \end{aligned} \tag{6.6}$$

where at most two of the four summands are non-zero.

Now let us build the bridge to the amplitude and sign decompositions. Recall that the Gabor wavelets are complex wavelets in the sense of the partial Hilbert transform. The split of the complex wavelet coefficients into the four channels can be interpreted as an amplitude and sign decomposition. However, the amplitude and sign split of the Gabor coefficients by (6.6) is slightly different than in the decompositions considered in the previous chapters. The representation of the wavelet coefficients by the four cell types $L_\mu^+ f$, $L_\mu^- f$, $E_\mu^+ f$, and $E_\mu^- f$ yields a separate decomposition of the real and the imaginary part into amplitude and (real-valued) sign, i.e., we have one amplitude and sign decomposition for the real part and one for the imaginary part. Hereby, the amplitude is transmitted by the firing rate of a simple cell and the sign is implicitly transmitted by the activeness of the (+) or the (−) cell.

The importance of the sign information In the Oppenheim-Lim type experiments in Section 5.1, we have seen that the signs of the complex wavelet coefficients codes the most significant information about the image structure. We here deal with a slightly different notion of sign than in Chapter 5 but we will see in the next experiment that the sign, induced by the split representation of the simple cells, still carries the significant part of the image's structural information. To this end, we expand an image into the Gabor wavelet system (6.3). We set the modulus of the real part of the wavelet coefficients to one, if they exceed some threshold $\tau > 0$; smaller coefficients are set to 0. We deal likewise with the imaginary part and reconstruct from these thresholded sign coefficients using formula (6.4), omitting the lowpass component. For the precise formulation of this procedure, we introduce the thresholded sign function $\mathrm{sgn}_\tau : \mathbb{R} \to \{-1, 0, 1\}$ defined by

$$\mathrm{sgn}_\tau(w) := \begin{cases} \mathrm{sgn}\ w, & \text{if } |w| > \tau, \\ 0, & \text{else.} \end{cases}$$

The *sign reconstruction formula* then reads as

$$\frac{2}{A+B} \sum_{j,k,l} [\mathrm{sgn}_\tau(\mathrm{Re}(w_{j,k,l}) + i\ \mathrm{sgn}_\tau(\mathrm{Im}(w_{j,k,l})]\, \psi_{j,k,l} \tag{6.7}$$

where $w_{j,k,l} = \langle f, \psi_{j,k,l} \rangle$. The action of the sign reconstruction (6.7) to a natural image is depicted in Figure 6.3. We observe the image structure is nearly completely preserved by the sign reconstruction, even small details remain visible.

The sign reconstruction experiments may suggest that the wavelet signs are sufficient for an almost complete representation of the images structure, and this is in fact the case for many natural images. However, there are images where the reconstruction from the wavelet signs is not that good. The next experiment (Figure 6.4) shows that the sign reconstruction (6.7) causes severe distortions if applied to brightness illusions such as the the Hermann grid. Hence for these images, the amplitude information does have a great influence on the reconstruction quality.

(a) Image f with unbalanced brightness

(b) Sign reconstruction by (6.7), $\tau = 0$

(c) Sign reconstruction by (6.7), $\tau = 0.01$

(d) Sign reconstruction by (6.7), $\tau = 0.02$

Figure 6.3: The reconstruction from the sign of the Gabor coefficients according to (6.7) for different threshold values τ. We see that nearly all of the structural information is kept. Even more, the originally unbalanced brightness is balanced in the reconstructions. Note that the details are very well preserved, even in the originally dark area. For $\tau = 0$, the image appears very noisy (b), but already for small positive values of τ, the noise disappears in the reconstructions (c – d).

6.3 An amplitude quantization model for the simulation of brightness illusions

We have just seen that we can achieve good reconstructions of natural images from the sign information induced by the simple cell representation. In contrast, we have noted that this procedure fails when applied to brightness illusions. We further observe in Figure 6.4 that the missing amplitude information leads to reconstruction errors which qualitatively resemble the illusory effects of brightness illusions. This gives rise to the hypothesis that an imperfect amplitude processing of the wavelet coefficients on a simple cell level is the reason for the brightness illusions.

In the following, we derive an extension of the Daugman-Lee model which takes into account quantizations of the Gabor wavelet coefficients on a simple cell level. In particular, we express the approximate relations of (6.5) by a concrete quantization function. We shall see in a series of experiments that our model reproduces many brightness illusions.

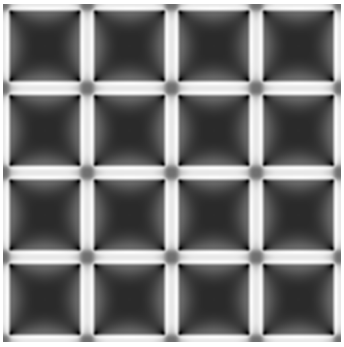

(a) Sign reconstruction (6.7), $\tau = 0.02$

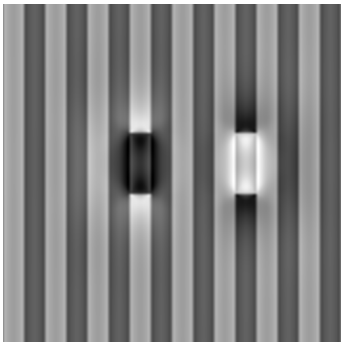

(b) Sign reconstruction (6.7), $\tau = 0.02$

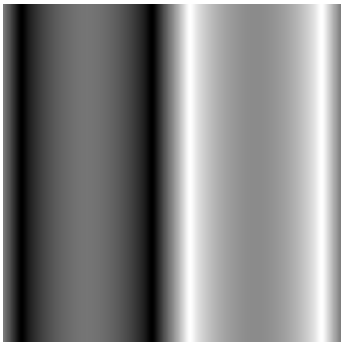

(c) Sign reconstruction (6.7), $\tau = 0.02$

Figure 6.4: The reconstruction from the sign of the Gabor coefficients according to (6.7) for the brightness illusions of Figure 6.1. The threshold parameter was chosen to be $\tau = 0.02$. We see that the errors in the reconstructed images qualitatively resemble the illusory effects of the brightness illusions. However, note that the reconstruction errors are much stronger than the illusory effect perceived by a human observer.

Basic assumptions We model the amplitude processing in simple cells based on the following three assumptions. First, we assume that a simple cell is active ("fires") if and only if its corresponding model Gabor coefficient exceeds in modulus some lower threshold $\tau > 0$. Second, we assume that the magnitude of a Gabor coefficient is transmitted in an unary representation by the firing rate of the simple cell. Here, the number of discharges of a simple cell is approximately proportional to the magnitude of the wavelet coefficient. At last, we assume that the number of discharges per observed scene has the upper limit $F_{\max} \in \mathbb{N}$.

Let us comment on the plausibility of these assumptions. The first assumption derives from a general property of neurons. A neuron discharges if its action potential exceeds some lower threshold, cf. [BCP07, Ch. 4]. The assumption of a unary representation (base-1 representation) of the amplitude by the firing rates can be justified as follows. In a unary (base-1) representation, the weight of a single digit does not depend on its position within the representation, as opposed to a binary (base-2) representation. In particular, coding and decoding in unary representations does not require a discrimination between the positions in a sequence of digits. The plausibility of the third assumption, that is the existence of an upper limit for the firing rates $F_{\max}$, is evident. However, we require a reasonable order of magnitude for $F_{\max}$, which we derive as follows. We have seen in the last section that the reconstructions might be severely distorted if the coefficients are coded by only one bit (which corresponds to the sign reconstruction). Clearly, an extension of the code space results in a better reconstruction quality. On the other hand, each additional element in the code space is at the cost of extra neuronal discharges, which consumes extra energy. Hence, the maximal firing rate per scene is a tradeoff between reconstruction quality and energy consumption. To derive a reasonable value, we use the fact that several works report a firing rate of up to about 100 Hz for simple cells, e.g., [CHM97, SFV76, SBS+87]. In [SSM05], the sampling rate of scenes by a human observer is found to be about 16 Hz. This suggests the choice $F_{\max} = \left[\frac{100}{16}\right] = 6$, where the square brackets denote the rounding operation. The quantity we derived here has to be understood more as an order of magnitude than as a precise parameter. We note that the outcome of the experiments is not altered significantly for other choices of the parameter $F_{\max}$, as long as we keep the order of magnitude. For example, a choice of $F_{\max}$

between 5 and 10 leads to almost identical results. The determination of exact parameters would require physiological experiments, which cannot be obtained in this work. We will comment in the next paragraph on the choice of the threshold τ.

A model of amplitude quantization With the assumptions of the previous paragraph, we model the relation between the Gabor coefficients and the discharges of the simple cells indicated in (6.5) by the quantifying function

$$F(u) := \begin{cases} 0, & \text{if } 0 \le u < \tau, \\ 1, & \text{if } \tau \le u < \frac{1}{F_{\max}} u_{\max}, \\ 2, & \text{if } \frac{1}{F_{\max}} u_{\max} \le u < \frac{2}{F_{\max}} u_{\max}, \\ 3, & \text{if } \frac{2}{F_{\max}} u_{\max} \le u < \frac{3}{F_{\max}} u_{\max}, \\ & \vdots \\ F_{\max}, & \text{if } \frac{F_{\max}-1}{F_{\max}} u_{\max} \le u. \end{cases} \tag{6.8}$$

Here, $u_{\max}$ denotes the Gabor wavelet magnitude corresponding to the maximum simple cell discharge rate $F_{\max}$. We empirically found that the maximum coefficient amplitude is about $u_{\max} = 1$ for natural images taking values in the range $[0, 1]$. The graph of F is depicted in Figure 6.5. Our model for the simple cell discharges now reads

$$\begin{aligned} L_\mu^+ f &= F[(\mathrm{Re}\langle \psi_\mu, f\rangle)_+], \\ L_\mu^- f &= F[(\mathrm{Re}\langle \psi_\mu, f\rangle)_-], \\ E_\mu^+ f &= F[(\mathrm{Im}\langle \psi_\mu, f\rangle)_+], \\ E_\mu^- f &= F[(\mathrm{Im}\langle \psi_\mu, f\rangle)_-]. \end{aligned} \tag{6.9}$$

For example, the wavelet coefficient $w = 0.6 - 0.2i$ corresponds to $F(0.6) = 4$ subsequent discharges of an L^+ cell and $F(0.2) = 2$ discharges of an E^- cell. Note that in our model (6.9) the simple cell firing rate is not in a perfect proportional relation to the Gabor coefficient.

Our next goal is to look at reconstructions from the quantified wavelet coefficients. To this end, we recompose the four quantified amplitude coefficients to a quantified complex Gabor wavelet coefficient s_μ by

$$s_\mu := \frac{u_{\max}}{F_{\max}} [L_\mu^+ f - L_\mu^- f + i\,(E_\mu^+ f - E_\mu^- f)].$$

(The multiplicative constant $\frac{u_{\max}}{F_{\max}}$ assures that the reconstruction has the same scaling as the original image.) Inserting this into the reproducing formula (6.4) the reconstruction formula of the quantified coefficients reads

$$\frac{2}{A+B} \sum_k \sum_{j,l} s_{j,k,l} \psi_{j,k,l} + \langle f, \phi_k \rangle \phi_k. \tag{6.10}$$

Notice that in this reconstruction formula, the lowpass coefficients $\langle f, \phi_k \rangle$ are assumed to be free from distortions.

We eventually comment on the choice of the threshold parameter τ. We found in our experiments that the magnitude of the threshold influences the reconstruction quality as follows. If τ is

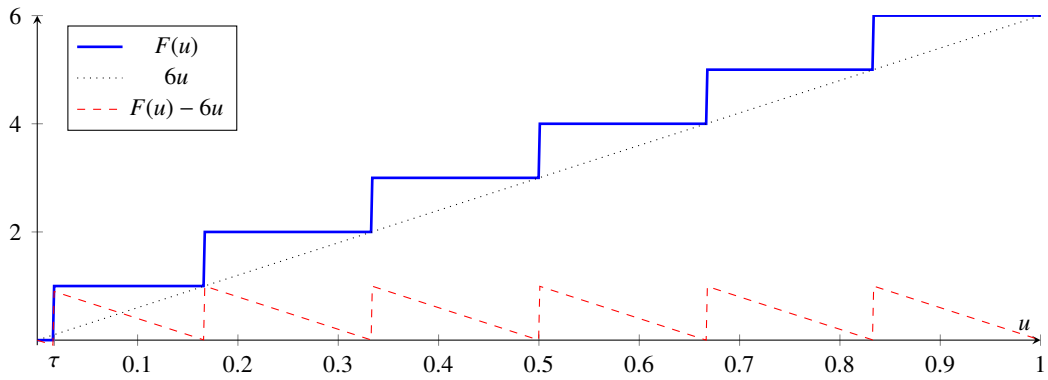

Figure 6.5: The quantification function $F(u)$ for the parameter choice $F_{\max} = 6$, $u_{\max} = 1$, and $\tau = \frac{1}{10} \cdot \frac{u_{\max}}{F_{\max}} \approx 0.017$. The quantified values are almost everywhere higher that the non-quantified values, depicted here as the linear function $u \mapsto \frac{F_{\max}}{u_{\max}} u = 6u$ (dottet line). The function of the quantization error $F(u) - 6u$ is plotted as dashed red line.

chosen too low then a lot of very small coefficients is raised to a higher level, and hence, noise is amplified, cf. Figure 6.3. On the other hand, if τ is large, then small details of the observed scene may be suppressed. We found that the threshold value $\tau = 0.1 \cdot \frac{u_{\max}}{F_{\max}}$ is a fair tradeoff between the suppression of noise and the preservation of details.

Simulation of brightness illusions Before we apply our quantization model (6.10) to brightness illusions we first check its reconstruction quality for natural images. In Figure 6.6 we see that a reconstruction from quantified coefficients preserves both the brightness and the structural information of natural images and that no significant distortions are introduced. In contrast, the following experiments show that the quantified reconstruction leads to an notable error if applied to brightness illusions and that this error coincides surprisingly accurate with the perceived illusory effects.

Let us first look at the Hermann grid illusion, which was already discovered in 1870, see [Her70]. The Hermann grid consists of white vertical and horizontal bars on a black background (Figure 6.1(a)). At the crossings of the bars, illusory gray smudges are perceived. In our first experiment, Figure 6.7, we observe that the reconstruction by our model reproduces the illusory gray circles of the Hermann grid illusion and that the intensity of the simulated effect matches the intensity of the perceived illusory effect.

In a second example, we investigate the sine distorted Hermann grid; see Figure 6.8. As stated in [GBHS08], the illusory effect vanishes for sufficiently high amplitudes of the sine wave. For low amplitudes of the sine, the gray smudges are still existent, but their intensity falls off with increasing amplitude up to almost no effect. In Figure 6.8 we see that this effect is reproduced by the proposed reconstruction model. This variant is of particular importance since it serves as a counterexample to the classical explanation of the illusory effects [GBHS08].

The next three variants were proposed in [SC05]. If the thickness of the white bars increases, then the illusory effect is diminished. In Figure 6.9 we see that the described behavior is accurately simulated by the quantified simple cell model. Further, if diagonals are added, then the illusion almost vanishes which we also can reproduce, see Figure 6.10. At last, we look at shifts

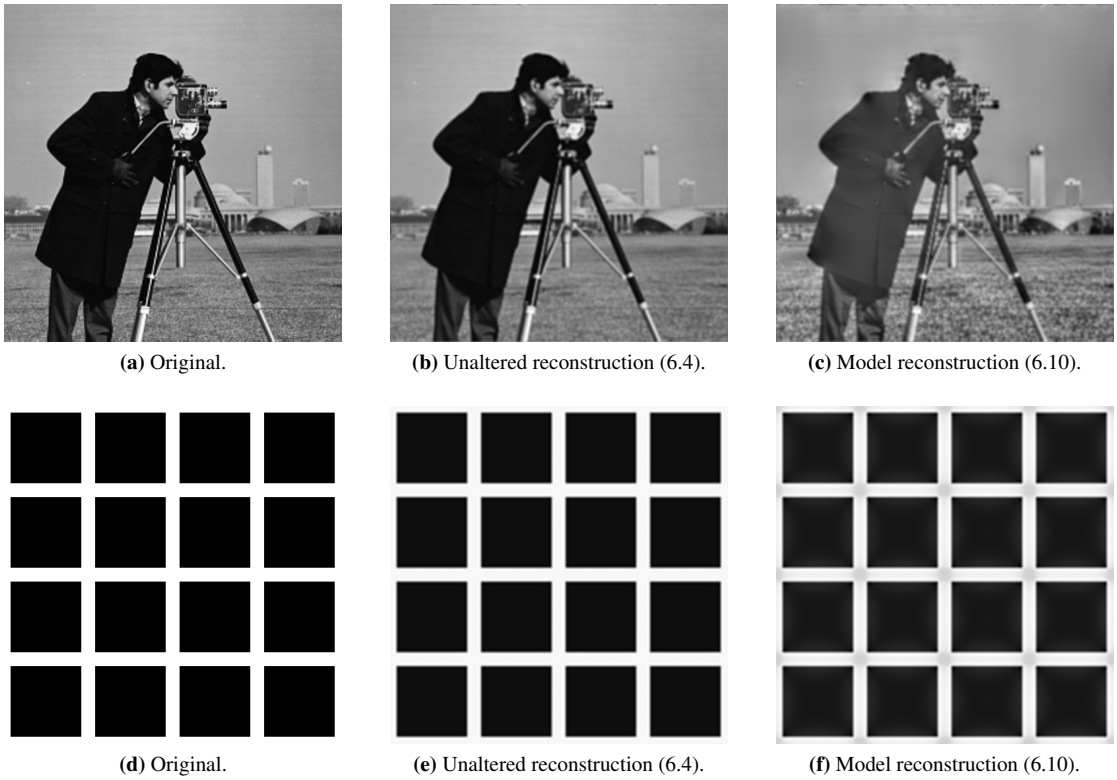

(a) Original. **(b)** Unaltered reconstruction (6.4). **(c)** Model reconstruction (6.10).

(d) Original. **(e)** Unaltered reconstruction (6.4). **(f)** Model reconstruction (6.10).

Figure 6.6: The reconstruction from quantified Gabor coefficients and the reconstruction from perfect coefficients of a natural image and a brightness illusion. (a–c) The reconstruction from perfect coefficients (6.4) is hardly distinguishable from the original. In the reconstruction from the quantified coefficients (6.10) almost all important details are preserved and the reconstruction error is within reasonable bounds. We even recognize the nice side effect that details in low contrast regions, such as the man's jacket, are more pronounced in the reconstruction. This can be explained, because small coefficients, which are just above the threshold τ, are raised by the quantification to the next larger integer value. (d–f) The reconstruction from perfect coefficients yields an almost perfect reconstruction even for brightness illusions. On the other hand, if we assume quantified coefficients according to (6.10), we observe a notable error which coincides with the perceived illusory effect.

of the black squares. Here, the illusory effect decreases already for small shifts but then remains on a constantly low level for larger shifts. This effect is simulated in Figure 6.11.

Apart from the Hermann grid, our model accounts for further classical brightness illusions. Amongst these are the Mach bands (Figure 6.12), the White illusion (Figure 6.13), and the Chevreul illusion (Figure 6.14). An explanation of the effects is given in the captions of the respective figures.

Further remarks on the quantization error Having shown that the reconstruction formula (6.10) reproduces illusory effects of brightness illusions we now try to figure out the reason for this behavior. We notice that the difference of the quantified reconstruction (6.10) to the unaltered

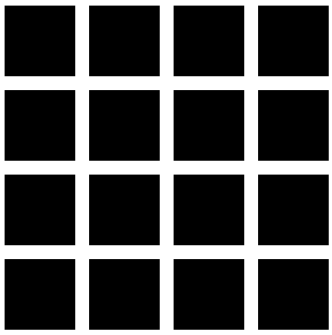

(a) Original.

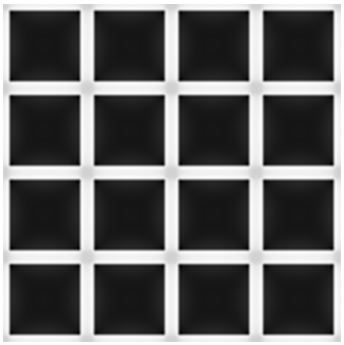

(b) Reconstruction by (6.10).

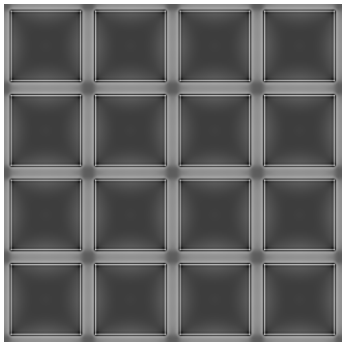

(c) Reconstruction error (gray values rescaled for better visibility, see profile plot (e) for the magnitudes).

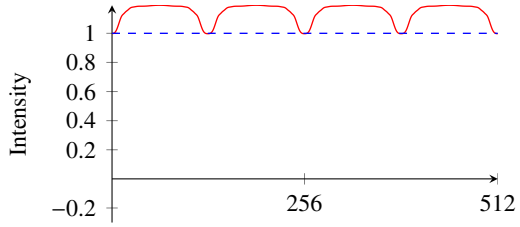

(d) Central horizontal profile of original (a) in blue and reconstruction (b) in red.

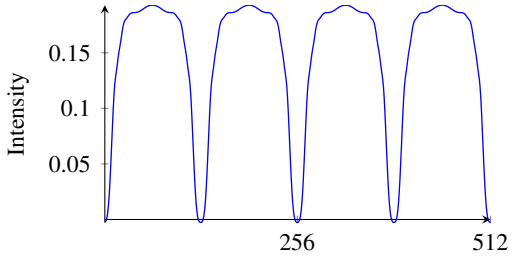

(e) Central profile of error (c).

Figure 6.7: (a) The observer of the Hermann grid sees illusory gray spots at the crossings of the white bars [Her70]. (b–e) The illusory effect can be clearly seen in the reconstruction from the quantified amplitude coefficients.

reconstruction (6.4) is given by

$$\frac{2}{A+B}\sum_{\mu}\left(\frac{u_{\max}}{F_{\max}}s_\mu - \langle f,\psi_\mu\rangle\right)\psi_\mu. \tag{6.11}$$

Thus, the reconstruction error originates from the quantification errors of the coefficients

$$\frac{u_{\max}}{F_{\max}}s_\mu - \langle f,\psi_\mu\rangle = \operatorname{sgn}(x_\mu)\cdot\left(\frac{u_{\max}}{F_{\max}}F(|x_\mu|) - |x_\mu|\right) + i\,\operatorname{sgn}(y_\mu)\cdot\left(\frac{u_{\max}}{F_{\max}}F(|y_\mu|) - |y_\mu|\right).$$

where $x_\mu = \operatorname{Re}\langle f,\psi_\mu\rangle$ and $y_\mu = \operatorname{Im}\langle f,\psi_\mu\rangle$. By the substitution

$$h(u) := \frac{u_{\max}}{F_{\max}}F(u) - u, \quad \text{for } u \geq 0,$$

we can rewrite the quantification error of the coefficients as

$$\frac{u_{\max}}{F_{\max}}s_\mu - w_\mu = \operatorname{sgn}_\tau(x_\mu)\cdot h(|x_\mu|) + i\,\operatorname{sgn}_\tau(y_\mu)\cdot h(|x_\mu|).$$

In this form, we may recognize a similarity to the sign reconstruction formula (6.7). In Figure 6.5 we see that h has the shape of a sawtooth function, taking values between $[0, 1]$, for $u \leq u_{\max}$. If

$h(u)$ were equal to 1 for $u > \tau$, then the reconstruction error (6.11) would amount exactly to the sign reconstruction of (6.7). This connection suggests that the illusory effects are similar to the effects induced by the sign reconstruction (6.7). However, the reason for the sign reconstruction effects are not yet understood and require further investigation.

6.4 Further references

The sign reconstruction formula (6.7) has parallels to the q-bit quantification experiments in [Lee96]. There, it has been observed that a good image reconstruction of natural images can be obtained even if the amplitude of the Gabor coefficients is quantified to a small set of values.

The classical explanation of brightness illusions is based on the filter characteristics of retinal ganglion cells [Bau60]. Recently, it has been shown by a striking counterexample that the illusory effect of the most famous brightness illusion, the Hermann grid, cannot originate on a retinal ganglion cell level [GBHS08].

The currently most favored theory is that brightness illusion originate on a simple cell level. The authors in [SC05] argue on an informal level that the Hermann grid illusion originates in the simple cells but their arguments were not backed by proper simulations. Corney and Lotto [CL07] reproduce the Hermann grid illusion as result of an artificial neuronal network, which was trained to robustly recognize surfaces under non-uniform illumination. The main issue of this approach is that one gets few insight into what has been learned by the neuronal network. In [OVAP08], brightness illusions are reproduced by a normalization of wavelet coefficients of a tensor product wavelet. Although several brightness illusions are simulated, the employed tensor product wavelets are not known to have any connection to the mammalian visual system. In [BM99], several brightness illusions, such as the classical Hermann grid and the white effect, are simulated by scale-wise renormalization of oriented difference of Gaussian (ODoG) filter outputs. The ODoG model is the most related approach to the simulations in this work, since the ODoG filters are similar to the Gabor wavelets. However, in [BM99] the authors manipulate the wavelet coefficients by a computationally expensive renormalization operation whose purpose for the visual system has not been answered satisfactory.

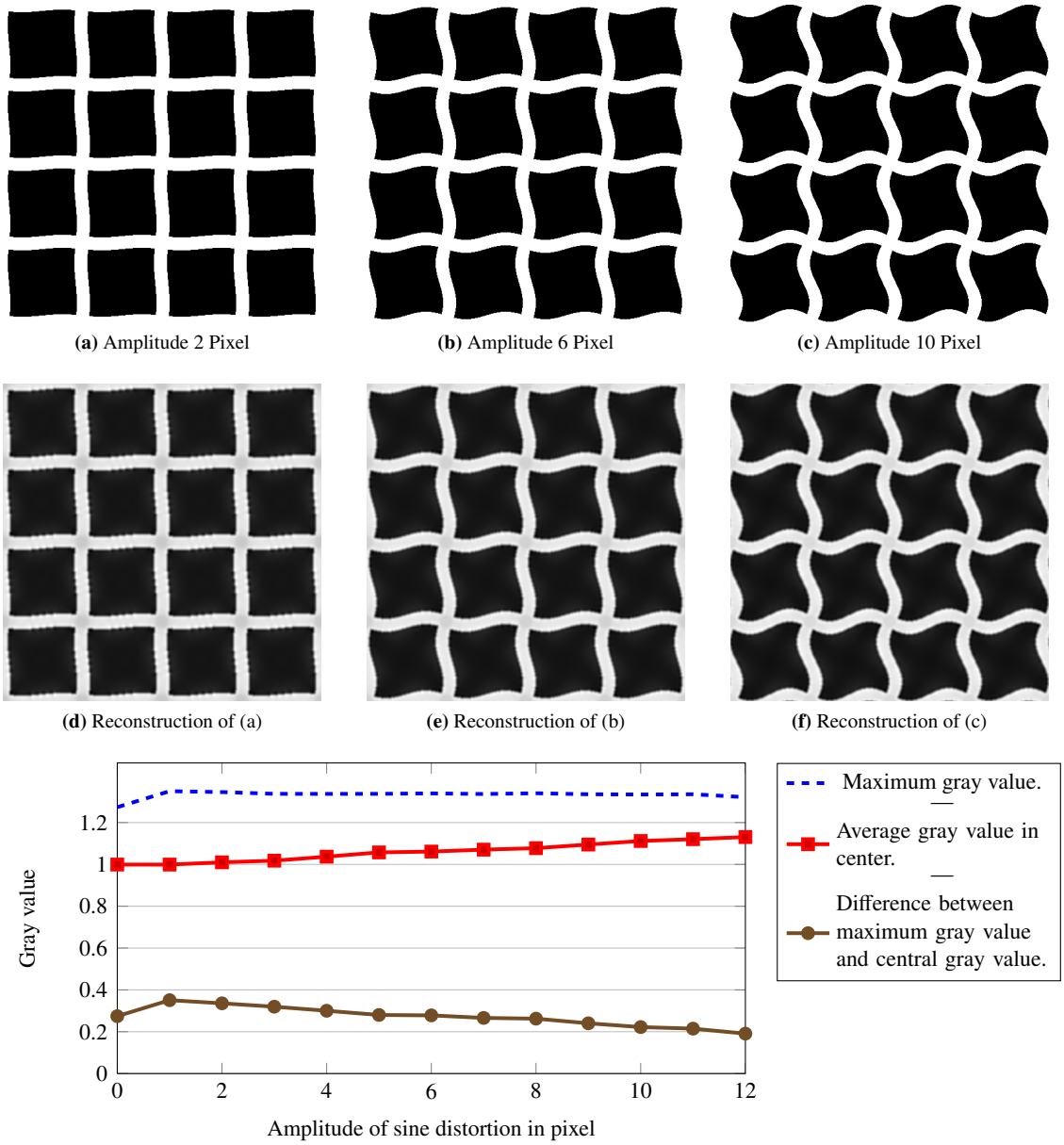

(a) Amplitude 2 Pixel **(b)** Amplitude 6 Pixel **(c)** Amplitude 10 Pixel

(d) Reconstruction of (a) **(e)** Reconstruction of (b) **(f)** Reconstruction of (c)

Figure 6.8: (a – c) The illusory effect decreases with increasing amplitude of the sine distortion. This is the counterexample from [GBHS08] to the classical explanation. (d – f) We observe that the reconstruction by the proposed model (6.10) reproduces the vanishing effect for larger amplitudes. We verify in the plot that the relative brightness in the center indeed decreases (brown line).

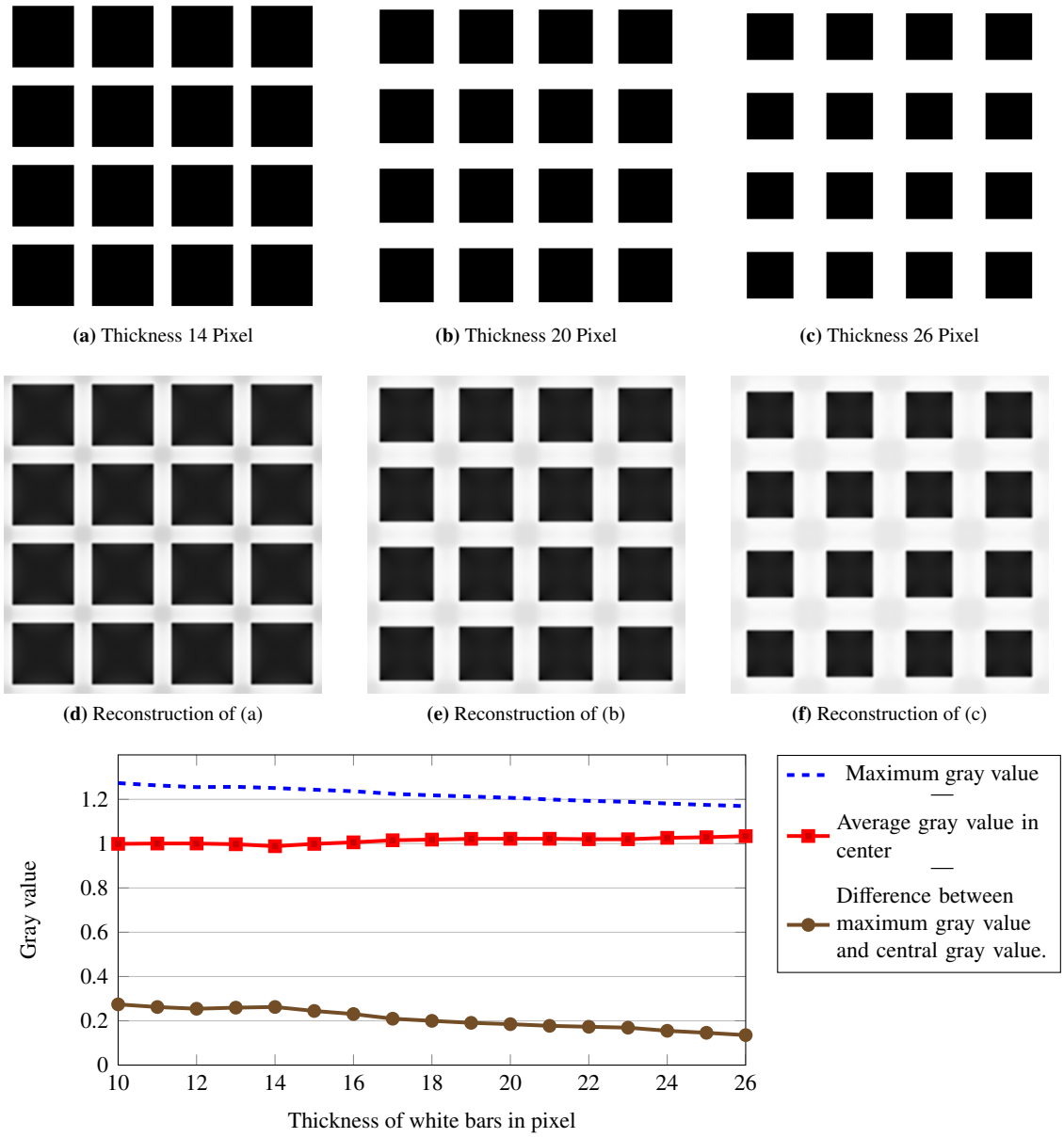

(a) Thickness 14 Pixel **(b)** Thickness 20 Pixel **(c)** Thickness 26 Pixel

(d) Reconstruction of (a) **(e)** Reconstruction of (b) **(f)** Reconstruction of (c)

Figure 6.9: (a – c) The illusory effect is diminished if the thickness of the white bars increases, cf. [SC05]. Note that the intensity of the illusory effect depends on the distance of the image to the eye. (d – f) The decrease of the smudges' intensities can also be observed in the reconstruction by (6.10). The precise quantities are depicted in the graph. There we see that the difference between the maximum gray value and the average gray level in the center decreases (brown line).

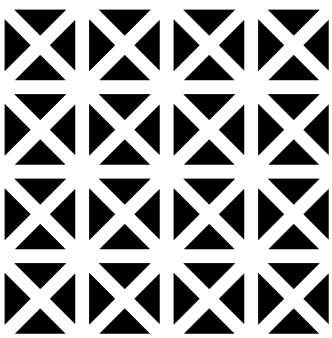

(a) Original.

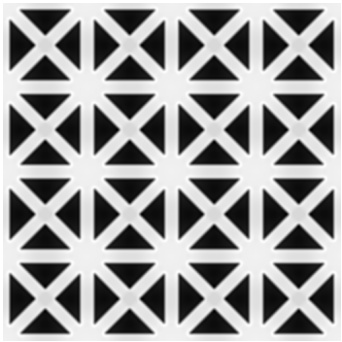

(b) Reconstruction by (6.10).

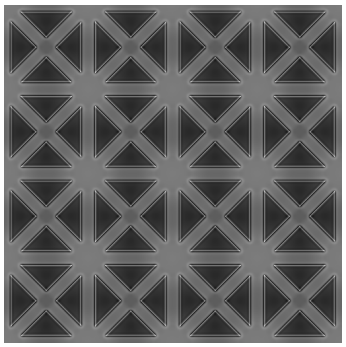

(c) Reconstruction error (gray values rescaled for better visibility, see profile plot (e) for the magnitudes).

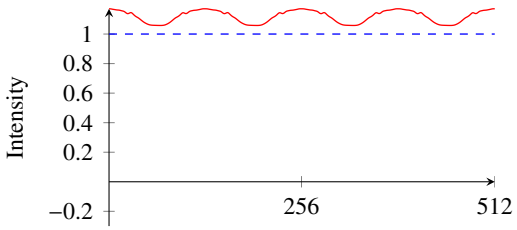

(d) Central horizontal profile of original (a) in blue and reconstruction (b) in red.

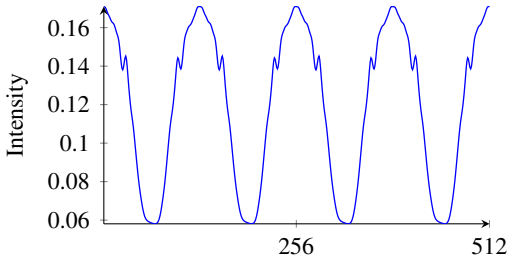

(e) Central profile of error (c).

Figure 6.10: The illusory effect of the Hermann grid is reduced significantly when diagonals are added, cf. [SC05]. Also in the reconstruction, the gray patches are only about half as intense as the patches in the original Hermann grid (Figure 6.7) and the variation is much smoother.

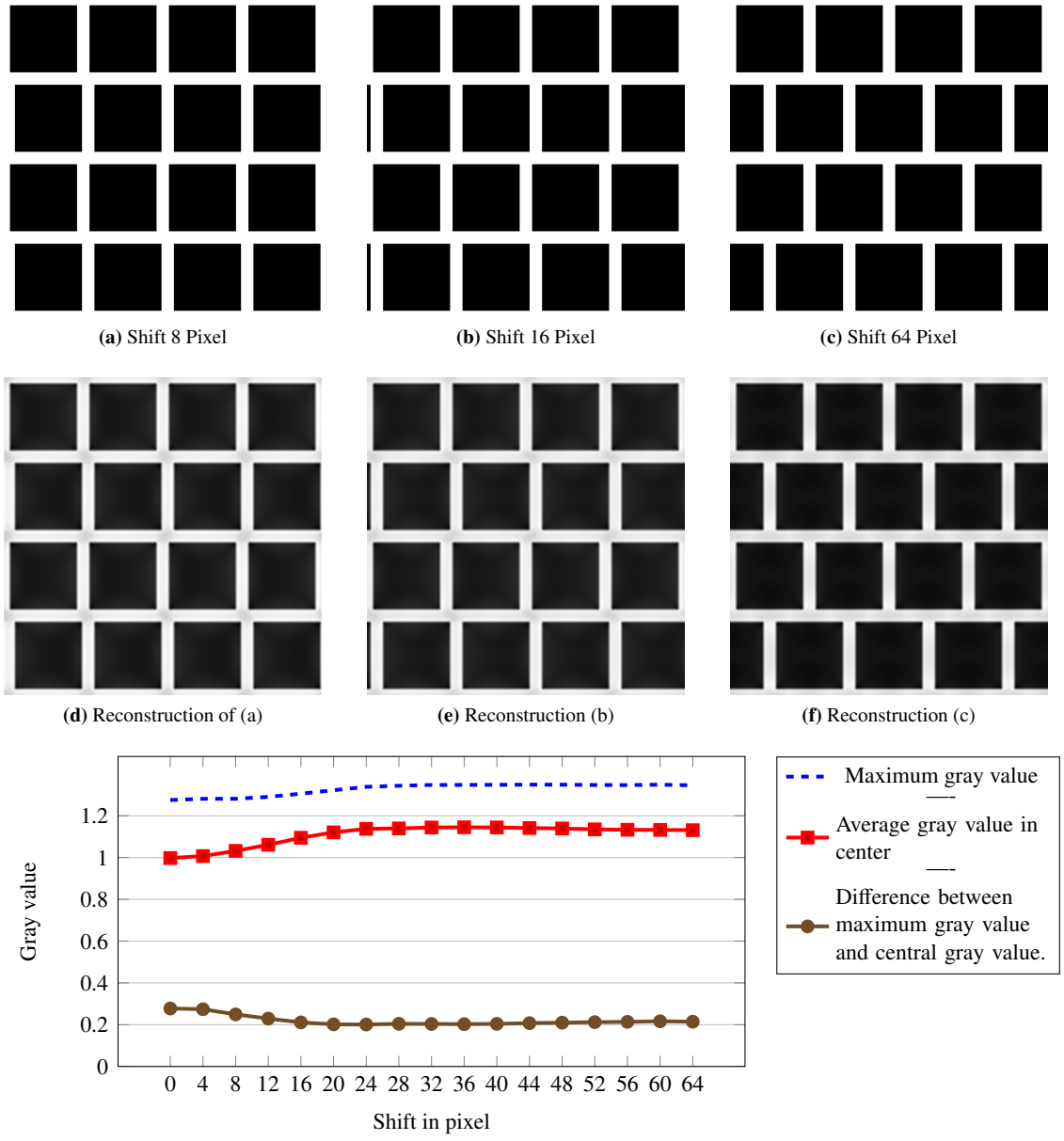

(a) Shift 8 Pixel **(b)** Shift 16 Pixel **(c)** Shift 64 Pixel

(d) Reconstruction of (a) **(e)** Reconstruction (b) **(f)** Reconstruction (c)

Figure 6.11: The illusory effect is diminished if the black squares are shifted [SC05] (a – c). This effect can be observed by the quantified reconstruction (d – f). The graph also shows that there is a saturation after a shift of about 20 to 24 pixels.

(a) Original.

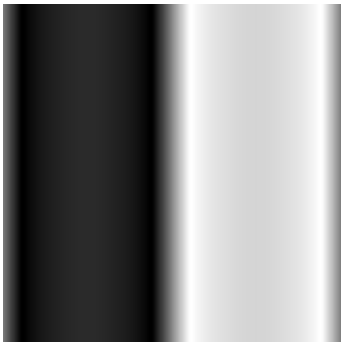

(b) Reconstruction by (6.10).

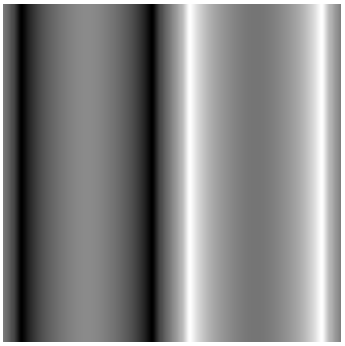

(c) Reconstruction error (gray values rescaled for better visibility, see profile plot (e) for the magnitudes).

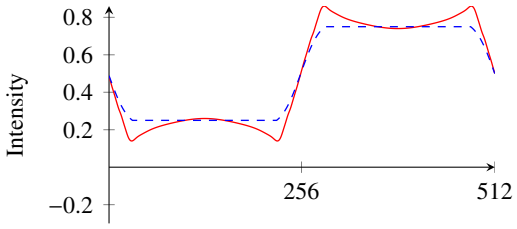

(d) Central horizontal profile of original (a) in blue and reconstruction (b) in red.

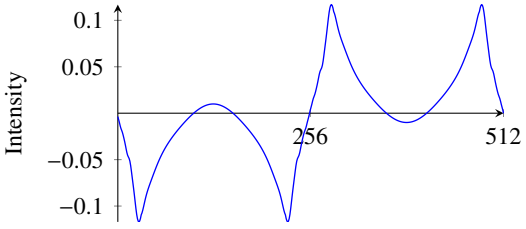

(e) Central profile of error (c).

Figure 6.12: (a) The observer recognizes two illusory thin strips at the sides of the central slope, so called Mach bands. (b – e) These illusory bands are nicely reproduced by the proposed simple cell model.

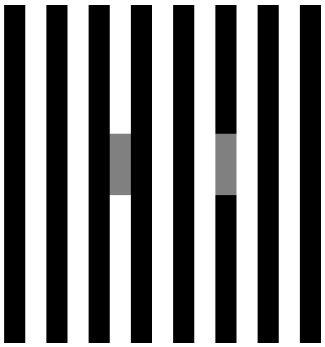

(a) Original.

(b) Reconstruction by (6.10).

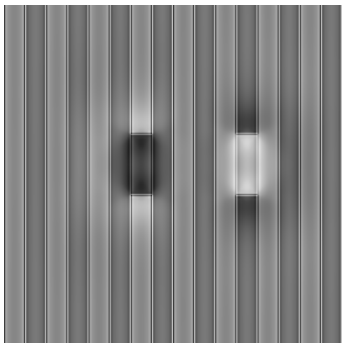

(c) Reconstruction error (gray values rescaled for better visibility, see profile plot (e) for the magnitudes).

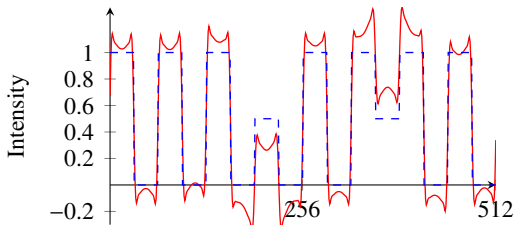

(d) Central horizontal profile of original (a) in blue and reconstruction (b) in red.

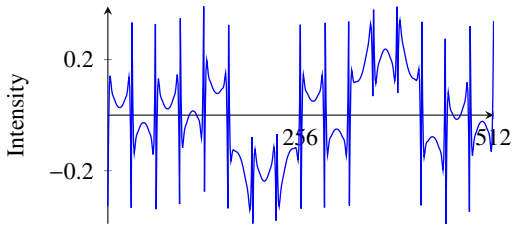

(e) Central profile of error (c).

Figure 6.13: The White illusion. The right gray patch appears to be brighter than the left one, although they have the same gray values. In the reconstruction, the right patch becomes indeed brighter than the left one, which can be best seen in the error image.

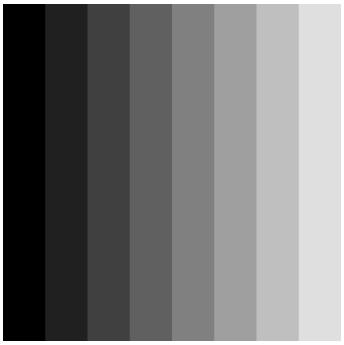

(a) Original.

(b) Reconstruction by (6.10).

(c) Reconstruction error (gray values rescaled for better visibility, see profile plot (e) for the magnitudes).

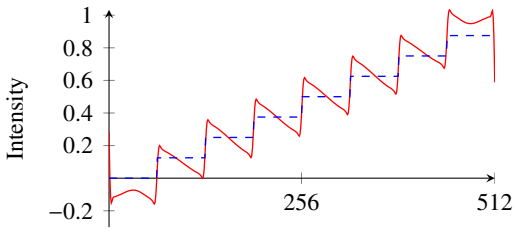

(d) Central horizontal profile of original (a) in blue and reconstruction (b) in red.

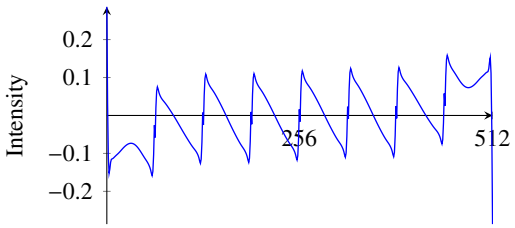

(e) Central profile of error (c).

Figure 6.14: The Chevreul illusion. Although the image (a) is piecewise constant it appears as if the stripes are brighter at their left hand side than at their right hand side. This illusory effect is simulated by the our quantization model.

Chapter 7

Conclusion and outlook

We have seen how reasonable wavelet amplitude and sign decompositions can be constructed and that such decompositions yield direct applications in signal and image analysis. It was investigated under which conditions combinations of quadrature operators and wavelet transforms are reasonable. Here, the Riesz and the partial Hilbert were in the focus, so the investigation of other quadrature operators is desirable.

We have used the connections between the coefficient's amplitudes to the wavefront set for setting up a computable edge model within a well developed theory. Here, a future direction of research will be the refinement of these models, for example by advancing from the classical wavefront set to the H^s-wavefront set.

We have further shown by the discrete signature that the wavelet signs can be applied to the analysis of signal and images. However, the theoretical foundations of wavelet signs in signal and image analysis are still poorly understood, so there is need for further research. First theoretical results in that direction could be obtained by the author in a joint work with L. Demaret and P. Massopust [DMS12].

At last, we proposed a model for the quantization of the wavelet coefficients' amplitudes within the visual system and gave computational evidence that this model reproduces the illusory effects of brightness illusions. For definite implications for the perception of brightness illusion, further physiological evidence is required.

A Appendix

A.1 The Fourier transform

We provide some basic facts about the Fourier transform, see e.g. [Bra00]. The Fourier transform for $f \in L^1(\mathbb{R}^n)$ is defined by

$$\widehat{f}(\xi) = \int_{\mathbb{R}} f(x) e^{-2\pi i\, x\cdot\xi}\, \mathrm{d}x.$$

For a distribution with compact support $f \in \mathcal{E}'(\mathbb{R}^n)$ the Fourier transform $\hat{f}$ is a function and we may write

$$\hat{f}(\xi) := \langle f, e_{-\xi}\rangle.$$

The Fourier transform for general tempered distributions $f \in \mathcal{S}'(\mathbb{R}^n)$ is defined by duality

$$\langle \hat{f}, \phi\rangle = \langle f, \hat{\phi}\rangle, \text{ for } \phi \in \mathcal{S}(\mathbb{R}^n).$$

If $A : \mathbb{R}^n \to \mathbb{R}^n$ is linear and invertible, then, by the change of variable,

$$\begin{aligned}\widehat{f\circ A}(\xi) &= \int_{\mathbb{R}^n} f(Ax) e^{-2\pi i x\cdot\xi}\, \mathrm{d}x = \frac{1}{|\det A|}\int_{\mathbb{R}^n} f(y) e^{-2\pi i A^{-1}y\cdot\xi}\, \mathrm{d}y \\ &= \frac{1}{|\det A|}\int_{\mathbb{R}^n} f(y) e^{-2\pi i y\cdot(A^{-1})^T\xi}\, \mathrm{d}y = \frac{1}{|\det A|}\widehat{f}((A^{-1})^T\xi). \end{aligned} \tag{A.1}$$

In particular, if A is orthogonal, then

$$\widehat{f\circ A}(\xi) = \widehat{f}(A\xi). \tag{A.2}$$

A table of frequently occurring Fourier transform is given in Table A.1.

A.2 The Meyer-type window functions

The radial Meyer-type window function W is defined by

$$W(\xi) = \begin{cases} \cos(\frac{\pi}{2} z(5-6\xi)), & \text{for } \frac{2}{3} \le \xi < \frac{5}{6}, \\ 1, & \text{for } \frac{5}{6} \le \xi < \frac{4}{3}, \\ \cos(\frac{\pi}{2} z(3\xi-4)), & \text{for } \frac{4}{3} \le \xi < \frac{5}{3}, \\ 0 & \text{else.} \end{cases} \tag{A.3}$$

$f(x)$	$\widehat{f}(\xi)$
Hermitian	real-valued
real-valued	Hermitian
$\mathbb{1}_{[-a,a]}$	$\frac{1}{\lvert a\rvert}\operatorname{sinc}\left(\frac{\xi}{a}\right)$
1	$\delta(\xi)$
$\operatorname{sgn}(x)$	$\frac{1}{i\pi\xi}$
$u(x) = \mathbb{1}_{[0,\infty)}$	$\frac{1}{2}\left(\frac{1}{i\pi\xi} + \delta(\xi)\right)$

Table A.1: Some important Fourier transforms.

and the angular Meyer-type window function V is given by

$$V(\xi) = \begin{cases} 1, & \text{for } |\xi| < \frac{1}{3}, \\ \cos(\frac{\pi}{2} z(3|\xi| - 4)), & \text{for } \frac{1}{3} \le |\xi| < \frac{2}{3}, \\ 0 & \text{else,} \end{cases} \tag{A.4}$$

see [Dau92, MP09]. Here z is a sufficiently smooth function satisfying

$$z(\xi) = \begin{cases} 0, & \text{for } \xi \le 0, \\ 1 & \text{for } \xi \ge 1, \end{cases} \qquad \text{and} \qquad z(\xi) + z(1-\xi) = 1, \quad \xi \in \mathbb{R}.$$

The following choices for z on the interval $(0, 1)$ yield C^0, C^1 and C^∞ regularity, respectively:

$$\begin{aligned} z_0(x) &= x, \\ z_1(x) &= 3x^2 - 2x^3, \\ z_\infty(x) &= \frac{s(x-1)}{s(x-1) + s(x)}, \end{aligned}$$

where

$$s(x) = \exp\left((1+x)^{-2} + (1-x)^{-2}\right).$$

Bibliography

[AGV09] P. Abry, P. Gonçalvès, and J.L. Véhel. *Scaling, Fractals and Wavelets*. ISTE, 2009.

[Bau60] G. Baumgartner. Indirekte Größenbestimmung der rezeptiven Felder der Retina beim Menschen mittels der Hermannschen Gittertäuschung. *Pflügers Archiv European Journal of Physiology*, 272(1):21–22, 1960.

[BCP07] M.F. Bear, B.W. Connors, and M.A. Paradiso. *Neuroscience: exploring the brain*. Philadelphia, PA:. Lippincott Williams & Wilkins, 2007.

[Bed62] E. Bedrosian. The analytic signal representation of modulated waveforms. *Proceedings of the IRE*, 50(10):2071–2076, 1962.

[BM99] B. Blakeslee and M.E. McCourt. A multiscale spatial filtering account of the White effect, simultaneous brightness contrast and grating induction. *Vision Research*, 39(26):4361–4377, 1999.

[Bra00] R.N. Bracewell. *The Fourier transform and its applications*. McGraw-Hill, 2000.

[BS01] T. Bülow and G. Sommer. Hypercomplex signals — a novel extension of the analytic signal to the multidimensional case. *IEEE Transactions on Signal Processing*, 49:2844–2852, 2001.

[Can86] J. Canny. A computational approach to edge detection. *IEEE Transactions on Pattern Analysis and Machine Intelligence*, PAMI-8(6):679 – 698, 1986.

[CD04] E. J. Candès and D. L. Donoho. New tight frames of curvelets and optimal representations of objects with piecewise C^2 singularities. *Communications on pure and applied mathematics*, 57(2):219–266, 2004.

[CD05a] E.J. Candes and D.L. Donoho. Continuous curvelet transform: I. Resolution of the wavefront set. *Applied and Computational Harmonic Analysis*, 19(2):162–197, 2005.

[CD05b] E.J. Candes and D.L. Donoho. Continuous curvelet transform: II. Discretization and frames. *Applied and Computational Harmonic Analysis*, 19(2):198–222, 2005.

[CHM97] M. Carandini, D. J. Heeger, and J. A. Movshon. Linearity and normalization in simple cells of the macaque primary visual cortex. *The Journal of Neuroscience*, 17(21):8621–8644, 1997.

[Chr03] O. Christensen. *An introduction to frames and Riesz bases*. Birkhäuser, 2003.

[CL07] D. Corney and R.B. Lotto. What are lightness illusions and why do we see them? *PLoS computational biology*, 3(9):e180, 2007.

[Dau85] J.G. Daugman. Uncertainty relation for resolution in space, spatial frequency, and orientation optimized by two-dimensional visual cortical filters. *Journal of the Optical Society of America A*, 2:1160–1169, 1985.

[Dau88] J.G. Daugman. Complete discrete 2-D gabor transforms by neural networks for image analysis and compression. *IEEE Transactions on Acoustics, Speech and Signal Processing*, 36(7):1169–1179, 1988.

[Dau92] I. Daubechies. *Ten lectures on wavelets*, volume 61. Society for Industrial Mathematics, 1992.

[DMS06] D. Donoho, A. Maleki, and M. Shahram. Wavelab 850. *Software toolkit for time-frequency analysis*, 2006.

[DMS12] L. Demaret, P. Massopust, and M. Storath. Signal analysis based on complex wavelet signs. *Submitted*, 2012. ArXiv preprint arXiv:1208.4578v1.

[Dui05] R. Duits. *Perceptual organization in image analysis*. PhD thesis, Technische Universiteit Eindhoven, 2005.

[DVAT82] R.L. De Valois, D.G. Albrecht, and L.G. Thorell. Spatial frequency selectivity of cells in macaque visual cortex. *Vision Research*, 22(5):545–559, 1982.

[ES97] I.U.V. Egorov and B.W. Schulze. *Pseudo-differential operators, singularities, applications*. Birkhäuser, 1997.

[FA91] W.T. Freeman and E.H. Adelson. The design and use of steerable filters. *IEEE Transactions on Pattern analysis and machine intelligence*, 13(9):891–906, 1991.

[Fis96] N.I. Fisher. *Statistical analysis of circular data*. Cambridge University Press, 1996.

[FJ98] F.G. Friedlander and M.S. Joshi. *Introduction to the Theory of Distributions*. Cambridge University Press, 1998.

[FJW91] M. Frazier, B. Jawerth, and G.L. Weiss. *Littlewood-Paley theory and the study of function spaces*. Number 79 in Regional conference series in mathematics. American Mathematical Society, 1991.

[FLE93] N.I. Fisher, T. Lewis, and B.J.J. Embleton. *Statistical analysis of spherical data*. Cambridge University Press, 1993.

[Fra08] E. Franken. *Enhancement of Crossing Elongated Structures in Images*. PhD thesis, Technische Universiteit Eindhoven, 2008.

[Fri12] J. Frikel. Sparse regularization in limited angle tomography. *Applied and Computational Harmonic Analysis*, 2012. to appear.

[FS00] M. Felsberg and G. Sommer. A new extension of linear signal processing for estimating local properties and detecting features. In *22. DAGM Symposium Mustererkennung*, 2000.

[FS01] M. Felsberg and G. Sommer. The monogenic signal. *IEEE Transactions on Signal Processing*, 49(12):3136–3144, 2001.

[FvdVB+04] B. Forster, D. van de Ville, J. Berent, D. Sage, and M. Unser. Complex wavelets for extended depth-of-field: A new method for the fusion of multichannel microscopy images. *Microscopy Research and Technique*, 65(1-2):33–42, 2004.

[Gab46] D. Gabor. Theory of communication. *Journal of the Institution of Electrical Engineers - Part III: Radio and Communication Engineering*, 93:429–457, 1946.

[GBHS08] J. Geier, L. Bernáth, M. Hudák, and L. Séra. Straightness as the main factor of the Hermann grid illusion. *Perception - London*, 37(5):651 —- 665, 2008.

[GL09] K. Guo and D. Labate. Characterization and analysis of edges using the continuous shearlet transform. *SIAM Journal on Imaging Sciences*, 2:959—-986, 2009.

[GM84] A. Grossmann and J. Morlet. Decomposition of hardy functions into square integrable wavelets of constant shape. *SIAM journal on mathematical analysis*, 15(4):723–736, 1984.

[GM91] J.E. Gilbert and M.A.M. Murray. *Clifford algebras and Dirac operators in harmonic analysis*, volume 26. Cambridge University Press, 1991.

[Gra04] L. Grafakos. *Classical and modern Fourier analysis*. Prentice Hall, 2004.

[GSS64] I.M. Gel´fand, G.E. Shilov, and E. Saletan. *Generalized functions*, volume 1. Academic press New York, 1964.

[Hah96] S.L. Hahn. *Hilbert transforms in signal processing*. Artech House on Demand, 1996.

[Hel10] S. Held. Personal communication. 2010.

[Hel12] S. Held. *Monogenic Wavelet Frames for Image Analysis*. PhD thesis, Technische Universität München, 2012. submitted.

[Her70] L. Hermann. Eine Erscheinung simultanen Contrastes. *Pflügers Archiv European Journal of Physiology*, 3(1):13–15, 1870. 10.1007/BF01855743.

[Hol95] M. Holschneider. *Wavelets. An analysis tool*. Oxford Mathematical Monographs, 1995.

[HSMF10] S. Held, M. Storath, P. Massopust, and B. Forster. Steerable wavelet frames based on the Riesz transform. *IEEE Transactions on Image Processing*, 19(3):653–667, March 2010.

[HW59] D.H. Hubel and T.N. Wiesel. Receptive fields of single neurones in the cat's striate cortex. *The Journal of Physiology*, 148(3):574–591, 1959.

[Hö85] L. Hörmander. *The analysis of linear partial differential operators*, volume III. Springer Verlag, 1985. Pseudodifferential operators.

[Hö03] L. Hörmander. *The analysis of linear partial differential operators*, volume I. Springer Verlag, Berlin, 2003. Distribution theory and Fourier analysis.

[Joy09] D. Joyce. On manifolds with corners. *Arxiv preprint arXiv:0910.3518*, 2009.

[Jä93] K. Jänich. *Vektoranalysis*. Springer, 1993.

[Kin99] N. Kingsbury. Image processing with complex wavelets. *Philosophical Transactions of the Royal Society of London. Series A: Mathematical, Physical and Engineering Sciences*, 357(1760):2543–2560, 1999.

[Kin01] N. Kingsbury. Complex wavelets for shift invariant analysis and filtering of signals. *Applied and Computational Harmonic Analysis*, 10(3):234–253, 2001.

[Kin08] F.W. King. Operator basis for analytic signal construction. *Multidimensional Systems and Signal Processing*, 19:131–137, 2008. 10.1007/s11045-007-0034-z.

[Kin09a] F.W. King. *Hilbert Transforms, Volume 1*. Cambridge University Press, 2009.

[Kin09b] F.W. King. *Hilbert Transforms, Volume 2*. Cambridge University Press, 2009.

[KL07] G. Kutyniok and D. Labate. Construction of regular and irregular shearlet frames. *Journal of Wavelet Theory and Applications*, 1(1):1–12, 2007.

[KL09] G. Kutyniok and D. Labate. Resolution of the wavefront set using continuous shearlets. *Transactions of the American Mathematical Society*, 361(5):2719–2754, 2009.

[KL12] G. Kutyniok and W-Q. Lim. Image separation using wavelets and shearlets. In J-D. Boissonnat, P. Chenin, A. Cohen, C. Gout, T. Lyche, M-L. Mazure, and L. Schumaker, editors, *Curves and Surfaces*, volume 6920 of *Lecture Notes in Computer Science*, pages 416–430. Springer, 2012.

[KMMG87] R. Kronland-Martinet, J. Morlet, and A. Grossmann. Analysis of sound patterns through wavelet transforms. *International Journal of Pattern Recognition and Artificial Intelligence*, 1(2):273–302, 1987.

[Kov99] P.D. Kovesi. Image features from phase congruency. *Videre: Journal of Computer Vision Research*, 1(3):1–26, 1999.

[Kov08] P.D. Kovesi. MATLAB and Octave functions for computer vision and image processing. *School of Computer Science & Software Engineering, The University of Western Australia*, 2008. `http://www.csse.uwa.edu.au/~pk/research/matlabfns/`, last checked on 2012/06/05.

[Kö04] K. Königsberger. *Analysis 2*. Springer, 2004.

[LBO01] K.G. Larkin, D.J. Bone, and M.A. Oldfield. Natural demodulation of two-dimensional fringe patterns. I. General background of the spiral phase quadrature transform. *Journal of the Optical Society of America A*, 18(8):1862–1870, 2001.

[Lee96] T.S. Lee. Image representation using 2D Gabor wavelets. *IEEE Transactions on Pattern Analysis and Machine Intelligence*, 18(10):959–971, 1996.

[Lee03] J.M. Lee. *Introduction to smooth manifolds*. Springer Verlag, 2003.

[LJ77] B.F. Logan Jr. Information in the zero crossings of bandpass signals. *Bell System Technical Journal*, 56:487–510, 1977.

[LLKW05] D. Labate, W.Q. Lim, G. Kutyniok, and G. Weiss. Sparse multidimensional representation using shearlets. In *Society of Photo-Optical Instrumentation Engineers (SPIE) Conference Series*, volume 5914, pages 254–262, 2005.

[Mal09] S. Mallat. *A Wavelet Tour of Signal Processing - The Sparse Way*. Academic Press, 2009.

[MM99] J.A. McArthur and B. Moulden. A two-dimensional model of brightness perception based on spatial filtering consistent with retinal processing. *Vision Research*, 39(6):1199–1219, 1999.

[MO87] M.C. Morrone and R.A. Owens. Feature detection from local energy. *Pattern Recognition Letters*, 6(5):303–313, 1987.

[MP09] J. Ma and G. Plonka. A review of curvelets and recent applications. *IEEE Signal Processing Magazine*, 2009.

[MS89] D. Mumford and J. Shah. Optimal approximations by piecewise smooth functions and associated variational problems. *Communications on Pure and Applied Mathematics*, 42(5):577–685, 1989.

[OL81] A.V. Oppenheim and J.S. Lim. The importance of phase in signals. *Proceedings of the IEEE*, 69(5):529–541, 1981.

[OM09] S. C. Olhede and G. Metikas. The monogenic wavelet transform. *IEEE Transactions on Signal Processing*, 57(9):3426–3441, 2009.

[OVAP08] X. Otazu, M. Vanrell, and C. Alejandro Párraga. Multiresolution wavelet framework models brightness induction effects. *Vision research*, 48(5):733–751, 2008.

[Pal99] S.E. Palmer. *Vision science: Photons to phenomenology*. MIT Press, 1999.

[Pet83] B.E. Petersen. *Introduction to the Fourier transform & pseudodifferential operators*, volume 19 of *Monographs and Studies in Mathematics*. Pitman (Advanced Publishing Program), Boston, 1983.

[Qui93] E.T. Quinto. Singularities of the x-ray transform and limited data tomography in $\mathbb{R}^2$ and $\mathbb{R}^3$. *SIAM Journal on Mathematical Analysis*, 24(5):1215–1225, 1993.

[Rad12] Radiopedia, 2012. Radiopedia.org, Last checked on 2012/06/05.

[SBK05] I.W. Selesnick, R.G. Baraniuk, and N.C. Kingsbury. The dual-tree complex wavelet transform. *IEEE Signal Processing Magazine*, 22(6):123–151, 2005.

[SBS+87] B. C. Skottun, A. Bradley, G. Sclar, I. Ohzawa, and R. D. Freeman. The effects of contrast on visual orientation and spatial frequency discrimination: a comparison of single cells and behavior. *Journal of Neurophysiology*, 57(3):773–786, 1987.

[SC05] P.H. Schiller and C.E. Carvey. The Hermann grid illusion revisited. *Perception - London*, 34(11):1375–1397, 2005.

[SFV76] P.H. Schiller, B.L. Finlay, and S.F. Volman. Quantitative studies of Single-Cell properties in monkey striate cortex. I. spatiotemporal organization of receptive fields. *Journal of Neurophysiology*, 39(6):1288–1319, 1976.

[Sog93] C.D. Sogge. *Fourier integrals in classical analysis*. Cambridge University Press, 1993.

[SSM05] W.A. Simpson, U. Shahani, and V. Manahilov. Illusory percepts of moving patterns due to discrete temporal sampling. *Neuroscience Letters*, 375(1):23–27, 2005.

[Ste70] E. M. Stein. *Singular Integrals and Differentiability Properties of Functions*. Princeton University Press, 1970.

[Sto08] M. Storath. Wavelets und das monogene Signal. Diploma thesis, Technische Universität München, 2008.

[Sto10] M. Storath. The monogenic curvelet transform. In *Proceedings of the IEEE International Conference on Image Processing (ICIP), Hong Kong*, pages 353–356, 2010.

[Sto11a] M. Storath. Directional multiscale amplitude and phase decomposition by the monogenic curvelet transform. *SIAM Journal on Imaging Sciences*, 4:57–78, 2011.

[Sto11b] M. Storath. Separation of edges in x-ray images by microlocal analysis. *Proceedings in Applied Mathematics and Mechanics (PAMM)*, 11(1):867–868, 2011.

[THH05] C.L. Tu, W.L. Hwang, and J. Ho. Analysis of singularities from modulus maxima of complex wavelets. *IEEE Transactions on Information Theory*, 51(3):1049–1062, 2005.

[Tit48] E.C. Titchmarsh. *Introduction to the theory of Fourier integrals*, volume 337. Clarendon Press Oxford, 1948.

[USvdV09] M. Unser, D. Sage, and D. van de Ville. Multiresolution monogenic signal analysis using the Riesz-Laplace wavelet transform. *IEEE Transactions on Image Processing*, 18(11):2402–2418, 2009.

[UvdV09] M. Unser and D. van de Ville. Higher-order Riesz transforms and steerable wavelet frames. In *Proceedings of the IEEE International Conference on Image Processing*, pages 3801–3804, Cairo, 2009.

[YLEK09] S. Yi, D. Labate, G.R. Easley, and H. Krim. A shearlet approach to edge analysis and detection. *IEEE Transactions on Image Processing*, 18(5):929–941, 2009.